All-Optical Characterization of the Mechanical Properties of 2D Materials

MSE53035: MSE Master Thesis

Lukas Pott

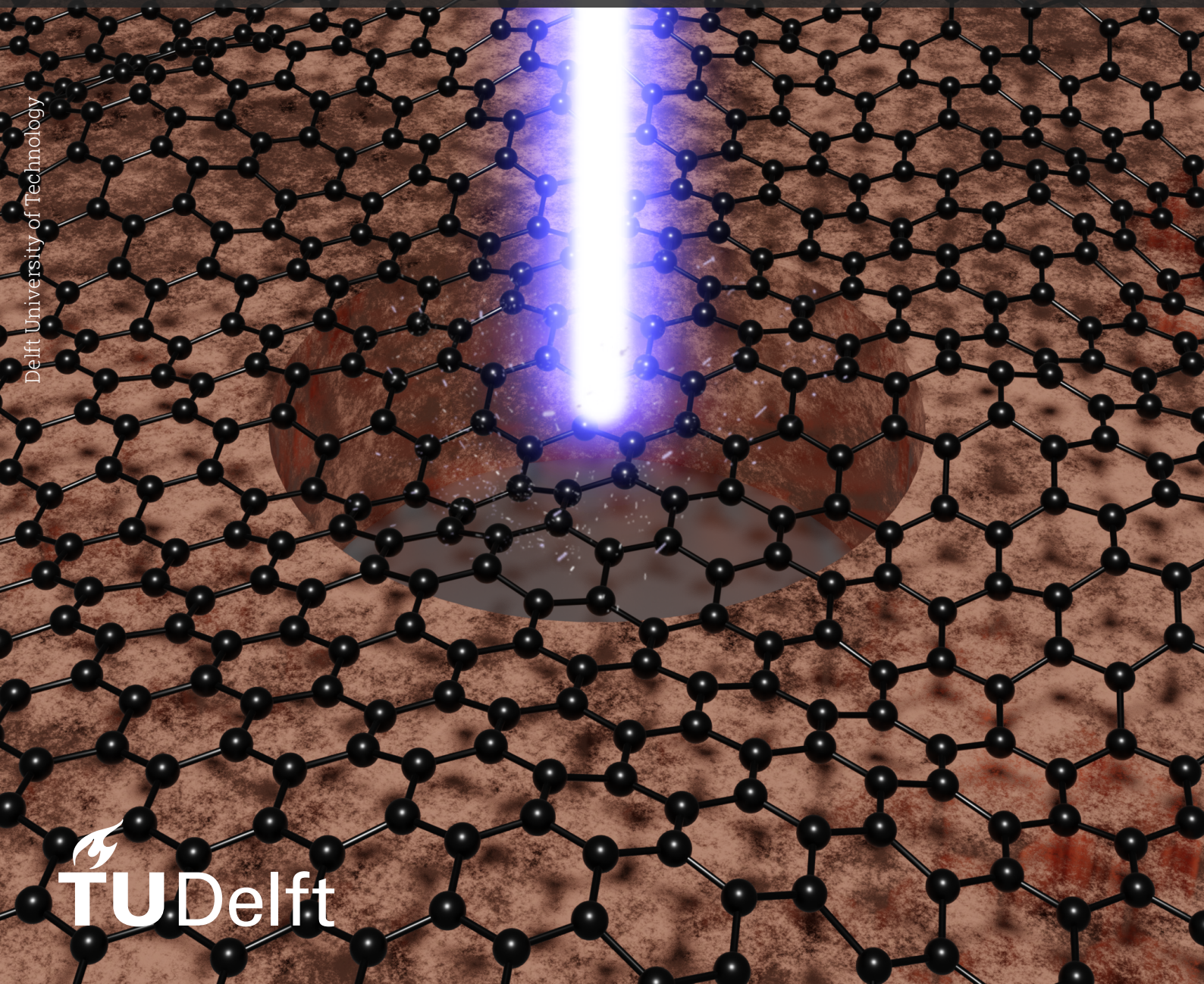

Delft University of Technology

TU Delft

All-Optical Characterization of the Mechanical Properties of 2D Materials

by

Lukas Pott

Dissertation

to obtain the degree of Master of Science
at Delft University of Technology.
To be defended publicly on
Monday, February 10, 2025, at 13:00

Committee: Prof. Dr. Peter Steeneken
Prof. Dr. Sid Kumar
Prof. Dr. Herre van der Zant
M.Sc. Álvaro Bermejillo Seco

Cover: Graphical Representation of the Actuation of a Graphene Monolayer Suspended Over a Circular Cavity by Optothermal Actuation With a Blue Laser

Style: TU Delft Report Style, with modifications by Daan Zwaneveld and Lukas Pott

TU Delft

Summary

Two-dimensional materials have attracted scientific interest due to their exceptional chemical, optical, electronic, and mechanical properties. In particular, their Young's modulus plays a crucial role in applications such as sensors, flexible electronics, and composite reinforcement. However, material defects, which are inevitable during fabrication and device operation, can significantly impact mechanical properties. The influence of defects on the Young's modulus remains a topic of debate, with contradictory experimental and theoretical findings presented in literature.

The most widely used method for measuring Young's modulus is atomic force microscopy (AFM) nanoindentation. However, it suffers from tip-sample interactions, high stress concentrations, and significant variability in reported values. To address these limitations, this thesis presents a novel, all-optical method for measuring the Young's modulus of monolayer membranes, eliminating physical contact with the sample and requiring no preliminary material assumptions.

The proposed method provides Young's modulus values by measuring nonlinear membrane dynamics together with higher harmonics and Brownian motion. Although the results exceed values reported in literature, it is noteworthy that this method yielded results for the modulus, despite inherent challenges associated with the measurement of 2D material monolayers. Various potential error sources have been identified and discussed, including measurement sensitivity, mode shape variations, and contamination effects. Recommendations for future research are provided to refine the approach and improve accuracy.

With the right experimental advancements, this contactless optical technique could serve as a viable alternative to AFM nanoindentation, offering a non-invasive way to study the mechanical properties of 2D materials with greater precision and reproducibility.

Contents

Nomenclature

Symbol	Definition	Unit
α	Transduction factor	[V^2/m^2]
β	Mass-normalized duffing coefficient	[$N/(m^3 \cdot kg)$]
b	Damping coefficient	[N·s/m]
δ	Vibration amplitude	[m]
E	Young's modulus	[Pa]
F	Force	[N]
f_0	Resonance frequency	[Hz]
f_{max}	Resonance frequency at maximum amplitude	[Hz]
g	Average membrane position	[m]
h	Thickness	[m]
$I_{n\omega}$	Intensity of the n-th harmonic	[V]
k_1	Linear spring constant	[N/m]
k_3	Nonlinear spring constant (Duffing coefficient)	[N/m^3]
k_B	Boltzmann constant	[J/K]
k_{eff}	Effective spring constant	[N/m]
λ	Wavelength	[m]
m	Mass of the resonator	[kg]
m_{eff}	Effective mass of the resonator	[kg]
ν	Poisson ratio	
Q	Quality factor	
R	Radius	[m]
S_{21}	Forward transmission coefficient	
S_{zz}	Power spectral density	[V^2/Hz]
σ	Stress	[Pa]
T	Temperature	[K]
V_{RMS}	Root Mean Square Voltage	[V]
ω	Angular frequency	[rad/s]
ω_0	Natural angular frequency	[rad/s]
x	Displacement	[m]
$\bar{X}$	Amplitude of steady-state oscillation	[m]
$\bar{X}_c$	Critical amplitude for nonlinearity	[m]
$\bar{X}_{\text{max}}$	Maximum amplitude of steady-state oscillation	[m]
ϕ	Phase difference	[rad]
ϵ	Strain	

1 Introduction

1.1. Two-Dimensional Materials

With the scientific study and fabrication of two-dimensional (2D) materials, researchers address current challenges in areas such as the semiconductor and medical industries, as well as sensor technology and the renewable energy sector [1–4]. The study of materials that extend only in two dimensions while retaining atomic thickness is crucial, as it allows for significant improvements in chemical, optical, electronic, and mechanical properties. In comparison to their bulk counterparts that are held together by van der Waals bonds, atomically thin monolayers from the same element or compound exhibit tremendously enhanced properties. For example, 2D materials offer improved carrier mobility and thermal conductivity, as well as a tunable band gap and the possibility for chemical functionalization [3, 5].

Concretely, the superior mechanical properties of some 2D materials have aroused great interest, and makes them suitable for applications ranging from sensors to flexible and wearable electronics, nanoelectromechanical systems (NEMS) and reinforcement agents in composites [3, 6–8]. Due to their atomic thickness and high aspect ratio, monolayers of van der Waals materials typically show very low bending stiffness while maintaining extremely high in-plane strength and stiffness, which is defined by the Young's modulus [9]. Within the more than a thousand known and predicted 2D materials, typical materials with promising mechanical properties include hexagonal boron nitride (hBN), Xenes, molybdenum disulfide (MoS_2) and graphene [8, 10–13]. Among these materials, graphene, and MoS_2 have attracted particular interest due to their outstanding mechanical properties resulting from a planar honeycomb-like atomic structure.

The outstanding material properties are not only intrinsically present, but can be tailored specifically to a desired application. The modification of the properties can occur via strain, functionalization, or the inclusion of lattice defects, with the latter being known as the field of defect engineering [7, 14–16]. Besides the relevance of lattice defects for the tunability of mechanical properties of monolayers, defects play a crucial role for applications of 2D materials in photovoltaics, integrated circuits, mechanical and chemical sensors as well as in composite reinforcement [17, 18]. Defects are not only introduced into a material to improve its properties, but arise during production and the exposure to ambient conditions and elevated temperatures during the device lifetime. This can have tremendous impact on the device performance, which further demonstrates the need to thoroughly understand the interdependence between mechanical properties and defect kind and concentration.

1.2. State of the Art

To use 2D materials as reinforcement agents in composites, the Young's modulus (E) is an important parameter, since materials with a high modulus allow significant reinforcement. The Young's modulus is an intrinsic material property that describes the stress-strain behavior of the material in the linear elastic regime under a uniaxially applied force. It can be regarded as a proportionality factor between

the stress σ and the resulting strain ϵ as:

$$\sigma = E\epsilon. \tag{1.1}$$

This definition is only valid for isotropic material properties along all directions. To describe the stress-strain relationship of anisotropic materials, a full stiffness tensor is required. For two-dimensional materials, it is possible to define an in-plane and out-of-plane Young's modulus, depending on the direction of the applied force. The in-plane modulus is a measure of the stiffness of the material for an applied force that acts within the plane. Thus, it is determined by the strength of the interatomic covalent bonds. For a 2D material of multiple layers, the out-of-plane modulus is defined for a force acting perpendicular to the plane of the material, and is thus governed by the van der Waals forces between the individual layers. Additionally, the Poisson ratio (ν) is an important material parameter, which describes the deformation of a material in the direction perpendicular to a uniaxially applied force. The Young's modulus and Poisson ratio will be of importance for the calculation of the material properties later in this thesis.

The measurement of Young's modulus in 2D materials is inherently challenging, leading to a wide spread of reported values in the literature. Furthermore, while the influence of defects is highly relevant, no scientific consensus has been reached. Contradictory results have been reported in both experimental and theoretical studies, as highlighted in Figure 1.1. The figure shows the influence of single vacancies on the in-plane Young's modulus of graphene as at increasing defect concentration. While the majority of the studies show a continuous decrease of the modulus with increasing defect concentration, few studies show a significant modulus increase at low defect concentration, followed by a continuous decrease. The number of experimental studies examining the influence of defects on the modulus is limited, with only one experimental study showing an increase of the modulus at low defect concentrations [19].

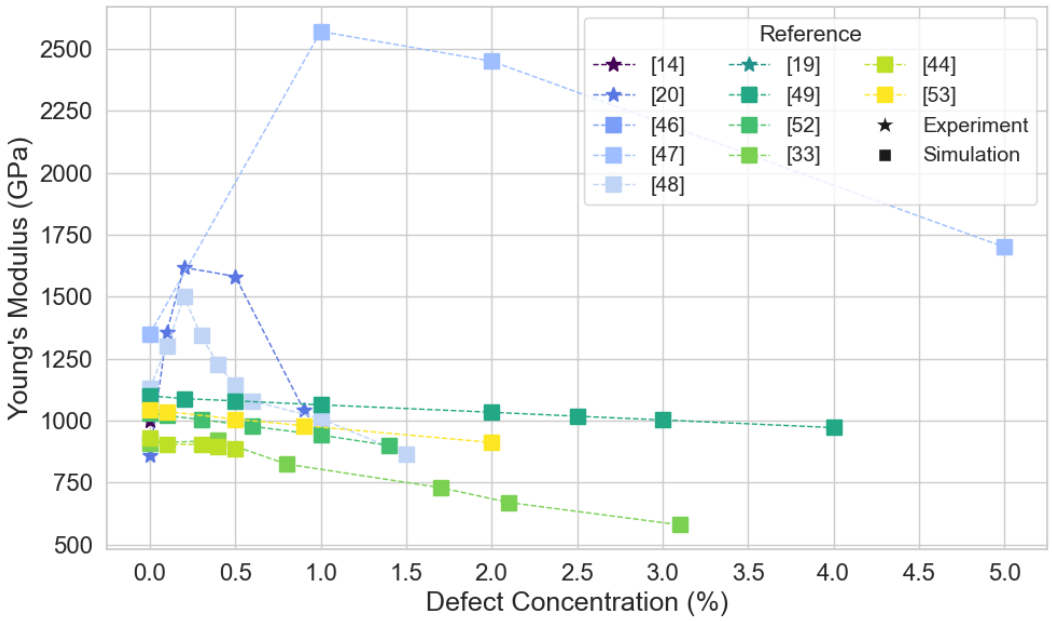

Figure 1.1: Influence of single vacancies on the Young's modulus of graphene monolayers, as presented in various references from the Literature Review of this thesis. References indicating an increase in the Young's modulus are represented by blue shades. For a more in-depth explanation of the types of defects and their influence on the mechanical properties of graphene and MoS_2, the reader is referred to the Literature Review in Appendix C.

In 2014, López-Polín and co-workers reported a method to drastically increase the in-plane Young's modulus of suspended graphene monolayers via the inclusion of lattice point defects [19]. The remarkable modulus increase was achieved by introducing low densities of single and di-vacancies of carbon

atoms into the material by irradiation with helium ions. At a defect concentration of $\sim$ 0.2 %, the greatest increase in modulus by almost a factor of two from 859 to 1618 GPa was found. The principle of the modulus increase was related to the suppression of thermal out-of-plane membrane fluctuations, which typically occur at room temperature. The suppression of these extended fluctuations is hypothesized to keep the membrane predominantly in the 2D plane, thus increasing the stiffness of suspended graphene monolayers.

To measure the modulus of the defective, freestanding monolayers, the authors applied Atomic Force Microscopy (AFM) Nanoindentation. In AFM Nanoindentation, an AFM tip is indented onto the monolayer membrane with increasing force, while the resulting force-displacement response is measured. From the force-displacement response, it is possible to extract the Young's modulus of the material. Despite being widely applied, this technique has several drawbacks and can lead to erroneous results when performed on freestanding monolayer membranes. The AFM tip can lead to high stress concentration, which drastically increases the risk of tip penetration and membrane damage, potentially hindering reproducible results [20, 21]. Furthermore, variations in the tip morphology through wear or contamination can contribute to the formation of artifacts and result in inaccurate measurements [20]. Due to the low bending stiffness of monolayer membranes, tip-sample interactions caused by adhesion forces from condensed liquid on the membrane can further alter the force-displacement relation [21]. AFM nanoindentation is a static technique, where indentation of the tip proceeds slowly, allowing viscoelastic and thermomechanical effects to influence the measurement [21]. Processes such as membrane slippage or delamination of the 2D material can further modify the results of a static deflection method. In addition to the experimental challenges associated with AFM Nanoindentation, large variations in the Young's moduli of 2D materials are reported in literature [22]. This emphasizes the experimental challenges associated with the measurement of the mechanical properties of 2D materials.

1.3. Nanomechanical Resonators and Nonlinear Dynamic Characterization

These difficulties with nanoindentation measurements have sparked research on alternative, non-contact methods to characterize the mechanical properties of freestanding 2D membranes. A method developed by Davidovikj *et al.* allows the dynamic characterization of the mechanical properties of freestanding membranes by analyzing the nonlinear mechanics of nanomechanical membrane resonators under forced oscillations in the MHz regime [22]. By applying this method, the nonlinear cubic spring constant of a membrane resonator, which becomes relevant at high vibrational amplitudes, can be related to its Young's modulus and pre-tension. 2D material membrane resonators consist of a circular cavity, which is covered by a suspended flake of 2D material forming the resonating membrane. The thickness of the suspended membrane can vary from a monolayer to several 10s of layers. Compared to AFM Nanoindentation, this nonlinear dynamic characterization technique that operates at frequencies in the MHz regime, thus providing values averaged over millions of vibration cycles. Furthermore, slippage, delamination, as well as viscoelastic and thermomechanical effects are drastically reduced, enhancing the accuracy of the method [22].

Membrane resonators formed by a 2D material are particularly suited for nonlinear dynamic characterization because nonlinear effects become relevant at very low actuation forces in the range of picoNewtons [22]. By combining membrane actuation with interferometric readout, very precise determination of the resonator's amplitude and cubic spring constant is possible. Davidovikj *et al.* obtained the Young's modulus of 5 nm thick graphene and MoS_2 nanomechanical resonators by fitting only the cubic spring constant to an experimentally determined amplitude response. The results obtained with this method were in close agreement with literature values. However, the method required estimation of the mass of the suspended membrane and was calculated with the density of the studied materials. In contrast to multilayer membranes as those studied by Davidovikj *et al.*, small contaminations, impurities, and defects from the production and transfer processes have a significantly pronounced effect on the mass of a monolayer membrane. Masses of monolayer membranes were shown to deviate by 600 %, which could lead to inaccurate results for the Young's modulus if monolayer masses are estimated [23].

1.4. Scope of This Thesis

To investigate the relationship between defects and the Young's modulus of monolayer 2D materials, this thesis proposes a novel experimental technique that enables the extraction of the modulus without requiring any material-specific assumptions. The presented work builds upon the approach developed by Davidovikj *et al.*, and extends it with an optical amplitude calibration from Dolleman *et al.* and a mass determination technique [22, 24]. As a result, the proposed method is entirely optical, eliminating the need for prior knowledge of the resonator's mass, pre-tension, or applied force. It serves as a non-contact alternative to AFM Nanoindentation, reducing viscoelastic and thermomechanical effects by operating in the dynamic regime and avoiding tip-sample interactions.

The goal of this thesis is the development of a reliable method to study the Young's modulus of 2D material monolayers. It should serve as a fundament to facilitate experimental work on the influence of defects on the Young's modulus of monolayer membranes of 2D materials like graphene and MoS_2 without requiring AFM Nanoindentation or preliminary assumptions about the material.

Throughout this thesis, the necessary theoretical fundament of nanomechanical resonators and their nonlinear dynamics is presented, followed by a detailed explanation of the experimental methodology and physical principles governing the method. The analytical procedure is then introduced and applied to four MoS_2 monolayer resonators. Finally, the results are discussed alongside potential error contributions, concluding with an outlook on future experiments to explore the effects of defects in monolayer 2D materials.

2

Theory

2.1. Membrane Resonators in the Linear Regime

The resonators studied in this thesis are circular membranes made of a single layer of 2D materials. Such membranes are extremely thin and have negligible bending stiffness κ in comparison to their bulk counterparts [25]. As a result, the overall in-plane mechanical stiffness of these membranes is governed by their in-plane tensile stress n_0, also referred to as pre-stress [26]. This allows the treatment of the presented resonators as structures in the membrane limit, in contrast to the theory of plate resonators whose mechanics are dominated by their bending stiffness [27].
To derive mathematical expressions, the focus lies on one-dimensional linear and nonlinear membrane resonators with only one degree of freedom. For a membrane resonator, this degree of freedom corresponds to the displacement of the membrane in the direction orthogonal to the plane of the non-suspended membrane.

2.1.1. Linear Equations of Motion

In the linear regime, the previously described resonators can be approximated as classical linear harmonic oscillators (LHOs), where the system dynamics are dominated by a restoring force. This restoring force F acts on the oscillator when it is displaced from its equilibrium position and is directly proportional to the displacement x, following Hooke's law:

$$F = -k_1 x. \tag{2.1}$$

The restoring force acts in the opposite direction of the displacement and is directly proportional, with a proportionality factor k_1 called the linear spring constant. The force that is acting on the mass can drive the motion of an oscillator periodically with an angular frequency ω, and is then described via:

$$F_{periodic} = F cos(\omega t). \tag{2.2}$$

To characterize and model a LHO with a single degree of freedom, one can use an equation of motion (EOM) that describes the force acting on the oscillator. In addition to the restoring force, a force of inertia produced by the oscillator mass m ($F = m\ddot{x}$) acts on the vibrating system. In total, the EOM of a LHO with a periodic force can be formulated as [28]:

$$m\ddot{x} + k_1 x = F cos(\omega t). \tag{2.3}$$

This equation holds for ideal systems where no damping occurs. In real physical systems, parts of the oscillation energy are dissipated through damping mechanisms, which are captured by adding a term $b\dot{x}$ to the EOM. Thus, the motion of a damped linear oscillator follows the relation [28]:

$$m\ddot{x} + b\dot{x} + k_1 x = F cos(\omega t). \tag{2.4}$$

The damping force is proportional to the damping coefficient b, which is defined via the quality factor Q as $b = \frac{\omega_0 m}{Q}$. The quality factor gives information about the energy dissipation during one oscillation period and can be understood as the ratio of stored versus lost energy during this period.

With the damping factor and the natural frequency ω_0:

$$\omega_0 = \sqrt{\frac{k_1}{m}}, \tag{2.5}$$

Equation 2.4 can be reformulated to:

$$m\ddot{x} + \frac{\omega_0 m}{Q}\dot{x} + \omega_0^2 m x = F cos(\omega t). \tag{2.6}$$

To facilitate comparability across multiple resonating systems, it is common practice to write Equation 2.6 in the mass-normalized form:

$$\ddot{x} + \frac{\omega_0}{Q}\dot{x} + \omega_0^2 x = \frac{F}{m}\cos(\omega t). \tag{2.7}$$

2.1.2. Steady-State Amplitude of a Linear Harmonic Membrane Resonator

The steady-state amplitude response is important and can be used to determine the oscillation magnitude $\bar{X}$ of a resonator in equilibrium with the driving force as a function of the driving frequency. Starting with Equation 2.7, one can derive an expression for $\bar{X}$ by assuming a sinusoidal displacement $x(t)$, which follows the driving force at the same frequency but with a phase difference ϕ:

$$x(t) = \bar{X}\cos(\omega t - \phi). \tag{2.8}$$

By inserting the derivatives of this function into the mass-normalized EOM, one obtains the amplitude response after mathematical simplification as [26]:

$$\bar{X} = \frac{\frac{F}{m}}{\sqrt{\left(\omega_0^2 - \omega^2\right)^2 + \left(\frac{\omega\omega_0}{Q}\right)^2}}. \tag{2.9}$$

The corresponding phase is described by:

$$\phi = -\arctan(\frac{\omega_0\omega}{Q(\omega_0^2 - \omega^2)}). \tag{2.10}$$

Equation 2.9 will be of importance in section 3.5, where it is used to obtain a value for F/m to plot the full amplitude response of a nonlinear membrane resonator and extract the applied driving force.
At resonance, where $\omega = \omega_0$, the equations for amplitude and phase simplify to:

$$\bar{X}(\omega = \omega_0) = \frac{FQ}{\omega_0^2 m}, \tag{2.11}$$

$$\phi(\omega = \omega_0) = -\frac{\pi}{2}. \tag{2.12}$$

2.2. Nonlinear Dynamics and the Duffing Equation

2.2.1. Nonlinear Equation of Motion

A membrane resonator subject to a harmonic driving force is linear until a certain critical amplitude X_c. At higher driving forces, the amplitude increases above this critical level and the resonator transitions to the nonlinear regime. In this regime, the restoring force is not directly proportional to the resonator

displacement, but shows a higher-order dependence on the displacement from the equilibrium position. Such behavior can be intuitively understood by a phenomenon called geometric nonlinearity. If a membrane is clamped along its full circumference, large vertical displacement of the membrane can only be achieved by stretching the interatomic bonds. This bond stretching leads to a stiffening of the material, which in turn leads to a change in resonance frequency and deviation from the linear dynamic behavior.

Assuming symmetry of the restoring force in both positive and negative displacement directions ($F(x) = -F(-x)$), Hooke's law ($F = -k_1 x$) can be expanded to produce [22]:

$$F(x) = -k_1 x - k_3 x^3 + ..., \tag{2.13}$$

where higher order terms are neglected for the scope of this thesis. In this equation, k_3 is called the nonlinear spring constant, cubic spring constant or Duffing coefficient. It gives rise to the Duffing equation, which is presented below and will be of great importance for this thesis and the estimation of the Young's modulus of membrane resonators. This additional component of the restoring force has significant consequences for the total equation of motion. By adding the cubic part of the restoring force to Equation 2.7, one arrives at the Duffing equation [26]:

$$m\ddot{x} + \frac{\omega_0 m}{Q}\dot{x} + \omega_0^2 m x + k_3 x^3 = F cos(\omega t). \tag{2.14}$$

Performing mass-normalization, the following form of the Duffing equation is obtained [26]:

$$\ddot{x} + \frac{\omega_0}{Q}\dot{x} + \omega_0^2 x + \beta x^3 = \frac{F}{m}\cos(\omega t), \tag{2.15}$$

with the mass-normalized Duffing coefficient β:

$$\beta = \frac{k_3}{m}. \tag{2.16}$$

At this point, it is important to introduce the concept of an effective mass m_{eff}, which will become relevant for the extraction of the real physical parameters (section 3.5) of the membrane resonators treated in this thesis. The effective mass of a membrane is a mode-dependent mass, which takes the vibrational shape of a specific mode into account. In a given vibrational mode, different regions of the membrane vibrate with varying amplitudes, resulting in an effective mass that is lower than the total physical mass. Throughout this thesis, only the fundamental mode of the presented circular membrane resonators is studied, which can be calculated from the total resonator mass m as [29]:

$$m_{eff} = 0.2695m. \tag{2.17}$$

As a result, all equations that are applied to the fundamental mode of the resonators in this thesis require the use of the effective mass instead of the total drum mass.

2.2.2. Steady-State Amplitude of a Nonlinear Membrane Resonator

The steady-state equation for the amplitude of a membrane resonator oscillating in the nonlinear regime can be derived by assuming the resonator's motion as a single harmonic. The mathematical process for the derivation of the steady state solution is explained in [30] and results in the following equation for the amplitude response when nonlinear damping is neglected:

$$\bar{X}^6\left(\frac{9\beta^2}{16}\right) + \bar{X}^4\left(\frac{3\beta(\omega_0^2 - \omega^2)}{2}\right) + \bar{X}^2\left(\left(\frac{\omega_0\omega}{Q}\right)^2 + (\omega_0^2 - \omega^2)^2\right) = \left(\frac{F_\omega}{m}\right)^2. \tag{2.18}$$

Here, $\bar{X}$ is the steady-state amplitude.

2.2.3. Resonator Behavior in the Nonlinear Regime

To qualitatively understand the behavior of a system which is described by Equation 2.14, it is helpful to write the total restoring force from Equation 2.13 as [31]:

$$F(x) = -(k_1 + k_3 x^2)x. \tag{2.19}$$

From here, one can define the effective spring constant k_{eff} [31]:

$$k_{eff} = k_1 + k_3 x^2. \tag{2.20}$$

Thus, it becomes clear that the stiffness of the resonator becomes dependent on the amplitude, which is represented by the term $k_3 x^2$. Further, it follows that the total stiffness of a resonating membrane is dictated by the sign of the nonlinear spring constant k_3.

For a positive value of the Duffing coefficient, the total effective spring constant of a resonator increases, leading to a spring-hardening effect. The influence of a positive k_3 is highlighted in Figure 2.1 a, which shows the amplitude response of a resonator for increasing driving forces. Upon increase of the driving force, the response transitions from a purely linear response at low amplitudes to a nonlinear response at high amplitudes. Because of the amplitude-dependent membrane stiffening, the resonance frequency changes with amplitude, as apparent when inserting k_{eff} into Equation 2.5 as:

$$\omega_0 = \sqrt{\frac{k_{eff}}{m}} = \sqrt{\frac{k_1 + k_3 x^2}{m}}. \tag{2.21}$$

This shifts the amplitude response curves to the right at increasing driving forces. For a negative Duffing coefficient, the amplitude response curve would be shifted to the left side, leading to a mirrored image of Figure 2.1 b. In an upwards frequency sweep experiment, the amplitude response increases until the driving frequency exceeds the resonance frequency. At that point, the amplitude suddenly drops to a lower value and follows the solid curves on the right side of the graph. In a reverse frequency sweep where the frequency is swept from high to low, the amplitude remains low until it suddenly jumps upward. The points where the amplitude suddenly drops or increases are called saddle node bifurcations (SNB). In the frequency range between the SNBs, three solutions of the steady state amplitude equation (Equation 2.18) exist. For each driving force, the stable solutions are plotted as solid lines, while the dotted line represents the unstable solution.

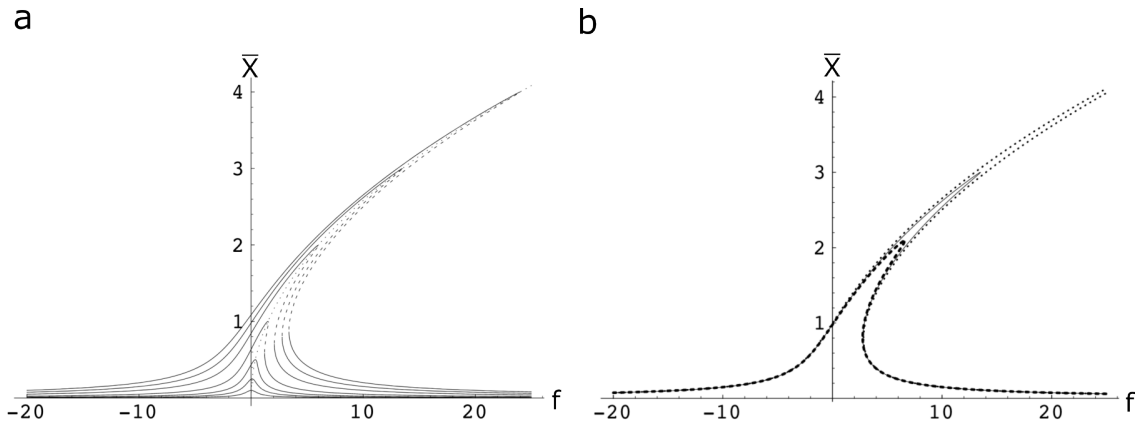

Figure 2.1: (a) Influence of the amplitude-dependent stiffness on the amplitude response of a resonator subject to increasing driving powers and a positive value of the Duffing coefficient. Solid lines represent the stable solutions, while dotted lines represent unstable solutions. (b) Change of the amplitude response of a nonlinear resonator in presence of nonlinear (dashed line) and linear (thin solid line) damping effects and without any damping (dotted line) for a constant driving force. The plots are reproduced from [32].

The amplitude response curves plotted in Figure 2.1 a allow for fitting a backbone curve, which enables the extraction of the Duffing coefficient. This will be particularly relevant in the experimental part of this thesis, and will be discussed in more detail in subsection 3.5.2.

When considering nonlinear damping processes that lead to dissipation of the resonator's energy during oscillation, the amplitude response curve is slightly modified. In Figure 2.1 b, the amplitude response of a resonator is shown without nonlinear damping, with slight nonlinear damping and without any kind of damping ($Q \to \infty$), while keeping the driving force constant. The response of a resonator without nonlinear damping, but finite quality factor is represented by the thin solid line. Under the influence of nonlinear damping effects, the response is modified to follow the thick dashed line, showing a reduction of the amplitude. In the case of no energy dissipation, the amplitude response is represented by the dotted line. It is worth noting that all curves lie on the same backbone, independent of the presence of nonlinear damping.

3

Materials and Methods

3.1. Molybdenum Disulfide

After the discovery of scalable routes for the production of graphene in 2004, research on this compound has been carried out extensively to study and modify the outstanding properties this compound offers [33]. However, the absence of a band gap has been limiting the applicability of graphene in logical electronic devices or optical sensors, sparking research on other 2D materials. In this so-called post-graphene era, transition metal dichalcogenides (TMDCs) and more specifically molybdenum disulfide (MoS_2) are amongst the most studied and promising materials.

Monolayer MoS_2 is a semiconducting 2D material with a direct bandgap of 1.8 eV and other promising optical and electrical properties, making it a suitable candidate for the design of nanoscale optical and electrical devices like field effect transistors (FET), photodetectors and solar cells [34, 35]. One monolayer of MoS_2 is made up of three covalently bound hexagonal layers (trilayer structure), namely one molybdenum layer which is sandwiched between two sulfur layers. Six sulfur atoms thus coordinate each molybdenum atom, and each sulfur atom is coordinated by three molybdenum atoms. In Figure 3.1 a) and b), the pristine trilayer structure is depicted from different perspectives. The atomic structure strongly resembles the honeycomb structure of graphene, but consists of two different atoms arranged in a trilayer structure.

As a result of the graphene-like honeycomb structure of monolayer MoS_2, this material has a high intrinsic stiffness and breaking strength. The Young's modulus and strength of MoS_2 are comparable to common steels, but values for the modulus vary significantly between experiments and simulations. Experimental examinations of the Young's modulus range from 270 ± 100 GPa [37] to 330 ± 70 GPa [38], while density functional theory (DFT) simulations report values down to 184 GPa [39]. The experimentally determined breaking strength of MoS_2 monolayers is reported to be 23 GPa [37].

3.2. Device Fabrication

3.2.1. Fabrication of Monolayer Membrane Resonators

In this thesis, the nonlinear response of circular optical cavities with monolayer membranes of MoS_2 is studied. The devices are fabricated via gold-assisted mechanical exfoliation from bulk crystals, with subsequent annealing. The samples were fabricated with a protocol developed in the group of Otakar Frank at the Czech Academy of Sciences, Czech Republic [40].

To create the nanomechanical cavities, substrate wafers of 310 nm SiO_2 on Si are used, with circular cavities etched through the oxide layer. On the chip, the cavity diameter ranges from 2 µm to 6 µm. By etching through the oxide, cavity depths of 310 nm are achieved and a silicon back mirror is created. The wafers are coated with a thin metal bilayer consisting of 3 nm of chromium (Cr) and

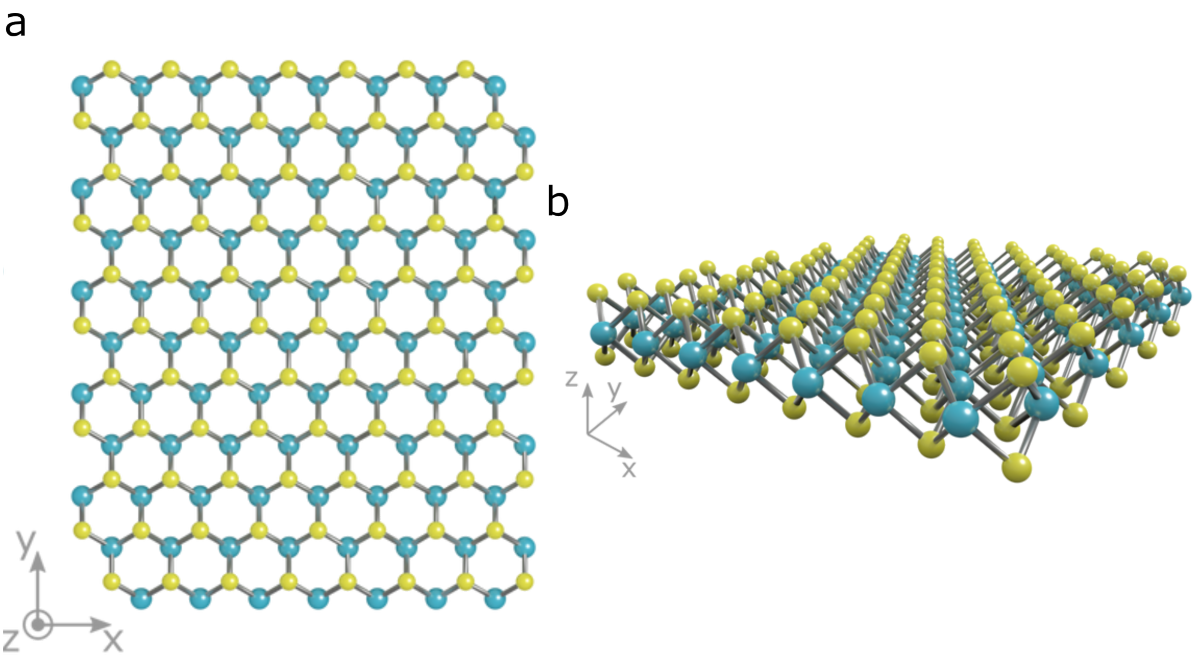

Figure 3.1: Pristine, defect-free monolayer of MoS_2 in (a) the top view and (b) from the side [36]. Yellow spheres represent sulfur atoms (S), while blue represents molybdenum (Mo).

15 nm of gold (Au) via magnetron sputtering (Quorum Q300T-D). The addition of a thin gold layer has been demonstrated to enhance the adhesion of mechanically exfoliated transition metal dichalcogenide (TMD) monolayers by leveraging gold's resistance to oxidation. This facilitates large-area exfoliation of the two-dimensional material by enhancing van der Waals adhesions between the TMD layer and the substrate [41].

To fabricate cavities with suspended monolayers of MoS_2, the monolayers were exfoliated from natural crystals. The crystals were pressed on the exfoliation tape (Nitto EPL-BT-150E-KL) and are thinned a maximum of twice. Then, the tape is pressed onto the sample, with subsequent heating to 100 °C for 30 minutes. This has been demonstrated to increase the yield of cavities covered by a monolayer [42]. To further maximize the yield, constant pressure was applied to the tape during the annealing step, which improves adhesion of the material to the gold surface. Once the substrate is cooled down to room temperature, the tape is removed. The sputtering and exfoliation processes are performed quickly to reduce exposure of the sample to reduce exposure to the environment. This is done to reduce adsorption of volatile organic compounds to the sample.

Figure 3.2a shows an optical microscope image of the chip used in this thesis. The drums with diameters of 3-6 µm are covered with MoS_2, which has a different color depending on the thickness. As the thickness increases, the color of MoS_2 changes from purple to blue and eventually silver for very thick flakes. Figure 3.2b highlights the color difference between a monolayer and multiple layers of material. In the purple multilayer flake, suspended membranes over the cavities appear with a yellow hue.

3.3. Atomic Force Microscopy

To analyze the surface texture and quality of the suspended membranes, Atomic Force Microscopy (AFM) measurements are performed. The measurements are performed with an Asylum Research Cypher AFM and Bruker silicon tips on a silicon nitride cantilever. The cantilever has a thickness of 0.6 µm, a length of 27 µm and a width of 32 µm. Additionally, its resonance frequency is 1400 kHz with a spring constant of 18 N/m.

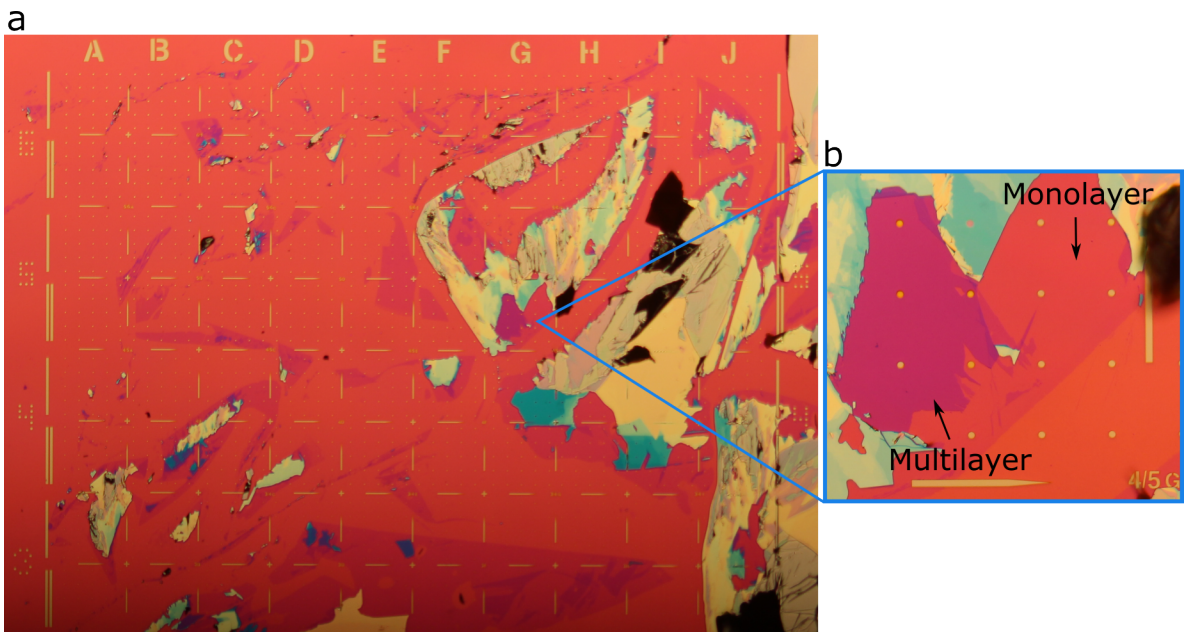

Figure 3.2: (a) Optical microscope image of the Si/SiO_2 chip with circular cavities ranging from 3 to 6 µm in diameter. The exfoliated MoS_2 shows a thickness dependent color, with thin flakes appearing purple and thick flakes appearing silver. Flakes with intermediate thickness appear blue. (b) Difference in optical contrast of monolayer and multilayer MoS_2. Suspended membranes in multilayer flakes appear with yellow hue.

3.4. Actuation and Detection

3.4.1. Optothermal Actuation and Laser Interferometry

To study the mechanics of two-dimensional materials in the form of membrane resonators, various different actuation and detection techniques have been developed. To excite membranes into harmonic vibrational motion, techniques like acoustic actuation, magnetic actuation, thermal gradient actuation, electrostatic actuation or optothermal actuation are possible. Among these, electrostatic and optothermal actuation have been widely studied and applied to actuate resonators of various architecture like beams, cantilevers, and membranes [43, 44].

Electrostatic actuation is a widely applied actuation technique and offers comparably simple implementation, precision and fast response. This technique exploits electrostatic forces, which can be generated between a suspended 2D material membrane and a gate electrode once a potential difference is applied. However, this technique requires two clearly separated electrodes without electrical contact to allow the formation of electrostatic forces to actuate the membrane. As presented in the previous section, the gold-assisted exfoliation of MoS_2 and graphene is achieved by gold sputtering on the substrate. The sputtering process does not allow precise control of the coated areas, and thus gold atoms are sputtered not only on the SiO_2 top layer, but are likely to be deposited into the cavity. For electrostatic actuation, this could lead to significant experimental difficulties due to the high risk of short circuits and the reduction of the dielectric insulation between the electrodes.

Optothermal Actuation

Besides electrostatic actuation, optothermal actuation has gained significant attraction for its efficiency, versatility and non-contact approach, making it an ideal candidate to develop an all-optical analysis procedure for the characterization of mechanical properties of 2D materials. In contrast to electrostatic actuation, it does not require the application of a voltage between membrane and back electrode, making it well suited for samples produced through gold-assisted exfoliation. Instead, the actuation happens

via a power-modulated laser that is focused on the membrane. This leads to modulated absorption of light by the membrane and causes subsequent heating and cooling. The alternating heating and cooling leads to thermal expansion and contraction, which effectively drives the membrane into oscillation. If the membrane is initially deflected downwards in the direction of the silicon substrate, thermal expansion causes a downwards deflection of the membrane, indicated by the red dashed line in Figure 3.3a. Upon cooling, the membrane contracts and is deflected upwards, as represented by the blue dashed line. This behavior applies to materials with a positive thermal expansion coefficient, while materials with a negative coefficient would exhibit the opposite trend. The expansion and contraction leads to reduced or increased distances between the semi-transparent membrane and the silicon mirror, which are different from the initial distance g_0.

Laser Interferometry

This actuation method integrates seamlessly with interferometric readout, enabling the proposed all-optical, non-contact approach. 2D material membranes of graphene and MoS_2 are suited for optical actuation and readout methods due to their specific optical, thermal and mechanical properties [31, 45]. They exhibit high optical absorption and thermal conductivity while being mechanically flexible to sustain large oscillations. Interferometric readout of nanomechanical membrane resonators is often accomplished by employing a Fabry-Pérot-interferometer, which is formed by the semi-transparent membrane and the highly reflective silicon substrate acting as a mirror. In such a Fabry-Pérot-interferometer, a readout laser is focused on the cavity and its power is modulated by the oscillating membrane in the cavity. This modulation of the readout laser contains information about the vibrational amplitude of the membrane and can be explained by two distinct phenomena [22]. After the readout laser passes through the optical cavity, it is transformed to an electrical signal with a photodiode. The diode converts incoming photons to a photocurrent which is proportional to the incident light intensity.

The first phenomenon is depicted in Figure 3.3 a and relies on interference of the readout laser. Due to the semi-transparent nature of the membrane, parts of the incoming light are reflected while others get transmitted through the membrane towards the silicon mirror. The transmitted rays are depicted by the gray line and can constructively or destructively interfere with the rays reflected at the oscillating membrane (blue and red arrows). The type of interference depends on the optical path difference between the rays, affecting the detected signal strength.

The second phenomenon that modulates the power of the readout laser is illustrated in Figure 3.3 b, and shows a cross-section through the optical cavity with the corresponding interfaces and membrane-silicon distance g_0. Additionally, the electric field of the readout laser is depicted in red. Since the readout laser reflects off the silicon substrate at the silicon-vacuum interface, the boundary condition requires the electric field to approach zero. This results in a standing wave pattern with alternating nodes and antinodes of electric field intensity. As the membrane, which absorbs part of the light due to its non-zero imaginary part of the refractive index, moves through this standing wave, the amount of light absorbed by the membrane varies depending on its position relative to the standing wave's intensity distribution. During this process, it is assumed that the membrane is sufficiently transparent such that the change in electric field of the standing wave is negligible. Maximum absorption occurs when the membrane is positioned at an antinode, where the electric field amplitude is highest. Minimal absorption occurs at nodes where the field amplitude is near zero.

The combination of these two mechanisms determines the final signal strength received by the photodiode. The total reflectivity of the optical cavity is significantly influenced by the thickness of the oscillating membrane and the cavity depth g_0. Figure 3.3 c shows the responsivity of an optical cavity formed by a silicon substrate and MoS_2 with varying membrane thickness and cavity depth g [47]. The responsivity is the derivative of the reflectivity with respect to the cavity depth, and thus shows the regions of strongest reflectivity change. It is desirable to design a cavity with a high responsivity, since this ensures optimal detection of even small membrane displacements. Thus, a high responsivity results in a stronger detectable signal change, increasing the signal-to-noise ratio (SNR). As apparent from Figure 3.3 c, the responsivity of a single layer of MoS_2 suspended over a cavity is significantly lower compared to multilayer MoS_2 and only changes marginally with cavity depth. This has drastic consequences for the experimental work throughout this thesis. Since it is desired to study the Young's

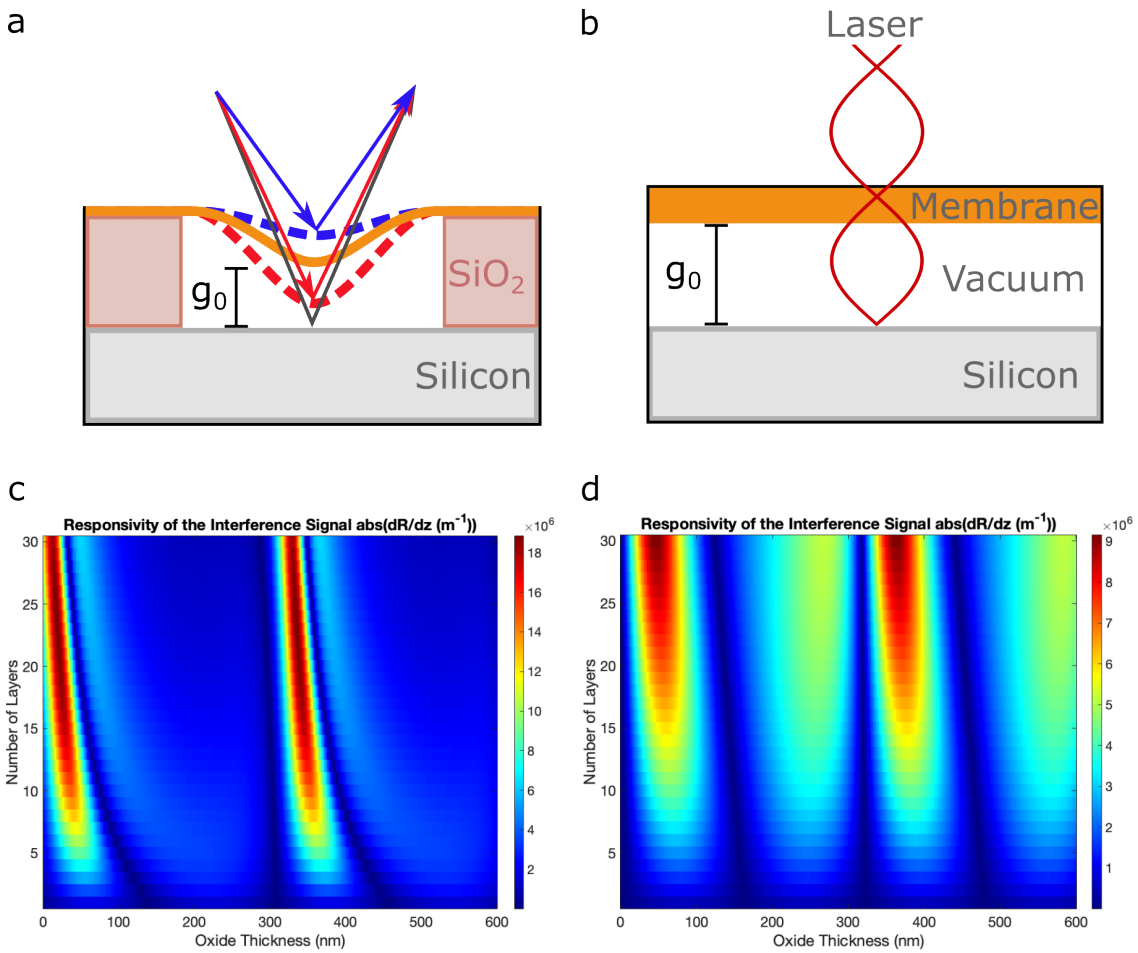

Figure 3.3: (a) Horizontal schematic of the optical cavity formed by the silicon back mirror and the semi-transparent 2D material membrane. When the membrane is optothermally excited, repeated thermal expansion and contraction induce vibrational motion. Incident light from the readout laser is reflected by both the back mirror and the membrane, creating a path difference between the rays. This path difference, which varies with the membrane's position, results in constructive and destructive interference, leading to intensity variations detected by the photodetector. (b) The readout laser forms a standing wave inside the cavity. Oscillation of the membrane through the standing wave leads to variations in the absorbed light by the membrane, thus modulating the light intensity sensed by the photodiode. (c) Dependence of the calculated responsivity of the interference signal on the oxide thickness for varying number of layers of MoS_2 and (d) graphene. The calculation is based on [46, 47], assuming a monolayer thickness and complex refractive index of 0.65 nm and 4.0 - 1.0*i* for MoS_2, and 0.335 nm and 2.6 - 1.3*i* for graphene [46, 48]. These values of the complex refractive index were obtained for a wavelength of 633 nm, corresponding to the wavelength of the readout laser. (a) and (b) are adapted with permission from the master thesis of Álvaro Bermejillo Seco, Delft University of Technology.

modulus of monolayer 2D material membranes, signal detection is very challenging and requires careful experimentation, laser alignment and positioning.

3.4.2. Experimental Setup

The experimental setup used to achieve all-optical actuation and detection of 2D material membrane resonators is displayed in Figure 3.4. A red helium-neon laser (HeNe) laser of wavelength $\lambda = 632.8$ nm is used to obtain information about the oscillation amplitude via interferometry. The light emitted from the laser is linearly polarized and is first passed through two neutral density (ND) filters, which

are positioned right after the laser. The purpose of the ND filters is to reduce the intensity of the light reaching the sample to avoid temperature-related influences on the membrane. The first ND filter is continuous, while the second is a filter wheel consisting of eight different filter strengths. For the experiments, the filters were set to their lowest attenuation to maximize the signal on the photodiode (see subsection 3.4.1) if not stated otherwise. Next, the red light passes through a beam expander (BE), which broadens the beam to allow maximum focussing of the light with the objective lens placed above the sample chamber. After the BE, a 1/2-waveplate and polarized beam splitter (PBS) are mounted. The 1/2-waveplate is placed in front of the PBS to control the polarization of the light for optimal beam splitting. It is set to rotate the incoming polarized light to match the PBS. In the PBS, the incident light is split into two orthogonal polarization components, where one is directed to the sample chamber and the other to a photodetector (Newport 1801). The beam that is directed onto the sample is passed through a 1/4 wave plate, transforming the linear polarization to elliptical polarization. Upon return from the sample, the reflected light gets transformed from elliptical to linear polarization, while being rotated by 90° to reach the photodetector through the PBS. Thus, the 1/4 wave plate ensures combination of both light paths to reach the photodetector. In front of the photodetector, a lens is placed to focus the light on the active area of the detector.
After the 1/4 wave plate, the light continues to the objective, where it is focused on the sample inside the sample chamber. The sample chamber is kept at a vacuum of 10^{-5} mbar, and contains a heating element to control the device temperature. During the experiments, the heating element was set to 310 K to achieve a stable temperature. Further, the sample chamber is mounted on an open-loop piezoelectric stage, which allows precise positioning of the sample within three dimensions. The insets on the lower side of Figure 3.4 show a close-up of the sample chamber, where a silicon chip containing multiple suspended membranes is positioned on the heater (right inset). The inset in the middle shows a suspended membrane over a cavity, which can be identified by its stronger yellow appearance (as indicated by the arrow). The inset on the left side shows a cross-section of the actuation and detection process achieved with the red and blue laser.

To actuate the membrane optothermally, a blue laser diode of wavelength $\lambda = 405$ nm is used. The diode is powered via a Thorlabs LDC 205 C laser diode controller, which is set to 45 mA for all measurements. An optical fiber connects the blue laser diode to a free-space coupler, which sends the light to a lens before it reaches a cold mirror. This cold mirror serves the purpose of introducing the blue light into the optical path of the red light, without altering the red laser's incidence angle on the sample. It reflects the blue light while allowing the red laser to pass through unaffected. From the cold mirror, the blue laser passes through the objective and is focused on the same spot as the red readout laser.

To position a membrane right at the focus point of the blue and red laser for optimal actuation and detection, a camera is used in combination with a torch as a white light source. The white light is directed through two beam splitters to facilitate introduction into the optical path of the blue and red laser. During the measurements, the white light is turned off and the beam splitter is removed from the optical path of the red and blue laser to increase the signal at the photodiode. The removal of the beam splitter for the white light during the measurements has a drawback for the laser positioning. With the beam splitter for the white light in place, the blue and red laser are positioned in the center of a membrane. When the beam splitter is flipped out of the beam during the measurement, the red and blue laser have a slightly different path than with the beam splitter in place. To compensate for the altered position of the lasers on the membrane, the obtained signal is maximized by manually adjusting the sample position with the piezoelectric stage.

The vector network analyzer (VNA, Rohde & Schwarz Model ZNB 4) used in this setup is a key component for the detection of the frequency response of the nanomechanical cavity. In addition to the DC power the blue laser is supplied with, the VNA outputs an AC signal to the blue laser diode. This AC signal effectively modulates the intensity of the blue laser sinusoidally to achieve optothermal actuation. Simultaneously, it is connected to the photodetector and measures the reflected intensity from the cavity. Thus, the VNA has the ability to measure the frequency-dependent response of the resonating membrane by relating the modulated power of the blue laser (input) to the received photodetector signal (output). To measure the linear and nonlinear response of the membrane, the forward transmission coefficient (S_{21}-parameter) is measured, which represents the ratio of the output signal from the photodetector over the input signal directed to the blue laser diode. In a frequency sweep, the S_{21}-parameter will show a high intensity when the membrane is driven at resonance. Such resonance

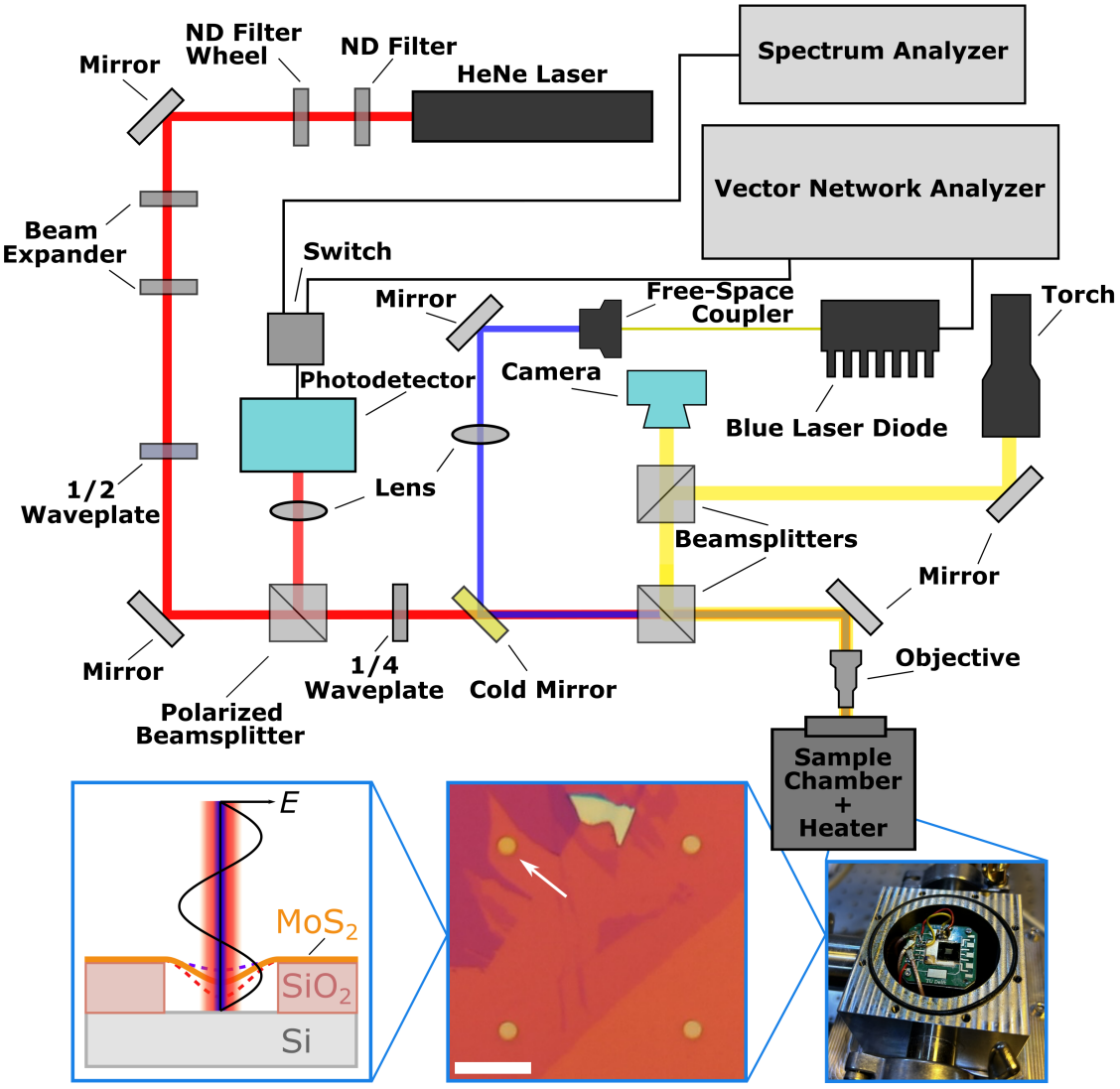

Figure 3.4: Laser interferometry setup comprised of the red and blue laser paths for actuation and detection and the white light path used for positioning. To switch between the measurement using a spectrum and a vector network analyzer, a switch is used. The basic optical and electronic components are highlighted and the insets in the lower side of the image show a close-up of a sample in the sample chamber, a suspended monolayer MoS_2 drum resonator and a schematic of the device architecture and cavity from a horizontal view. The scale bar is 20 µm. Adapted with permission from [49].

peaks are of central importance to study nanomechanical phenomena and extract the Young's modulus.

Besides the VNA, a spectrum analyzer (SA, Rohde & Schwarz FSL) is connected to the photodiode. The SA is used to conduct measurements of the temperature-related Brownian motion of the membrane, which will be further explained in the next section. By using a switch, the RF signal from the photodiode can be diverted to either the SA or the VNA, depending on the desired measurement.

3.5. Extraction of Resonator Parameters

The goal of this thesis is the calculation of the Young's modulus of the resonating membranes by employing optical actuation and detection. The thesis builds upon a method developed by Davidovikj *et al.*, which enables the calculation of the Young's modulus of multilayer graphene and MoS_2 membranes using nonlinear dynamics [22]. By extracting the nonlinear spring constant k_3, it is possible to calculate

the Young's modulus of a membrane resonator from:

$$E = \frac{(1.27 - 0.97\nu - 0.27\nu^2)R^2}{\pi h} k_3. \tag{3.1}$$

This equation relates the Young's modulus to the nonlinear spring constant via the Poisson ratio ν, the drum radius R and the membrane thickness h. The authors employed the steady-state amplitude solution of the Duffing equation to fit experimental data with a least-squares optimization algorithm, with k_3 as the sole fitting parameter. This yields accurate results for the Young's moduli of the studied materials, but requires an estimation of the drum mass as a parameter in the steady-state solution. Such mass estimations based on the density and volume of the membrane resonator can be particularly inaccurate for monolayers due to large mass deviations caused by environmental moisture, contamination, or lattice defects from the production and transfer methods. Masses were shown to deviate by up to 600 % compared to the theoretically estimated mass [23, 31].

To address these uncertainties, this thesis proposes a novel method to extract relevant resonator parameters without relying on mass estimations. It expands the method of Davidovikj *et al.* by employing optical amplitude calibration and direct measurements of the resonator mass via its thermally driven Brownian motion, also referred to as thermomechanical calibration [24, 29]. Furthermore, temperature fluctuations are accounted for by applying a method developed by Li *et al.*, which will be explained later in the text [50]. For the calculation of the Young's modulus, three measurements are required per resonator, which are conducted using a vector network analyzer (VNA) and a spectrum analyzer (SA). A flowchart illustrating the procedure and the key resonator parameters is presented in Figure 3.5, where the three measurements are indicated by blue and orange borders. The measurements consist of the calibration of the resonator's amplitude, the examination of its nonlinear behavior and the thermomechanical calibration step.

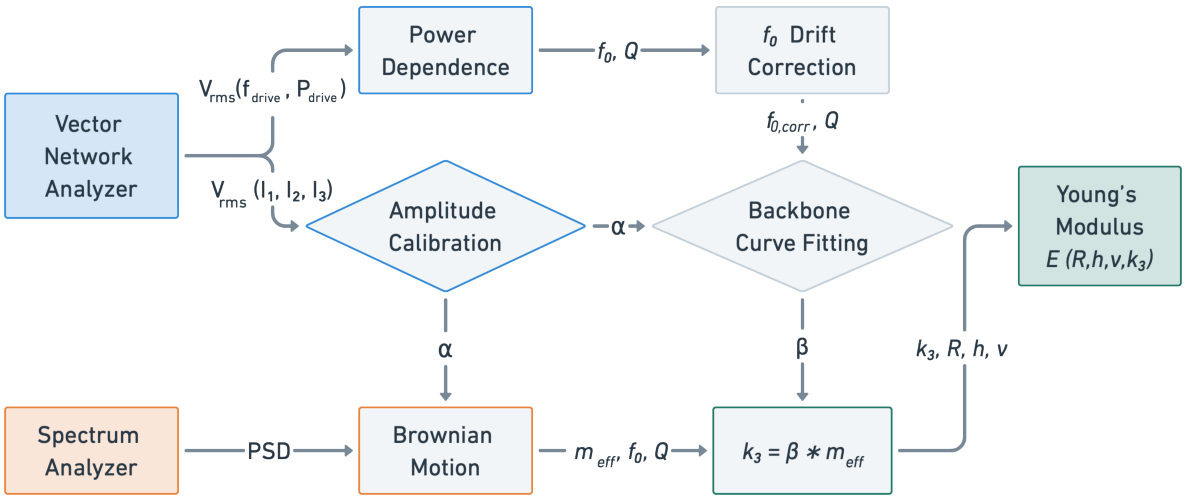

Figure 3.5: Flow chart representing the proposed all-optical approach to extract the Young's modulus of a 2D material membrane. First, two measurements are conducted with the VNA to obtain the transduction factor α and the mass-normalized Duffing coefficient β. The Duffing coefficient is obtained from a power-dependence measurement, which measures the amplitude response of the resonating membrane at increasing driving force. The power dependence measurement requires temperature correction to facilitate the fitting of the backbone curve to obtain β. The amplitude calibration measures the harmonics of the fundamental mode (I_1, I_2, I_3) to obtain the transduction factor, which allows transformation of the VNA signal in volts to an amplitude in nm. The Brownian motion measurement from the spectrum analyzer gives the power spectral density of the membrane's thermal fluctuation. Together with the transduction factor from the amplitude calibration step, the effective mass can be fitted and an assumption of the drum mass is not needed. Finally, the non-normalized duffing coefficient k_3 is calculated from β and m_{eff}, from which the Young's modulus can be derived directly.

To conduct the measurements, a drum with a suspended monolayer is selected on the chip. An undamaged cavity with a suspended monolayer of graphene or MoS_2 can be distinguished by its optical contrast relative to a cavity without a suspended material layer. The contrast is influenced by the thickness of the suspended membrane, the distance to the substrate, the substrate itself and the used wavelength [46, 51]. For the devices used in this thesis, suspended monolayers of MoS_2 appear with a yellowish contrast, compared to a white color of the cavities without suspended membrane. The optical appearance of an MoS_2 monolayer on silicon is depicted in the middle inset of Figure 3.4.

Once a suspended monolayer is identified, its resonance frequency of the fundamental mode and nonlinear behavior are examined using the VNA. If significant nonlinearity is observed, the presence of harmonics up to the third order is verified to enable amplitude calibration. From the equation for the resonance frequency $\omega_0 = \sqrt{k_1/m}$, it follows that the resonance frequency is inversely proportional to the mass of the membrane. This poses a challenge for detecting higher harmonics, as the photodiode is designed to operate within a bandwidth of 125 MHz, beyond which its response attenuates significantly. Due to their low mass, monolayer membranes exhibit higher resonance frequencies compared to a multilayer membrane of the same diameter. This can be problematic for the detection of the higher harmonics, because the photodiode is designed for operation up to a bandwidth of 125 MHz. Beyond that, the signal response of the photodetector attenuates significantly. Monolayer membranes have very low mass, leading to comparably high resonance frequencies as opposed to multilayer membranes.

Once higher harmonics are detected, the signal strength of the membrane's Brownian motion is assessed. If a clear signal is observed, all three measurements are conducted consecutively without changing the laser position on the resonator. The significance of a continuous measurement protocol is discussed in the following section.

3.5.1. Amplitude Calibration

The calibration of the amplitude is a crucial step towards the extraction of the nonlinear spring constant and the effective mass. This experimental step yields the transduction factor α (V^2/m^2), which describes the amount of voltage generated by the photodiode per meter of displacement of the resonator. Thus, the transduction factor allows the transformation of a VNA signal in V/V to information about the resonator's displacement in nm. The method of optical amplitude calibration was developed by Dolleman *et al.* and exploits the generation of higher harmonics resulting from nonlinear optical transduction [24].

In Fabry-Pérot interferometry of nanomechanical cavities, the reflected intensity received by the photodiode periodically changes as a function of the distance between the semi-transparent membrane and the reflecting back mirror. At low vibrational amplitudes of the membrane, the dependence of the detected optical signal can be approximated to be linearly dependent on the mirror to mirror distance. At high vibrational amplitudes, however, this assumption of linear transduction is invalid, and optical nonlinearities become relevant. The nonlinearities give rise to higher harmonics at integer multiples of the fundamental resonance frequency, providing valuable information about the vibrational amplitude δ, the average membrane position g and most importantly, the transduction factor α. By assuming a sinusoidal motion of the resonating membrane, mathematical formulas for δ, g and α are developed using ratios of the harmonics up to the third order.

The vibrational amplitude δ can be calculated from the third ($I_{3\omega}$) and first ($I_{1\omega}$) harmonic via:

$$\delta = \frac{2\sqrt{6I_{3\omega}/I_{1\omega}}}{\sqrt{\gamma^2 - I_{3\omega}/I_{1\omega}\gamma^2}}, \tag{3.2}$$

with $\gamma = 4\pi/\lambda$ and λ as the wavelength of the readout laser ($\lambda = 633nm$). From the amplitude δ, it is possible to calculate the average position g via the ratio of the second to the first harmonic $I_{2\omega}/I_{1\omega}$:

$$g = \frac{1}{\gamma}\left(\pi n + \arctan\left(\frac{12\delta\gamma - \delta^3\gamma^3}{(6\delta^2\gamma^2 - 48)I_{2\omega}/I_{1\omega}}\right)\right). \tag{3.3}$$

In this equation, n is a positive integer and requires knowledge of the estimated average position based on the production process [24]. For the device architecture used in this thesis, a value of $n = 2$ is chosen [24].

Finally, the square root of the transduction factor can be calculated from the equation:

$$\sqrt{\alpha} \approx \frac{I_{1\omega}}{\delta}, \tag{3.4}$$

with $I_{1\omega}$ as the measured root-mean-square (RMS) voltage V_{RMS} of the fundamental harmonic.

At high vibrational amplitudes, nonlinear transduction effects can influence the amplitude, leading to an error in the calculation of δ. It is possible to account for this source of error by calculating the corrected amplitude δ_{corr} from [24]:

$$\delta_{corr} = \left(1 + \frac{1}{8}\left(\frac{I_{1\omega}}{\sqrt{\alpha}}\right)^2 \gamma^2\right) \frac{I_{1\omega}}{\sqrt{\alpha}}. \tag{3.5}$$

The output signal of the VNA (S_{21}) is given as a complex ratio of the output signal of the photodiode (V_{out}) over the reference or input signal modulating the blue laser (V_{in}) as:

$$S_{21}[V/V] = \frac{V_{out}}{V_{in}}. \tag{3.6}$$

To convert this to V_{RMS}, the input RMS-voltage $V_{in,RMS}$ must be known. With the impedance Z of the VNA (50 Ω) and the RMS input power $P_{in,RMS}$ in dBm, the input voltage is calculated via:

$$V_{in,RMS} = \sqrt{ZP_{in,RMS}} = \sqrt{\frac{Z}{1000} 10^{\frac{P(dBm)}{10}}}. \tag{3.7}$$

Finally, the output RMS voltage is obtained with:

$$V_{out,RMS} = S_{21}\sqrt{\frac{Z}{1000}} 10^{\frac{P(dBm)}{20}}. \tag{3.8}$$

The transduction coefficient α plays a crucial role for the rest of the measurements and is a direct input parameter for the fitting of the duffing coefficient and the effective mass. The value of α is highly sensitive to the positioning and focus of the readout laser on the drum, as well as to variations in laser intensity [22]. Thus, it is important to perform a continuous set of measurements to ensure validity of the transduction factor across all measurements.

3.5.2. Laser Interferometry in the Nonlinear Regime: Power Dependence

The second measurement with the VNA examines the power dependence of the resonator by step-wise increasing the power modulation of the blue laser. This changes the driving force accordingly, leading to a transition of the resonator's behavior from the linear to the nonlinear regime. The power-dependence is measured from -40 dBm to 10 dBm for each drum to capture this transition. Then, the backbone curve can be applied:

$$f_{\mathsf{max}}^2 = f_0^2 + \frac{3}{16\pi^2}\beta \bar{X}_{\mathsf{max,nl}}^2, \tag{3.9}$$

which allows extraction of the mass-normalized Duffing coefficient β [26, 50, 52]. The backbone curve relates the frequency at the maximum of the amplitude response f_{max}^2 to the fundamental resonance frequency in the linear regime f_0^2, the maximum displacement of the nonlinear response $\bar{X}_{max,nl}^2$ and the mass normalized duffing coefficient. β can then be extracted by fitting the backbone curve to multiple frequency response curves To obtain the amplitude response data in nm, the VNA signal (V_{RMS}) is

converted to an absolute displacement in nm by applying Equation 3.2 with the transduction factor obtained from the amplitude calibration.

Upon increase of the power modulation, the temperature of the drum can fluctuate, which leads to changes in the tensile stress of the membrane due to thermal expansion. In membrane resonators, the tensile stress is the core parameter that influences the resonance frequency (section 2.1). Thus, changes in resonance frequency are observed at increasing optothermal driving force [26], which ultimately leads to misalignment of the power-dependence curves. To compensate for the temperature-related shift of the power-dependence curves, a method presented by Li *et al.* is applied, which allows correcting for the influence of temperature by aligning the experimental dataset at the resonance frequency of the device in the linear regime [50, 52].

The alignment of the power dependence curves bases on the assumption that the influence of the cubic spring constant is negligible at frequencies far away from the resonance frequency. This is applicable, because the restoring force contribution from nonlinearities ($\propto \beta x^3$) is small due to small displacements x at frequencies away from the resonance frequency (Equation 2.15). To account for temperature fluctuations, a linear harmonic oscillator model is fitted to the nonlinear frequency response curves at frequency ranges far from the resonance frequencies. This fitting process provides estimates of the resonance frequency and quality factor. The fitting regions are manually selected to ensure a reasonable correspondence with the dataset. In the next step, the resonance frequency of a linear response curve is selected as the reference frequency, and the frequency difference between the fitted resonance frequency of the nonlinear response curve and the reference frequency is determined. Finally, the nonlinear curves are aligned with the reference frequency.

To perform the linear oscillator fitting, the following LHO model is used:

$$\bar{X}(f) = \frac{\bar{X}_{max,l}/Q}{\sqrt{(1-(f/f_0)^2)^2 + f^2(f_0/Q)^2}}, \tag{3.10}$$

where $\bar{X}_{max,l}$ is set to the maximum amplitude of the nonlinear curve $\bar{X}_{max,nl}$ to perform the fitting for f_0 and Q.

After correction for temperature fluctuations, the backbone curve can be fitted to provide the mass normalized nonlinear spring constant.

3.5.3. Mass Calculation using Brownian Motion

The transduction factor is not only relevant for the fitting procedure of β, but is a direct input parameter for the fitting process for the effective mass. In the thermomechanical calibration step, the membrane's Brownian motion is measured using a spectrum analyzer and exploits the relation between the membrane's temperature-related fluctuations and its mechanical response. This relation is given by the equipartition theorem, which is commonly applied to calibrate the displacement of a nanomechanical resonator via the transduction coefficient α [22, 29]. In this work, however, thermomechanical calibration is not used to obtain the transduction coefficient, but the effective mass.

The Brownian motion of a nanomechanical membrane arises from the collision of surrounding gas particles with the membrane. At temperatures above 0 K, the particles can transfer energy to the membrane, leading to a random vibrational motion often called thermal noise. Based on the equipartition theorem, the mean square amplitude of the thermal motion of the n-th mode of the resonator can be described as:

$$\langle x_n^2(t)\rangle = \int_0^\infty df S_{zz}(f). \tag{3.11}$$

Here, f is the frequency and $S_{zz}(f)$ the one-sided power-spectral density (PSD) of the membrane arising from thermal noise. The PSD of the n-th mode can be written as:

$$S_{zz}(f) = \frac{k_B T f_n}{2\pi^3 m_{\text{eff},n} Q_n \left[(f^2 - f_n^2)^2 + \left(\frac{f f_n}{Q_n} \right)^2 \right]}, \tag{3.12}$$

with f_n, Q_n and $m_{eff,n}$ as the resonance frequency, quality factor and effective mass of the mode, respectively [29]. Further, k_B is the Boltzmann constant and T the resonator temperature.

The PSD of the membrane resonators can be measured using a Spectrum Analyzer. By squaring the obtained voltage signal and dividing it by the measurement bandwidth, the PSD is obtained, with units of V^2/Hz. However, the measured signal does not purely correspond to the thermal noise of the membrane, but also contains environmental white noise S_{vv}^w as a flat additive and noise from the photodetector $S_{vv}^{PD}(f)$. Thus, the measured PSD from the spectrum analyzer can be written as:

$$S_{vv}(f) = S_{vv}^w + S_{vv}^{PD}(f) + \alpha S_{zz}(f), \tag{3.13}$$

with α as the transduction factor [29].

To calculate the effective mass of the fundamental mode, the PSD of the fundamental mode is measured without altering the laser position with respect to the amplitude calibration and power-dependence measurement. This ensures validity of the transduction factor across the set of consecutive measurements. During the measurement of the PSD, the blue actuation laser is turned off, and only the red laser illuminates the sample for interferometric readout. Then, the dark noise of the photodiode is measured with the red laser turned off.

By subtracting the measured dark noise from the PSD of the resonator, only a constant noise floor remains due to the white noise from the environment. By averaging in a frequency range away from the peak of the Brownian motion, the constant noise floor can be determined as is subtracted from the PSD. The remaining signal after subtraction of $S_{vv}^{PD}(f)$ and S_{vv}^w can be purely attributed to the thermal noise of the resonator $\alpha S_{zz}(f)$.

Because α is already known, it is possible to determine the effective mass by fitting the obtained thermal noise signal using Equation 3.12 multiplied with α. To obtain initial guesses for f_0 and Q, a LHO model is first fitted to the PSD. In the final step, the initial guesses of f_0 and Q are used to fit the effective mass m_{eff} to the PSD.

3.5.4. Calculation of the Young's Modulus

After all three of the measurements presented in Figure 3.5 were conducted consecutively, it is possible to calculate the Young's modulus by combining Equation 2.16 with Equation 3.1. With the value for β obtained from the power-dependence measurement, the non-normalized Duffing coefficient k_3 can be computed as:

$$k_3 = \beta \cdot m_{eff}. \tag{3.14}$$

Finally, k_3 can be inserted into Equation 3.1 together with the drum radius, Poisson ratio and membrane thickness to obtain the Young's modulus of the studied membrane.

4

Results and Discussion

4.1. Young's Modulus of Pristine MoS_2 Monolayers

To evaluate the proposed all-optical characterization method for determining the Young's modulus, the devices made from pristine monolayer MoS_2 are used, and the analysis procedure described in section 3.5 is followed closely. A total of 26 suspended membranes on the chip are tested for their nonlinear performance, Brownian motion, and presence of harmonics at varying drum diameters of 3 to 6 µm. Consecutive measurements on drums exhibiting the required nonlinear behavior and harmonics up to the third order are conducted on four drums (Drum 5, 12, 15 and 16), corresponding to an approximate yield of 15%. Notably, high actuation powers close to 10 dBm are required to detect signals from the harmonics. In most drums, the absence of third order-harmonics impeded amplitude calibration and further measurements. Nonlinear behavior and the required harmonics are observed in drums with diameters of 4 and 5 µm, with corresponding optical images shown in Figure 4.1. The proposed method is demonstrated in detail on one of the four drums (Drum 16), which consists of a MoS_2 monolayer suspended over a 5 µm diameter cavity.

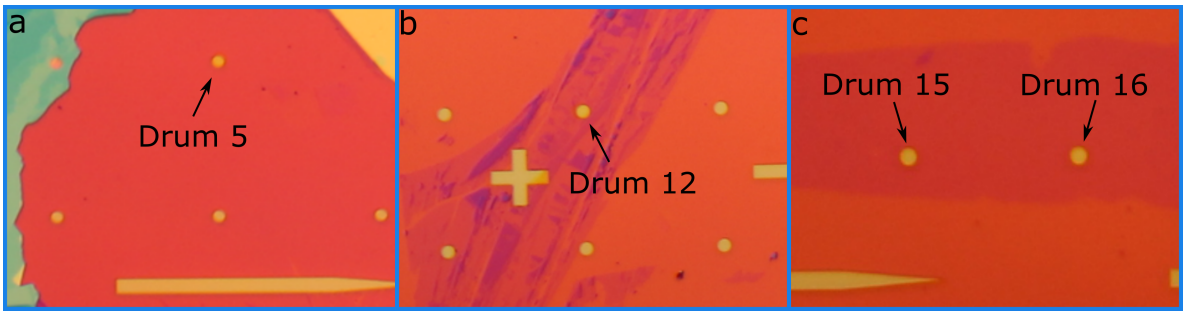

Figure 4.1: Overview of the nanodrums fabricated from pristine monolayer MoS2 via gold-assisted mechanical exfoliation. The diameters of the drums are (a) 4 µm for Drum 5 and (b-c) 5 µm for the Drums 12, 15 and 16.

Before the start of a measurement, the blue and red laser spots are positioned in the center of the drum using the white light source and the camera, with the corresponding beam splitter in the optical path of the lasers. The spot size of both the red and blue laser is approximately 1 µm. With the focus of both lasers at the height of the membrane, the white light source is turned off and the device's response to different driving frequencies is examined with the VNA. Once the resonance peak with the lowest frequency is identified, it is assumed to be the fundamental mode of the drum. All measurements conducted on this drum will be performed in the frequency range around this peak to ensure the validity of the equations and effective mass described in section 3.5.

To record the measurements, the beam splitter introducing the white light into the optical path of the

lasers was removed to direct the maximum intensity of the red laser to the photodiode. With the beam splitter in place, the third harmonics of the drums were not visible due to the reduction in laser intensity caused by the splitter. Removing the beam splitter during measurements resulted in a slight shift of the red and blue lasers away from the drum's center position. This required manual re-centering by maximizing the signal of the fundamental mode and higher harmonics in the VNA. The laser position on the drum was manually adjusted using the open-loop piezoelectric stage until the signal detected by the VNA reached its maximum.

4.1.1. Extraction of Device Parameters

In the beginning of the analysis, the resonance frequency of the fundamental mode was identified at approximately 40.45 MHz, and all measurements were conducted with the resonance frequency as the center frequency and a span of 10 MHz. Figure 4.2 presents the fundamental mode at very low driving powers of -34 to -22 dBm. With higher driving power, the amplitude of the resonator rises as expected due to enhanced thermal expansion and contraction. In addition to the presented amplitude response data at low driving powers, Figure 4.2 shows fits of a damped linear harmonic oscillator model to the experimental results. The fitting of an LHO model to the data at low power is justified under the assumption that nonlinearities are negligible due to the low amplitude. From the fits, it is possible to extract the resonance frequency and the quality factor, which are given in the legend for each driving power. The resonance frequencies are consistent between different driving powers, with minor variations arising from measurement noise and a limited number of measurement points.

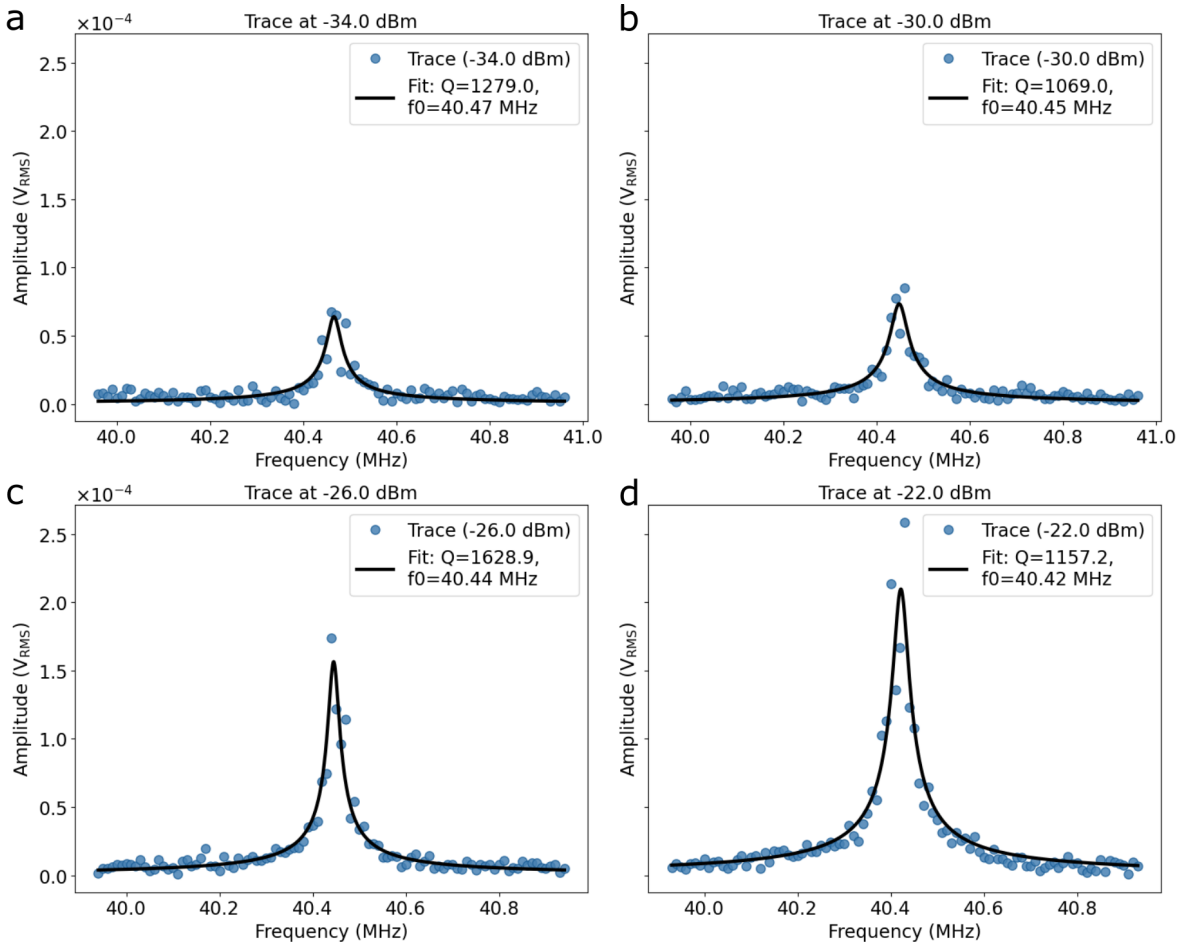

Figure 4.2: Experimental data and corresponding linear harmonic oscillator fits of Drum 16 at different driving powers. The Q-factors and resonance frequencies are stated for each power. The amplitude is given in V_{RMS}.

The extracted quality factors from the fits are remarkably high for 2D material resonators at room temperature, with values ranging from ~1000 to ~1600 at -34 to -22 dBm. In general, quality factors of such resonators are below 1000, with commonly reported values in the lower hundreds [53–56]. High quality factors are desirable in nanomechanical resonators due to an increase in precision of mass, pressure, and strain sensing as well as a reduced energy consumption for low-power devices [52, 57, 58]. A potential reason for the high quality factor could be the production method, if the suspended membranes are fabricated with very high pre-strain. Highly pre-strained membranes exhibit increased quality factors in comparison to membranes without pre-strain due to a phenomenon called dissipation dilution [59, 60]. As introduced in subsection 2.1.1, the quality factor represents the amount of stored over dissipated energy per oscillation cycle. In a highly pre-strained membrane, the increased pre-strain enhances the stored energy, while dissipation mechanisms remain largely unaffected. Consequently, the dissipated energy is effectively 'diluted' relative to the stored energy, leading to a higher quality factor.

Amplitude Calibration

After identification of the resonance frequency of the fundamental mode, the higher harmonics of this mode are measured to calibrate the vibrational amplitude. To avoid an influence of nonlinear damping and strong temperature-related shifts in the resonance frequency, the harmonics are measured at the lowest driving power, where the third harmonics are visible. For Drum 16, the harmonics are measured at 6 dBm and are presented in Figure 4.3 a. The first three harmonics are detectable and above the noise level, while the fourth harmonic is not visible. The transition point of the harmonics from the upper branch of the stable solution to the lower branch occurs at different frequencies, which can arise from fluctuations in the nonlinear response of the resonating membranes [24]. Such fluctuations in the nonlinear response could originate from thermal or measurement noise or slight variations in the driving force [24]. The variations in the transition points between the harmonics do not have negative consequences for the calculation of the ratios of the harmonics, since the backbone curve followed by the resonator is the same for all harmonics [24]. The amplitude, average position, and the square root of the transduction factor are calculated within a frequency window of 50 kHz, ending before the peak of the harmonic preceding the lowest peak frequency. The window used for calculating the harmonic ratios is indicated by the dashed vertical lines in the figure.

Figure 4.3 b-d show the amplitude of the resonating membrane, its average position and transduction factor calculated within the 50 kHz range. With 15 nm, the amplitude of the vibration is high compared to the thickness of a single layer of MoS_2 (6.5 Å [61]), but not so high that nonlinear effects play a role. This is in agreement with the similar amplitudes of the averaged δ and δ_{corr} of 15 nm. The extracted average position of 302 nm is in line with the depth of the cavity, which was extracted to be 304 nm. The cavity depth was measured with an AFM at multiple non-suspended cavities. The extracted square root of the transduction factor is 1.20×10^6 V/m, which corresponds to a value of 1.43×10^{12} V^2/m^2 for α. In contrast to the amplitude, which is expected to increase along the upper branch of the amplitude solution, g and $\sqrt{\alpha}$ are expected to be constant. This is in agreement to the values in Figure 4.3 c and d, which do not depend on the frequency.

Power-Dependence

After obtaining the transduction factor, the power-dependence measurement is conducted. During the measurement, the power modulation of the blue actuation laser is increased in increments of 2 dBm from -40 to 10 dBm and the amplitude response is measured. Figure 4.4 a shows a selection of amplitude responses in nm at different driving powers, from -22 dBm to 10 dBm. The amplitude is converted to nm with the transduction factor from the amplitude calibration step by dividing the measured V_{RMS} by $\sqrt{\alpha}$. These responses are also used for the fitting of the backbone curve to extract the normalized Duffing coefficient, which is shown in Figure 4.4 b.

The amplitude responses in Figure 4.4 a exhibit significant temperature-related fluctuations in their resonance frequencies, which requires aligning the resonance frequencies to enable fitting of the backbone curve. These temperature-induced shifts in resonance frequency become increasingly pronounced with higher driving power, with the amplitude response of driving at 10 dBm showing the strongest

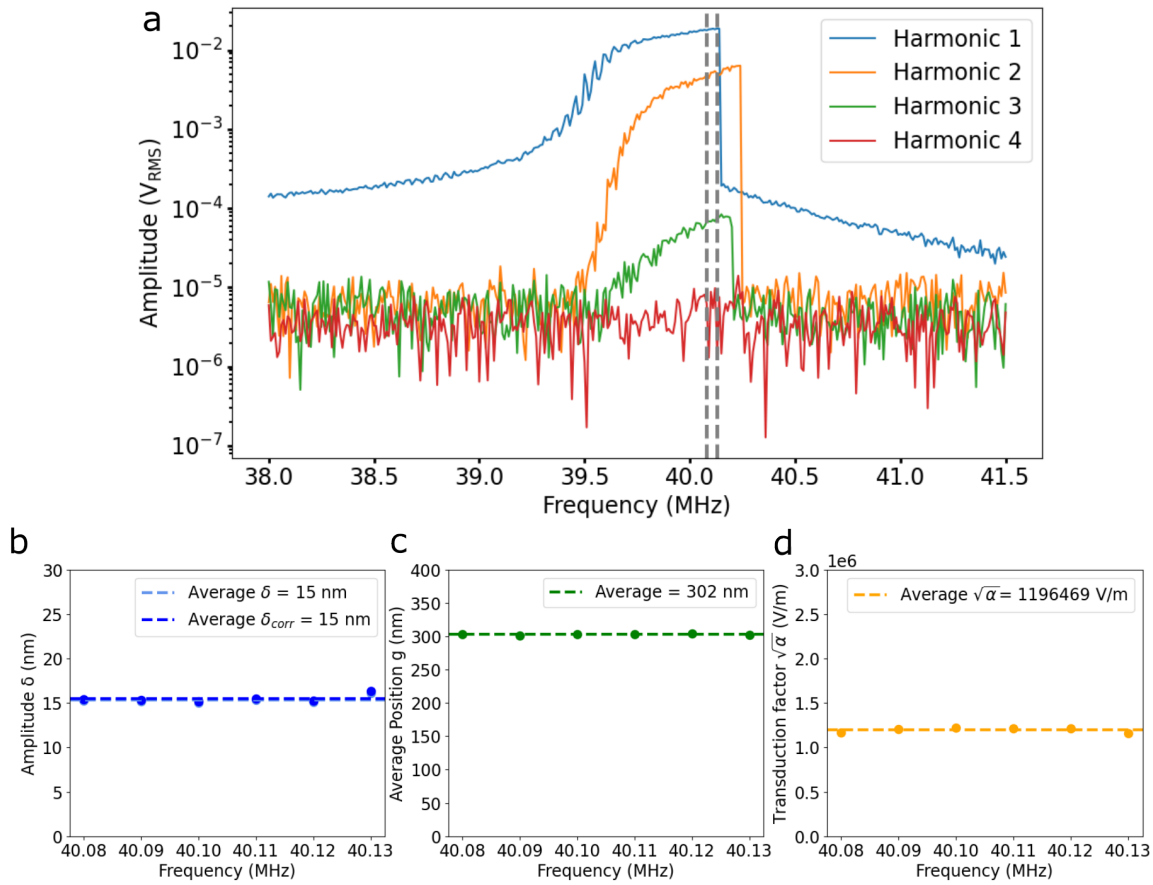

Figure 4.3: (a) Amplitude calibration of the membrane resonator using the harmonics of the fundamental mode. The harmonics were measured at 6.0 dBm to reduce the possibility of nonlinear damping and temperature-related shifts during the measurement. The vertical dashed lines indicate the frequency window where the amplitude, average position and transduction factor of the resonator were computed. (b) Amplitude of the resonator with and without correction for nonlinear optical transduction. Due to the low amplitude, nonlinear optical transduction effects are negligible. (c) Average position and (d) transduction factor of the membrane resonator.

shift. An increase in power modulation leads to a rise of the membrane temperature due to the limited thermal conduction of the membrane. At high irradiation intensities, the generated heat is not fully dissipated during the subsequent cooling cycle, causing a cumulative temperature increase. The increase in membrane temperature results in thermal expansion of the membrane, which in turn reduces the overall tension in the membrane [62]. The reduced tension in the membrane lowers its stiffness, and thus the resonance frequency (see Equation 2.5) [62].

To correct for the frequency shifts, the amplitude response at each driving power is fitted with a LHO model at frequencies with an amplitude well below 1 nm. At such low amplitudes. the effect of nonlinearities is negligible. The fitted curve represents the response of the resonator in absence of nonlinearities and can be used to determine the frequency shift Δf of the response at high driving power to the resonance frequency of the membrane at low driving powers (f_0). The resonance frequency of 40.41 MHz at low driving power is determined from the linear response at a modulation of -22 dBm, which is shown in purple. To fit the LHO model to the nonlinear data, the regions above and below the resonance frequency are determined manually, along with the initial guess for the resonance frequency. The procedure is shown in the inset of Figure 4.4 a for the response at 4 dBm, where the data used for the fit is represented in blue. In the fitting process, the amplitude of the LHO model is fixed, while the resonance frequency and quality factor are fitted. The frequency shift Δf is defined as the difference of the fitted resonance frequency to the resonance frequency at low driving power f_0.

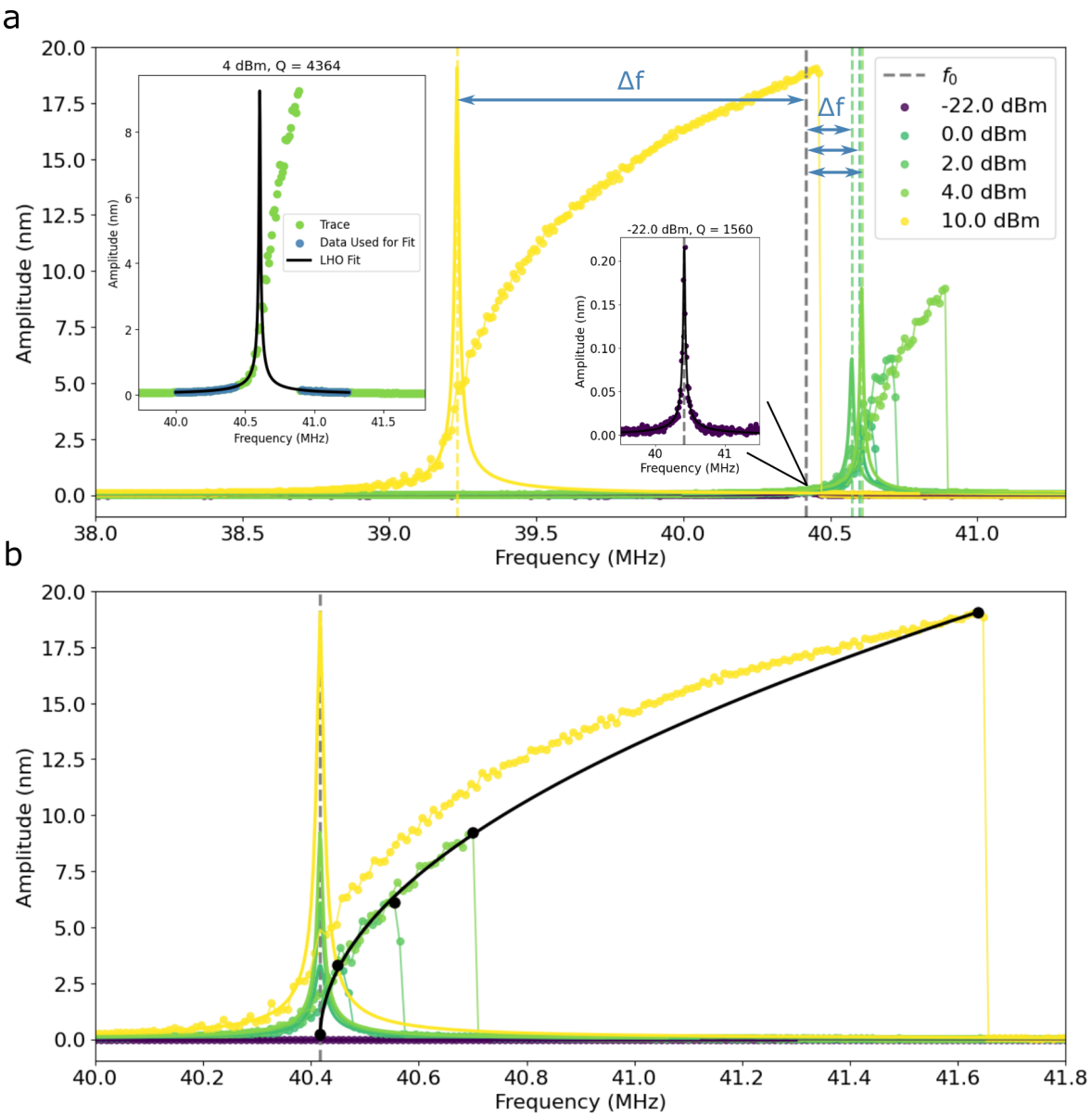

Figure 4.4: (a) Power-dependence measurement of Drum 16 at driving powers from -22 dBm to 10 dBm. To correct for the temperature-induced frequency shift, a LHO model is fitted to the response in the linear regime for amplitudes well below 1 nm (see inset). For each driving power, the frequency shift Δf is determined by calculating the difference between the resonance frequency from the LHO fit (indicated by colored dashed vertical lines) to the resonance frequency f_0 of the resonance at low driving power (-22 dBm, indicated by the vertical grey dashed line). The inset for -22 dBm shows the fit determining f_0. (b) Fit of the backbone curve (Equation 3.9) to the maximum amplitudes of each driving power after correction for temperature fluctuations. The extracted value for the Duffing coefficient from the fit is β = 14.5$\pm$0.2×10^{30} $Nm^{-3}kg^{-1}$.

After correction for the temperature fluctuations, the curves are plotted in Figure 4.4 b to fit the backbone curve and extract the normalized Duffing coefficient. In the graph, the maximum amplitudes for each driving power are highlighted by black dots, through which the backbone equation from Equation 3.9 is fitted. A good agreement of the fitted backbone curve and the maximum amplitudes is observed, indicating a successful temperature correction. The fitting procedure yields a mass-normalized Duffing coefficient of β = 14.5$\pm$0.2×10^{30} $Nm^{-3}kg^{-1}$, with the uncertainty extracted from the fit.

After extracting β from the backbone of the power-dependence measurement, it is possible to verify the agreement between the experimental data and the Duffing coefficient. This is achieved by plotting the experimental data together with the solutions of the steady-state amplitude based on Equation 2.18. For each driving power, the steady-state amplitude equation requires the resonance frequency $\omega_0 = 2\pi f_0$, the quality factor Q, the fitted Duffing coefficient β and the driving force per effective mass as F_ω/m_{eff}. The values for Q and F_ω/m_{eff} are calculated together with the resonance frequency in the step for the correction of temperature fluctuations in the same manually defined frequency regions. Q is calculated together with the resonance frequency and F_ω/m_{eff} in a separate fit of a LHO model with F_ω/m_{eff} in the numerator (Equation 2.9).

With these values as the input parameters for the steady-state amplitude response function, the experimental data is plotted together with the stable and unstable solution branches in Figure 4.5. The upper and lower stable solutions are plotted as solid lines, whereas a dashed line indicates the unstable solution. Figure 4.5 a-e show the data corresponding to the individual driving powers, while an overlay of all data and fits is presented in Figure 4.5 f.

The plotted steady-state amplitude response curves are in good agreement with the experimental data for power modulation values of -22 dBm up to 4 dBm (Figure 4.5a-d). The amplitude and curvature of the steady-state solution strongly resemble the experimental findings. However, it is important to emphasize the increase in quality factor from 1560 at -22 dBm to 4364 at 4 dBm. Generally, the quality factor of a resonator transitioning from the linear to the nonlinear regime is not expected to increase with increasing driving powers. With higher amplitudes, energy losses arising from nonlinear damping are expected to increase, thus leading to a broadened resonance and reduced quality factor [26, 31].

In contrast to the data of lower modulation powers, the agreement between the calculated amplitude response and the data for 10 dBm is reduced (Figure 4.5e). For frequencies around the resonance frequency, the measured amplitude increases more sharply than the calculated response, showing limited agreement. At amplitudes approaching the maximum, the calculated and measured response align more closely, showing similar curvatures. Most notably, the amplitude of the steady-state response does not match the value of the experimental data. In general, a reduced amplitude can originate from a lower quality factor. However, the quality factor was extracted from the LHO fit to the data performed for the temperature correction, which matches the experimentally determined amplitude in Figure 4.4 a and b.

The higher amplitude of the measured response for 10 dBm in comparison to the calculation using Equation 2.18 is unexpected, particularly regarding effects of nonlinear damping. If a resonator is subject to nonlinear damping, its vibrational amplitude is typically reduced in comparison to an undamped vibration, as presented in Figure 2.1 b. Since nonlinear damping was neglected in this thesis, the calculated amplitude would be expected to exceed the measured amplitude if nonlinear damping is present.

Brownian Motion Measurement

To be able to compute the Young's modulus from the mass normalized Duffing coefficient β, it is essential to convert it to the non-normalized form k_3. This can be achieved via Equation 2.16, requiring the effective mass to be known. The effective mass of the fundamental mode can be obtained with the measurement of the Brownian motion of the drum. By using the spectrum analyzer, the PSD of the drum's thermal motion is recorded together with the dark current noise of the photodetector. The PSD is measured at a bandwidth of 3kHz, a sweep time of 0.5 s and 20 averages. During the measurement, the blue laser is turned off. After subtracting the noise of the photodetector and a constant white noise signal, the pure PSD of the drum's thermal motion is obtained. By using the transduction factor obtained from the amplitude calibration, the effective mass can be extracted by fitting Equation 3.12 to the measured data. Before fitting the effective mass, initial guesses for the quality factor and resonance frequency are obtained by fitting a LHO model to the Brownian motion PSD. In Figure 4.6, the fit of Equation 3.12 to the measured PSD is shown. From the fit, an effective mass of m_{eff} = $11.5 \pm 0.7 \times 10^{-17}$ kg is obtained.

The extracted effective mass can be compared to that of an ideal circular drum made of monolayer MoS_2 without membrane slack, defects, or contamination. To calculate the mass for an ideal drum

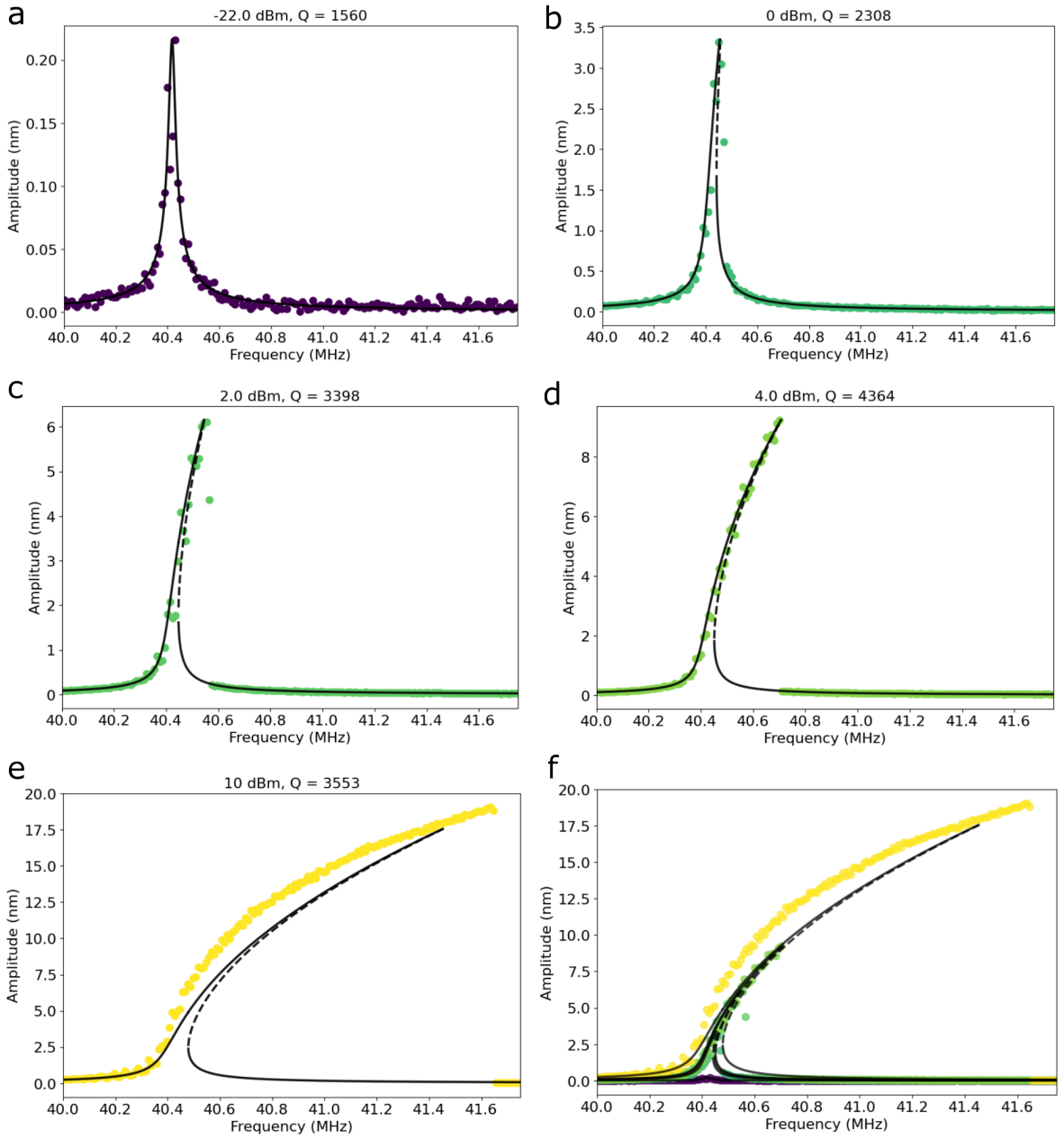

Figure 4.5: (a-e) Overlay of the measured and calculated steady state response of the oscillating membrane for increasing driving powers from -22 to 10 dBm. The colored data points correspond to the experimental data, and the black line indicates the steady-state solutions obtained from Equation 2.18. The stable solutions are represented by solid lines, while dashed lines represent the unstable solution. For each driving power, the quality factors extracted from the linear response are shown in the title of the plots. (f) Combined plot showing the experimental data and steady-state solutions for the driving powers of (a-e).

of 5 µm diameter, the bulk mass density of 5060 kgm^{-3} for MoS_2 is multiplied with the volume of the membrane for a thickness of 6.5 Å [61, 63]. The resulting ideal mass of 1.74×10^{-17} kg is a factor of 6.6 lower than the mass extracted from the fitting process. This discrepancy could be attributed to contaminants introduced during sample fabrication, transfer, and analysis, including moisture, dust, and other residues. Thus, the higher extracted mass is reasonable and does not necessarily indicate a large systematic error. Additionally, membrane slack in real drums leads to a slightly higher effective mass compared to an ideal, perfectly tensioned membrane. The discrepancy between measured and

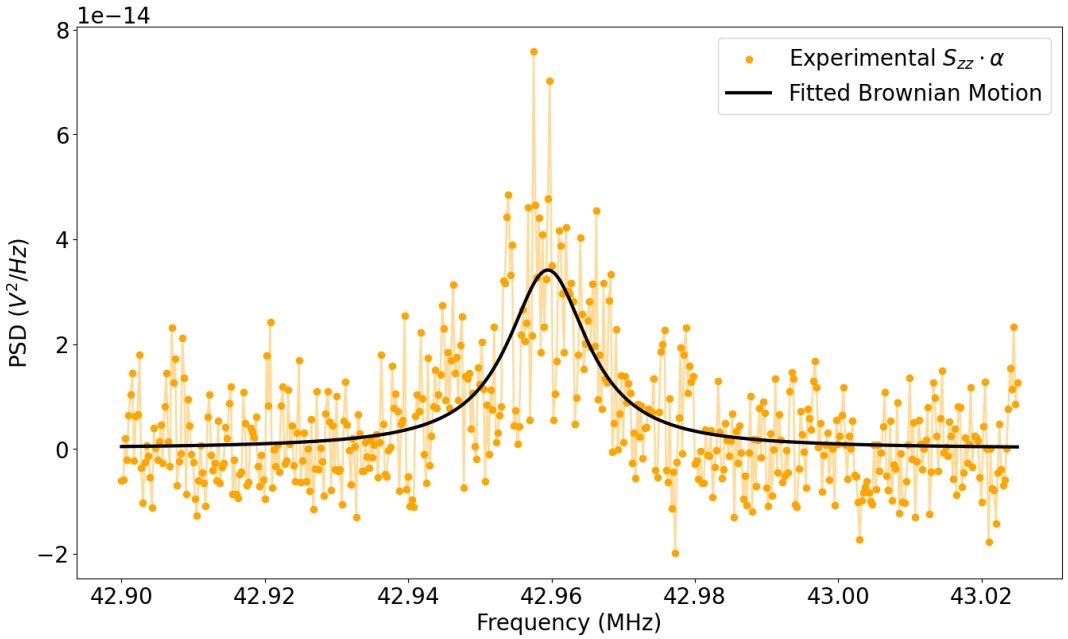

Figure 4.6: Measured power spectral density of Drum 16 after subtraction of a flat noise background, together with the corresponding fit to determine the effective mass of the membrane. The power spectral density is measured with a bandwidth of 3 kHz, a sweep time of 0.5 s and 20 averages at an input impedance of 50 Ω. The value obtained for the effective mass is m_{eff} = 11.5±0.7×10^{-17} kg.

expected values is discussed in more detail in subsection 4.1.3.

4.1.2. Calculation of the Young's Modulus

After obtaining the effective drum mass, it is possible to calculate the non-normalized spring constant k_3 and the Young's modulus via Equation 3.1. By rearranging Equation 2.16, k_3 is calculated as $k_3 = \beta m_{eff,fit}$ and has a value of 1.67±0.33×10^{15} Nm^{-3}. To compute the modulus for Drum 16, the value for k_3 is used together with a radius of 2.5 µm, monolayer thickness of 0.65 Å and a Poisson ratio of 0.25 [61, 64]. The obtained value for the Young's modulus using the values extracted with the presented method is E = 5157 ± 980 GPa. The error was determined by propagating the errors from the transduction factor, effective mass and Duffing coefficient.

This modulus value is significantly higher than the expected literature values, which range from 140 to 430 GPa [22]. To provide a more comprehensive overview, the moduli of three additional drums are shown in Figure 4.7, obtained using the same all-optical procedure. As evident from the figure, the moduli of all drums are significantly higher than the literature values (grey horizontal band), with the modulus of Drum 5 being the closest at 663±158 GPa. Furthermore, the figure shows calculated Young's moduli of the analyzed drums when the effective mass of an ideal drum $m_{eff,calc}$ is used to calculate k_3. These moduli are in better agreement with the literature data and range from 87±20 GPa to 779±140 GPa. Although the values for Drum 12 and Drum 16 are close to or within the range of literature values, a general deviation remains.

To calculate the Young's moduli of the other examined drums, the corresponding transduction factor, Duffing coefficient and fitted effective mass were determined with the same approach as for Drum 16. The values for each drum are summarized in Table 4.1, allowing comparison among the drums and to values obtained from other works.

The normalized Duffing coefficient is expected to differ slightly due to sample-dependent variations in pre-tension, contamination and defects. The Duffing coefficient governs the amplitude-dependent membrane stiffening, which increases the restoring force (Equation 2.19). The fabrication of nanomechanical membrane resonators inherently results in membranes with varying pre-tension, defect den-

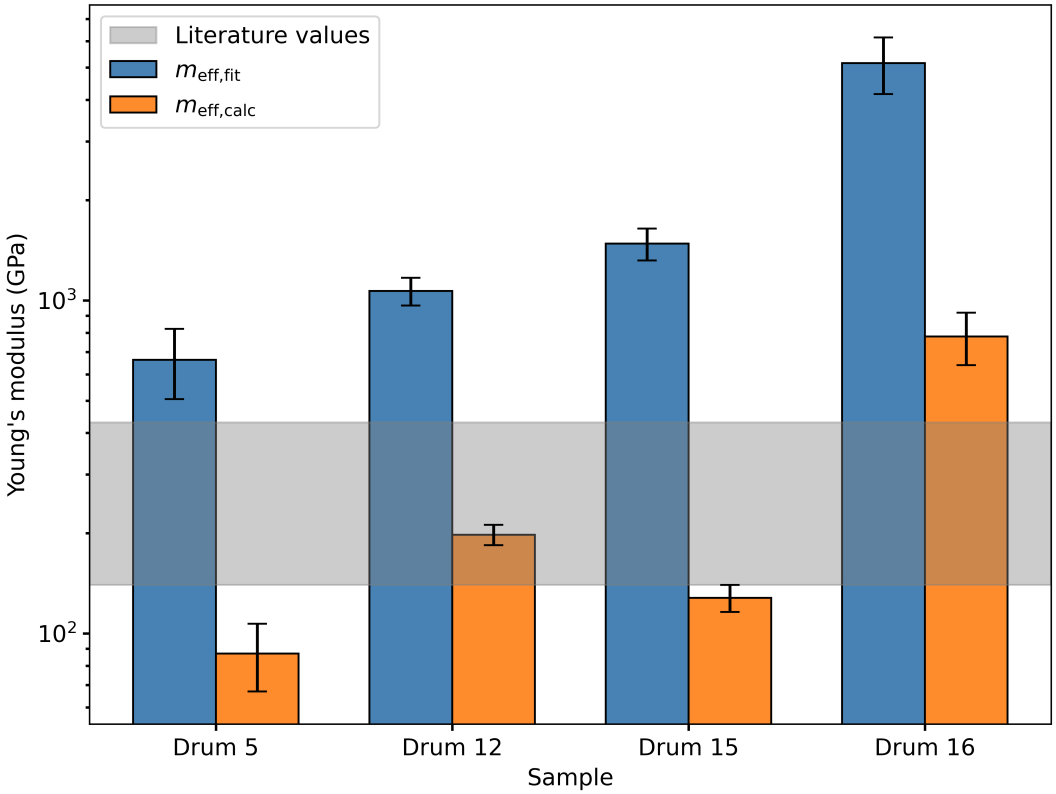

Figure 4.7: Bar chart representing the experimentally obtained Young's moduli of the studied membrane resonators. Blue bars indicate Young's moduli calculated from the fitted effective mass from the Brownian motion. Orange bars represent the moduli when calculated with an effective mass of an ideal, perfectly spherical drum. The range of Young's moduli described in literature is indicated by a grey horizontal band [22].

sity, and contamination levels [65, 66]. Davidovikj *et al.* demonstrated that non-uniform pre-strain distributions modify the mode shape, thereby altering the amplitude dependent stiffening behavior [47]. Furthermore, crystal lattice defects or additional point masses from contamination can further influence the mode shape and result in variations in the cubic stiffness between membranes. As shown in Table 4.1, the extracted values for β are comparable for Drums 5, 12, and 15, whereas the value for Drum 16 deviates.

Comparing the transduction factors to the value reported by Dolleman *et al.*, a clear difference between MoS_2 and graphene is evident [24]. The transduction factor of MoS_2 is approximately three orders of magnitude higher than for graphene. This can be attributed to the higher reflectivity and stronger optical absorption of MoS_2, compared to graphene's broadband but weaker absorption [68]. Additionally, the higher responsivity values of MoS_2 in Figure 3.3 support this correlation. Moreover, the obtained values are consistent with those of Davidovikj *et al.* [22] obtained by interferometric readout and amplitude calibration via Brownian motion.

4.1.3. Discrepancy Between Results and Literature

As evident from Figure 4.7, the Young's moduli calculated from the fitted data show a clear discrepancy with literature values across all studied drums. This discrepancy persists even when the effective mass of an ideal drum is used to calculate the modulus instead of the fitted mass from the Brownian motion. The analysis and identification of the cause for the discrepancy is further hindered by a limited amount of studies reporting values for the Duffing coefficient and transduction factor obtained via optical readout and transduction methods. While it is difficult to attribute the discrepancy to a single measurement

Table 4.1: Comparison of experimentally determined properties of the examined monolayer MoS_2 resonators analyzed with the developed method. The measured transduction factor, normalized Duffing coefficient and effective mass are given together with values extracted from literature for similar experimental techniques. [1]Calculated assuming a perfectly spherical drum of radius 4 and 5 µm, a bulk mass density of 5060 kgm^{-3} and monolayer thickness of 6.5 Å [61, 63].

Sample	Drum Diameter (µm)	Transduction Factor α ($\times 10^{12}$ V^2/m^2)	Normalized Duffing Coefficient β ($\times 10^{30}$ $Nm^{-3}kg^{-1}$)	Effective Mass $m_{eff,fit}$ ($\times 10^{-17}$ kg)	E using $m_{eff,fit}$ (GPa)	E using $m_{eff,calc}$ (GPa)
Drum 5	4	0.51±0.09	3.94±0.4	8.51±0.3	663±158	87±20
Drum 12	5	5.47±0.22	3.69±0.2	9.35±0.5	1067±102	198±14
Drum 15	5	1.23±0.09	2.38±0.1	20.1±0.9	1480±163	128±12
Drum 16	5	1.43±0.06	14.5±0.2	11.5±0.7	5157±996	779±140
MoS_2 [22]	4	2.56	—	—	—	315±23
Ideal MoS_2	4/5	—	—	1.11/1.74[1]	—	140-430 [22]
Graphene (5 nm) [22]	5	—	8.79	—	—	—
Graphene [24]	5	0.00774	—	—	—	—
Graphene [67]	5	—	—	5.0-9.6	—	494

parameter, potential sources of error include the mode shape of the resonating membrane, the fitted effective mass, the amplitude calibration step and the extraction of the Duffing coefficient.

Mode Shape

Firstly, the dependence of the presented all-optical procedure on the mode shape of the drum is highlighted. All equations that were used to derive the Young's moduli rely on the assumption that the fundamental mode with the corresponding mode shape is measured. The presence of contamination, lattice defects or non-uniform pre-strain throughout the membrane can cause deviation of the vibrational mode from the fundamental mode shape [47]. The applied formulas for the modulus calculation in this thesis are derived for axisymmetric vibrational modes of the membrane and are invalid for asymmetric modes [22]. Whereas the fundamental mode is generally axisymmetric, contamination, imperfections or non-uniform pre-strain could result in an asymmetric vibrational mode, causing inaccurate results. Furthermore, non-uniformity of the membrane could lead to mode-coupling, further altering the vibrational mode shape [26].

Effective Mass

Secondly, the effective mass of the membrane is a critical parameter in the calculation, because it directly influences the value of the nonlinear spring constant. Lattice defects or additional mass from contamination can lead to significant changes of the effective mass. To assess the quality of the analyzed samples, AFM imaging is performed on both monolayer and multilayer membranes. Two drums measured using the proposed all-optical method are analyzed (Drum 15 and 16) alongside previously unstudied drums. The AFM images of Drum 15 and 16 are presented in Figure 4.8a-b, and clearly show impurities and defects on the monolayer surface.

Drum 15 shows strong contamination by added particles on the membrane surface in the vicinity of the membrane edge. With respect to the monolayer membrane, these particles have a height of approximately 35 nm, and could significantly increase the mass of the membrane and affect its mode shape. The AFM images also reveal side-wall adhesion, indicated by the steep slope of the membrane around

its circumference. Additionally, Drum 16 shows contamination in the vicinity of the membrane edge and a major lattice defect. Indicated by the abrupt decrease in height close to the membrane center, the membrane seems perforated. A perforation in the membrane is expected to drastically affect the mode shape and strain profile of the membrane. Further measurements on monolayer (Drum A2) and multilayer (Drum A6) drums are performed, which were not studied with nonlinear dynamic characterization. Both drums are presented in Figure 4.8c-d, also highlighting contamination and non-uniformity of the membranes. While Drum A2 seems to have less contamination, Drum A6 shows localized impurities of ~45 nm and wrinkles close to the membrane edge.

Despite the presence of impurities, the effective mass of the MoS_2 membranes is comparable to that of graphene membranes studied by Liu *et al.* with the same radius, which range from 5.0–9.6 $\times 10^{-17}$ kg [67]. Given that graphene has a slightly lower mass than MoS_2, the mass values obtained for the resonators in this thesis appear reasonable.

Laser Position Sensitivity in Transduction and Nonlinear Stiffness

Finally, the strong dependence of the transduction factor and nonlinear spring constant on the laser position is emphasized. From the amplitude calibration step, the transduction factor is extracted, which is a crucial input parameter for the fit of the backbone curve to obtain the Duffing coefficient and the extraction of the effective mass. If the readout laser is not directly focussed on the drum center, the interferometric readout captures a reduced vibrational amplitude with respect to the central oscillation, leading to an inaccurate transduction factor. This could potentially influence the calculated Young's modulus, contributing to the observed discrepancy.

In addition to the transduction factor, the nonlinear stiffness is highly sensitive to the measurement position. If the readout laser is not focused on the center of the drum, a reduced vibrational amplitude is recorded, since the highest oscillation of the fundamental mode occurs in the membrane center. When assuming that the actuation force and resonance frequency stay unaffected, the Duffing coefficient would increase. This could occir for cases where the blue and red laser are not perfectly aligned, or both lasers are focused on an off-center position of the membrane. With the requirement of manual adjustment of the laser position on the drum due to the influence of the beam splitter (subsection 3.4.2), this inaccuracy is increased. The increased Duffing coefficient could explain the increased values of the Young's moduli, due to the direct proportionality of the modulus and the Duffing coefficient.

Additional Error Sources

An additional source of error could lie in the experimental procedure for the measurement of the Brownian motion. The fitted effective mass was obtained by measuring the thermal noise of the drum without irradiation of the blue laser. This changes the temperature of the drum and thus its resonance frequency, from 40.41 MHz under irradiation with the blue and red laser to 42.96 MHz during the Brownian motion measurement. Despite the better agreement of Young's moduli using the calculated instead of the fitted effective mass, is it not possible to regard the fitted mass as the only source of error. Although the fitting procedure is consistent in itself and experimental data and steady-state solution align reasonably well, it is not possible to purely assign the source for the discrepancy to the mass fitting procedure. As discussed, the transduction factor and Duffing coefficient are highly dependent on the laser position on the drum and could equally contribute to the discrepancy in the results.

Another interesting observation is the significant change in quality factor that was observed from fitting the LHO model to the power-dependence measurement. Generally, such an increase is not expected, as damping effects typically increase with increasing driving amplitude [26, 31]. However, the resonators in this thesis showed quality factors above 1000, which is higher than commonly reported values [53–56]. While the high quality factors could be related to dissipation dilution, an explanation for the quality factor increase can not be given at this point.

Finally, it is important to note that the different sources of error are not independent but highly interconnected. In particular, membrane contamination or defects simultaneously affect the mode shape, effective mass, and nonlinear stiffness. The fundamental assumption underlying the equations in this thesis is the symmetry of the fundamental mode. If defects or additional mass alter the mode shape, the

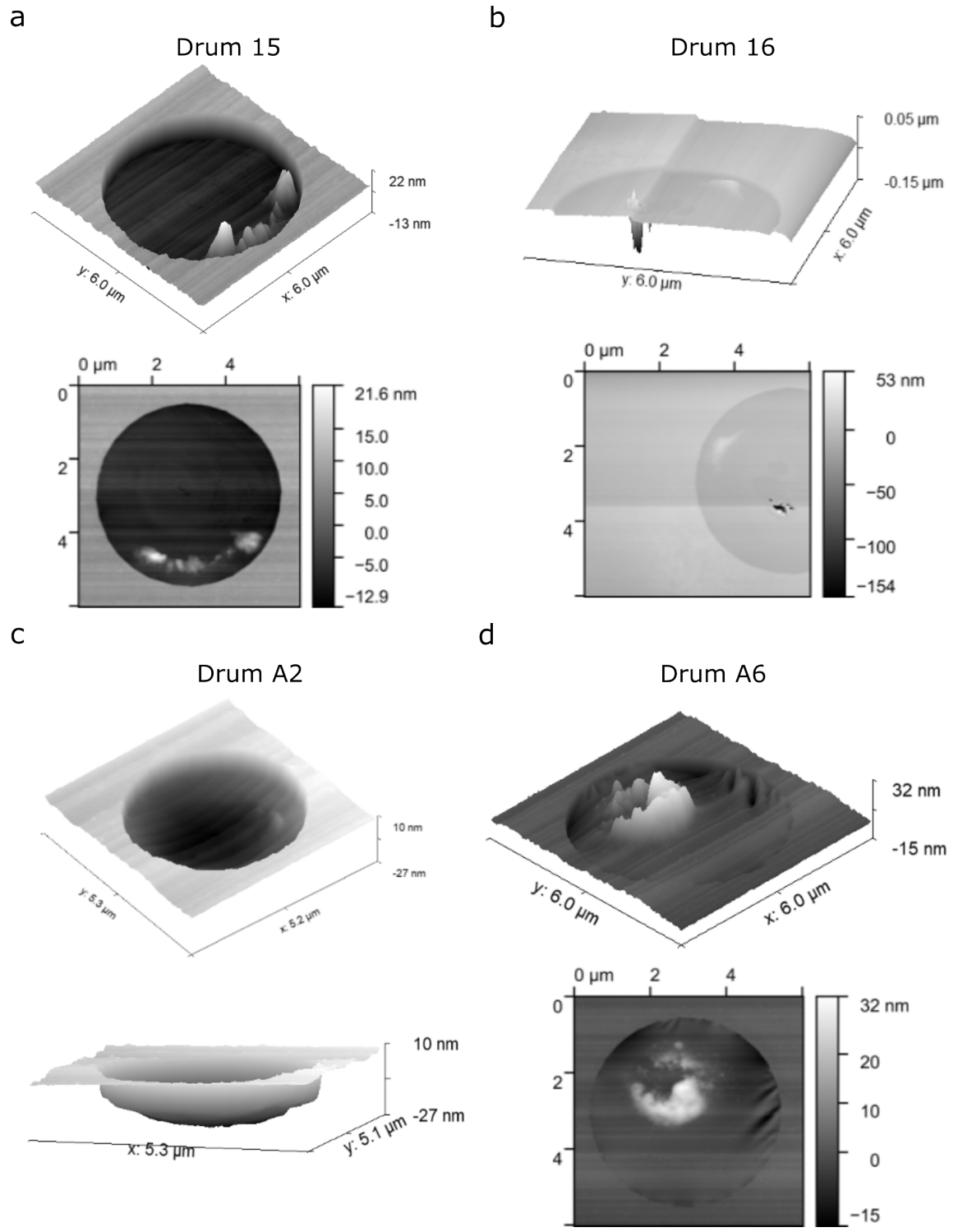

Figure 4.8: Scanning mode AFM images of four suspended MoS_2 membranes to reveal the topography and quality of the membranes. (a-b) Topography maps of monolayer membranes of Drum 15 and 16, showing sample contamination close to the cavity edge and membrane perforation (Drum 16). Topography of additional (c) monolayer and (d) multilayer membranes, which were not studied with nonlinear dynamic characterization. The membrane in (c) shows comparably low contamination, while the multilayer in (d) shows strong contamination of the membrane with a height of ~45 nm with respect to the membrane. Additionally, wrinkles are present in the vicinity of the membrane edge.

equations become less accurate. Moreover, the mode shape determines the measured amplitude during the calibration step and backbone fitting process, directly influencing the extracted Young's modulus via the transduction factor and Duffing coefficient.

5

Conclusion and Outlook

In the scope of this thesis, a novel all-optical approach for measuring the Young's modulus of two-dimensional materials was developed and successfully tested on monolayer membrane resonators of MoS_2. By replicating nonlinear dynamic characterization from Davidovikj *et al.* and combining it with optical amplitude calibration from Dolleman *et al.*, an all-optical analysis method is achieved. From a set of three consecutive measurements, it is possible to extract the Young's modulus without preliminary assumptions about the resonator. By eliminating the need for physical contact, this method overcomes limitations of atomic force microscopy (AFM) nanoindentation, such as high stress concentrations, tip-sample interactions (adhesion, capillary forces), and viscoelastic effects. Unlike the static deflection method in AFM, the presented approach enables the characterization of the dynamic mechanical properties of 2D materials through their nonlinear vibrational behavior.

Although values for the Young's moduli of all drums are extracted, these values exceed the range of literature values. On the other hand, calculation of the Young's modulus with the effective mass of an ideal drum yields results slightly below literature values. Given the similarity of the obtained mass values to those of Liu *et al.*, the mass values obtained in this thesis appear reasonable [67]. One of the key factors influencing the results is the strong sensitivity of the transduction factor and nonlinear stiffness to laser positioning. Moreover, surface morphology imaging revealed significant contamination and lattice defects, which could explain deviations in the extracted Young's modulus. Since membrane contamination and imperfections impact all key parameters, including the mode shape, effective mass, and nonlinear stiffness, it is challenging to identify a single source of error. Given the inherent challenges associated with measuring atomically thin monolayer membranes, it is noteworthy that this method yielded results for the modulus, despite the need for further improvements.

While pristine membranes without deliberately introduced defects were studied throughout this thesis, analysis of defective membranes is feasible, given that the mode shape does not drastically deviate from the fundamental mode. This would allow analysis of the Young's modulus of defective graphene membranes to evaluate a potential modulus increase at low defect concentrations, as presented by López-Polín *et al.* [19]. Furthermore, this technique could be expanded to other 2D materials if their mechanical, thermal and optical properties allow analysis with this all-optical, nonlinear dynamic approach.

Despite deviation from the experimentally determined Young's moduli to literature values, the presented method successfully combines actuation, amplitude calibration and mass determination relying purely on optical methods. Thus, this method could function as a promising, contactless alternative to AFM Nanoindentation to unravel the connection between point defects and Young's modulus in 2D material monolayers.

5.1. Final Recommendations

Given the high relevance of 2D materials for current and future industrial applications, further experimental research is required to evaluate and improve the method presented in this thesis. Below, a list of potential improvements and recommendations is given. By adapting the experimental setup accordingly, the developed method could pave the way towards a deeper understanding of the relation between Young's modulus and defect concentration.

- To detect a signal for the harmonics up to the third order, the monolayer resonators in this thesis required very high actuation power as opposed to multilayer membranes. This increases the chance of influencing the membrane, increasing membrane temperature and introducing defects. A possible way to reduce the invasiveness of the method is by changing the readout laser and adapting the cavity depth accordingly to obtain the highest possible responsivity. Furthermore, this increases the sensitivity and stability of the method as well as the measurement yield.
- The invasiveness could further be reduced by applying a different actuation method, such as a piezoelectric actuator. This reduces changes in membrane temperature and possible changes of the membrane. Furthermore, the necessity of aligning the actuation and readout laser is avoided, which simplifies the experimentation and increases efficiency.
- With an improved measurement setup, repeated measurements on the same drum would provide insight into the accuracy and reproducibility of the method by reducing statistical uncertainty.
- To validate the method, the analysis of multilayer membranes is feasible. This would reduce the effect of contamination on the effective mass, providing more accurate results.

References

1. Iannaccone, G., Bonaccorso, F., Colombo, L. & Fiori, G. Quantum engineering of transistors based on 2D materials heterostructures. en. *Nature Nanotechnology* **13,** 183–191 (2018).
2. Tatullo, M. *et al.* Phosphorene Is the New Graphene in Biomedical Applications. *Materials* **12** (2019).
3. Lemme, M. C. *et al.* Nanoelectromechanical Sensors Based on Suspended 2D Materials. en. *Research* **2020,** 2020/8748602 (2020).
4. Khan, K. *et al.* Going green with batteries and supercapacitor: Two dimensional materials and their nanocomposites based energy storage applications. *Progress in Solid State Chemistry* **58,** 100254 (2020).
5. Glavin, N. R. *et al.* Emerging Applications of Elemental 2D Materials. en. *Advanced Materials* **32,** 1904302 (2020).
6. Zhang, Z. *et al.* Rosin-enabled ultraclean and damage-free transfer of graphene for large-area flexible organic light-emitting diodes. en. *Nature Communications* **8,** 14560 (2017).
7. Lee, Y. H. *et al.* Flexible high-performance graphene hybrid photodetectors functionalized with gold nanostars and perovskites. en. *NPG Asia Materials* **12,** 1–12 (2020).
8. Dong, M. *et al.* Multifunctional epoxy nanocomposites reinforced by two-dimensional materials: A review. en. *Carbon* **185,** 57–81 (2021).
9. Hou, Y. *et al.* Tuning instability in suspended monolayer 2D materials. en. *Nature Communications* **15,** 4033 (2024).
10. Mounet, N. *et al.* Two-dimensional materials from high-throughput computational exfoliation of experimentally known compounds. en. *Nature Nanotechnology* **13,** 246–252 (2018).
11. Falin, A. *et al.* Mechanical properties of atomically thin boron nitride and the role of interlayer interactions. en. *Nature Communications* **8,** 15815 (2017).
12. Wang, T. *et al.* Xenes as an Emerging 2D Monoelemental Family: Fundamental Electrochemistry and Energy Applications. en. *Advanced Functional Materials* **30,** 2002885 (2020).
13. Lee, C., Wei, X., Kysar, J. W. & Hone, J. Measurement of the Elastic Properties and Intrinsic Strength of Monolayer Graphene. en. *Science* **321,** 385–388 (2008).
14. Peng, Z., Chen, X., Fan, Y., Srolovitz, D. J. & Lei, D. Strain engineering of 2D semiconductors and graphene: from strain fields to band-structure tuning and photonic applications. en. *Light: Science & Applications* **9,** 190 (2020).
15. Georgakilas, V. *et al.* Functionalization of Graphene: Covalent and Non-Covalent Approaches, Derivatives and Applications. *Chemical Reviews* **112,** 6156–6214 (2012).
16. Cao, Q. *et al.* A Review of Current Development of Graphene Mechanics. en. *Crystals* **8,** 357 (2018).
17. Komsa, H.-P. & Krasheninnikov, A. V. in *Defects in Two-Dimensional Materials* (eds Addou, R. & Colombo, L.) 7–41 (Elsevier, 2022).
18. Zandiatashbar, A. *et al.* Effect of defects on the intrinsic strength and stiffness of graphene. en. *Nature Communications* **5,** 3186 (2014).
19. López-Polín, G. *et al.* Increasing the elastic modulus of graphene by controlled defect creation. en. *Nature Physics* **11,** 26–31 (2015).
20. Rosenhek-Goldian, I. & Cohen, S. R. Some considerations in nanoindentation measurement and analysis by atomic force microscopy. en. *Journal of Vacuum Science & Technology A* **41,** 062801 (2023).

21. Rao, Y. & Lu, N. Effects of adhesive and frictional contacts on the nanoindentation of two-dimensional material drumheads. en. *Journal of the Mechanics and Physics of Solids* **192,** 105828 (2024).
22. Davidovikj, D. *et al.* Nonlinear dynamic characterization of two-dimensional materials. en. *Nature Communications* **8,** 1253 (2017).
23. Chen, C. *et al.* Performance of monolayer graphene nanomechanical resonators with electrical readout. en. *Nature Nanotechnology* **4,** 861–867 (2009).
24. Dolleman, R. J., Davidovikj, D., Van Der Zant, H. S. J. & Steeneken, P. G. Amplitude calibration of 2D mechanical resonators by nonlinear optical transduction. en. *Applied Physics Letters* **111,** 253104 (2017).
25. Yu, J. *et al.* Designing the Bending Stiffness of 2D Material Heterostructures. en. *Advanced Materials* **33,** 2007269 (2021).
26. Schmid, S., Villanueva, L. G. & Roukes, M. L. *Fundamentals of Nanomechanical Resonators* en (Springer International Publishing, Cham, 2016).
27. Castellanos-Gomez, A., Singh, V., Van Der Zant, H. S. J. & Steele, G. A. Mechanics of freely-suspended ultrathin layered materials. en. *Annalen der Physik* **527,** 27–44 (2015).
28. Rao, S. S. *Mechanical Vibrations* 5th (Prentice Hall, Upper Saddle River, NJ, 2011).
29. Hauer, B., Doolin, C., Beach, K. & Davis, J. A general procedure for thermomechanical calibration of nano/micro-mechanical resonators. en. *Annals of Physics* **339,** 181–207 (2013).
30. Keşkekler, A. *Nonlinear coupling and dissipation in two-dimensional resonators* PhD thesis (Delft University of Technology, 2023).
31. Steeneken, P. G., Dolleman, R. J., Davidovikj, D., Alijani, F. & Van Der Zant, H. S. J. Dynamics of 2D material membranes. en. *2D Materials* **8,** 042001 (2021).
32. Lifshitz, R. & Cross, M. C. en. in *Reviews of Nonlinear Dynamics and Complexity* (ed Schuster, H. G.) 1st ed. (Wiley, 2008).
33. Novoselov, K. S. *et al.* Electric Field Effect in Atomically Thin Carbon Films. en. *Science* **306,** 666–669 (2004).
34. Mak, K. F., Lee, C., Hone, J., Shan, J. & Heinz, T. F. Atomically Thin MoS2: A New Direct-Gap Semiconductor. *Physical Review Letters* **105,** 136805 (2010).
35. Hong, J. *et al.* Exploring atomic defects in molybdenum disulphide monolayers. en. *Nature Communications* **6,** 1–8 (2015).
36. Ossila B.V. *Molybdenum Disulfide, MoS2: Theory, Structure & Applications* `https://www.ossila.com/pages/molybdenum-disulfide-mos2#ref1` (2024).
37. Bertolazzi, S., Brivio, J. & Kis, A. Stretching and breaking of ultrathin MoS2. eng. *ACS nano* **5,** 9703–9709 (2011).
38. Castellanos-Gomez, A. *et al.* Elastic Properties of Freely Suspended MoS2 Nanosheets. *Advanced Materials* **24,** 772–775 (2012).
39. Peng, Q. & De, S. Outstanding mechanical properties of monolayer MoS2 and its application in elastic energy storage. en. *Physical Chemistry Chemical Physics* **15,** 19427–19437 (2013).
40. Sahu, S. *et al.* Large-Area Mechanically-Exfoliated Two-Dimensional Materials on Arbitrary Substrates. en. *Advanced Materials Technologies* **8,** 2201993 (2023).
41. Velický, M. *et al.* Mechanism of Gold-Assisted Exfoliation of Centimeter-Sized Transition-Metal Dichalcogenide Monolayers. en. *ACS Nano* **12,** 10463–10472 (2018).
42. Heyl, M. *et al.* Low Temperature Heating of Silver-Mediated Exfoliation of MoS_2. en. *Advanced Materials Interfaces* **9,** 2200362 (2022).
43. Desbiolles, B. X. E., Furlan, G., Schwartzberg, A. M., Ashby, P. D. & Ziegler, D. Electrostatically actuated encased cantilevers. *Beilstein Journal of Nanotechnology* **9,** 1381–1389 (2018).
44. Dolleman, R. J. *et al.* Opto-thermally excited multimode parametric resonance in graphene membranes. en. *Scientific Reports* **8,** 9366 (2018).

45. Nair, R. R. *et al.* Fine Structure Constant Defines Visual Transparency of Graphene. en. *Science* **320,** 1308–1308 (2008).
46. Blake, P. *et al.* Making graphene visible. en. *Applied Physics Letters* **91,** 063124 (2007).
47. Davidovikj, D. *et al.* Visualizing the Motion of Graphene Nanodrums. en. *Nano Letters* **16,** 2768–2773 (2016).
48. Zhang, H. *et al.* Measuring the Refractive Index of Highly Crystalline Monolayer MoS2 with High Confidence. en. *Scientific Reports* **5,** 8440 (2015).
49. Houmes, M. *Magnetostriction in 2D material nanomechanical resonators* PhD thesis (Delft University of Technology, 2024).
50. Li, Z. *et al.* Finite Element-based Nonlinear Dynamic Optimization of Nanomechanical Resonators. *arXiv preprint.* arXiv: 2407.12600 (2024).
51. Lee, Y.-C., Chang, S.-W., Chen, S.-H., Chen, S.-L. & Chen, H.-L. Optical Inspection of 2D Materials: From Mechanical Exfoliation to Wafer-Scale Growth and Beyond. *Advanced Science* **9,** 2102128 (2021).
52. Li, Z. *et al.* Strain engineering of nonlinear nanoresonators from hardening to softening. en. *Communications Physics* **7,** 53 (2024).
53. Zhang, P. *et al.* Unveiling the tradeoff between device scale and surface nonidealities for an optimized quality factor at room temperature in 2D MoS2 nanomechanical resonators. en. *Microsystems & Nanoengineering* **10,** 140 (2024).
54. Zheng, X.-Q., Lee, J. & Feng, P. X.-L. Hexagonal boron nitride nanomechanical resonators with spatially visualized motion. en. *Microsystems & Nanoengineering* **3,** 17038 (2017).
55. Castellanos-Gomez, A. *et al.* Single-Layer MoS_2 Mechanical Resonators. en. *Advanced Materials* **25,** 6719–6723 (2013).
56. Lee, J., Wang, Z., He, K., Shan, J. & Feng, P. X.-L. Air damping of atomically thin MoS2 nanomechanical resonators. en. *Applied Physics Letters* **105,** 023104 (2014).
57. Beccari, A. *et al.* Strained crystalline nanomechanical resonators with quality factors above 10 billion. en. *Nature Physics* **18,** 436–441 (2022).
58. Hälg, D. *et al.* Membrane-based scanning force microscopy. en. *Physical Review Applied* **15,** L021001 (2021).
59. Fedorov, S. A. *et al.* Generalized dissipation dilution in strained mechanical resonators. en. *Physical Review B* **99,** 054107 (2019).
60. Wopereis, M. P. F. *et al.* Tuning dissipation dilution in 2D material resonators by MEMS-induced tension. en. *Journal of Applied Physics* **136,** 014302 (2024).
61. Zhao, Y. & Ouyang, G. Thickness-dependent photoelectric properties of MoS2/Si heterostructure solar cells. en. *Scientific Reports* **9,** 17381 (2019).
62. Šiškins, M. *et al.* Magnetic and electronic phase transitions probed by nanomechanical resonators. en. *Nature Communications* **11,** 2698 (2020).
63. *CRC Handbook of chemistry and physics* 102nd edition 2021-2022. eng (ed Rumble, J. R.) (CRC Press, Boca Raton London New York, 2021).
64. Liu, K. *et al.* Elastic Properties of Chemical-Vapor-Deposited monolayer MoS_2, WS_2, and their bilayer heterostructures. en. *Nano Letters* **14,** 5097–5103 (2014).
65. Ferrari, P. F., Kim, S. & Van Der Zande, A. M. Nanoelectromechanical systems from two-dimensional materials. en. *Applied Physics Reviews* **10,** 031302 (2023).
66. Sarafraz, A. *et al.* Quantifying stress distribution in ultra-large graphene drums through mode shape imaging. en. *npj 2D Materials and Applications* **8,** 45 (2024).
67. Liu, H. *et al.* Tuning heat transport in graphene by tension. en. *Physical Review B* **108,** L081401 (2023).
68. Li, Q., Lu, J., Gupta, P. & Qiu, M. Engineering Optical Absorption in Graphene and Other 2D Materials: Advances and Applications. en. *Advanced Optical Materials* **7,** 1900595 (2019).

Acknowledgements

These last pages of my thesis are dedicated to the people who helped and supported me in this final stage of my master. Without you, the journey to this thesis would have surely been longer and a lot more difficult.

Álvaro, you deserve the first words in this chapter. I remember my first nanomechanics meeting on the day I started my thesis. Maurits was presenting some very intricate math on plate theory and magnetostriction. Despite him using Einstein notation, one equation filled a whole page. I stared at the screen and thought: ”What have I done to myself?”.

But, from day to day, nonlinear dynamics and membrane theory started to make more and more sense, and I eventually ended up enjoying every day of my thesis (except maybe the last few days of writing). For that, you deserve all the credit. I don’t know how often I knocked at your office door, interrupting you in what you were doing. It must be somewhere close to 50x (or more?). However, I always felt very welcomed, and you answered all my questions in a very intuitive and understandable way.

I really benefited from your structured approach to solving problems and explaining something, I’m sure this will help me for the rest of my career. But, you are not only a great researcher, but have a great personality as well. We have spent countless hours together in the past months, (mis-) aligning lasers, measuring resonances, cursing the missing harmonics and bursting drums while still having fun. I do not think many master students have enjoyed spending time with their daily supervisor as much as I did. Thank you for everything. I am proud calling you my amigo.

Peter, without your guidance, expertise, and creativity in explaining potential errors for a mismatch in the results, this journey would have been much more difficult. When I slowly began understanding the vast and complicated world of nanomechanics in 2D materials, you provided me and Álvaro with countless ideas on what to measure, how to measure, what to analyze and how to interpret our results. Your enormous expertise on mechanics and electronics surely made our life easier. I thank you for your constant support in the meetings or via email. Although I had lots of questions and wrote emails even on the weekends and late at night, you always took time to answer me, give valuable feedback and explain your ideas. I very much appreciate this and can say that I felt a bit like a PhD student.

Herre, thank you for your constant interest in my research and giving ideas to explain our results. I appreciate your attention to words and phrasing when it comes to presenting and discussing results. Besides that, I enjoyed our conversations during lunch or while having a coffee, you are certainly part of the reason for the close community in this department. Too bad we didn’t manage to play tennis with Álvaro and Peter!

The samples studied in this thesis were fabriacted by Adeel Bukhari from the Group of Otakar Franke at the Czech Academy of Sciences. Thank you for providing so many samples throughout the last months. I am aware of the time and effort it takes to fabricate and analyze them and I very much appreciate your efforts.

Next, there are all the other friendly, welcoming and amazing people in the department. Maurits, Riccardo, Riccardo, Matteo, Cosimo, Raúl, Loic, Giannis, Linde, Ritesh, Merel, Boris and everyone else. From bouldering to beers, padel, or watching a series, I am glad to have spent time outside the faculty with you. I feel much like I am part of the whole group and I am happy I got to know all of you. Thank you for making the QN Department so special. I am certain that this is one of the nicest research groups in the whole world.

Finally, I want to thank my friends and family for supporting me throughout this journey. By giving mental support or checking my thesis, all of you helped me reach this day. To those friends who still need to finish their thesis, stay strong, I believe in you, and I am always there for support.

Now, it is time to hand in my report, and I thank all of you from the bottom of my heart. Stay the way you are.

A

Measurements and Results of Additional Drums

Drum 5

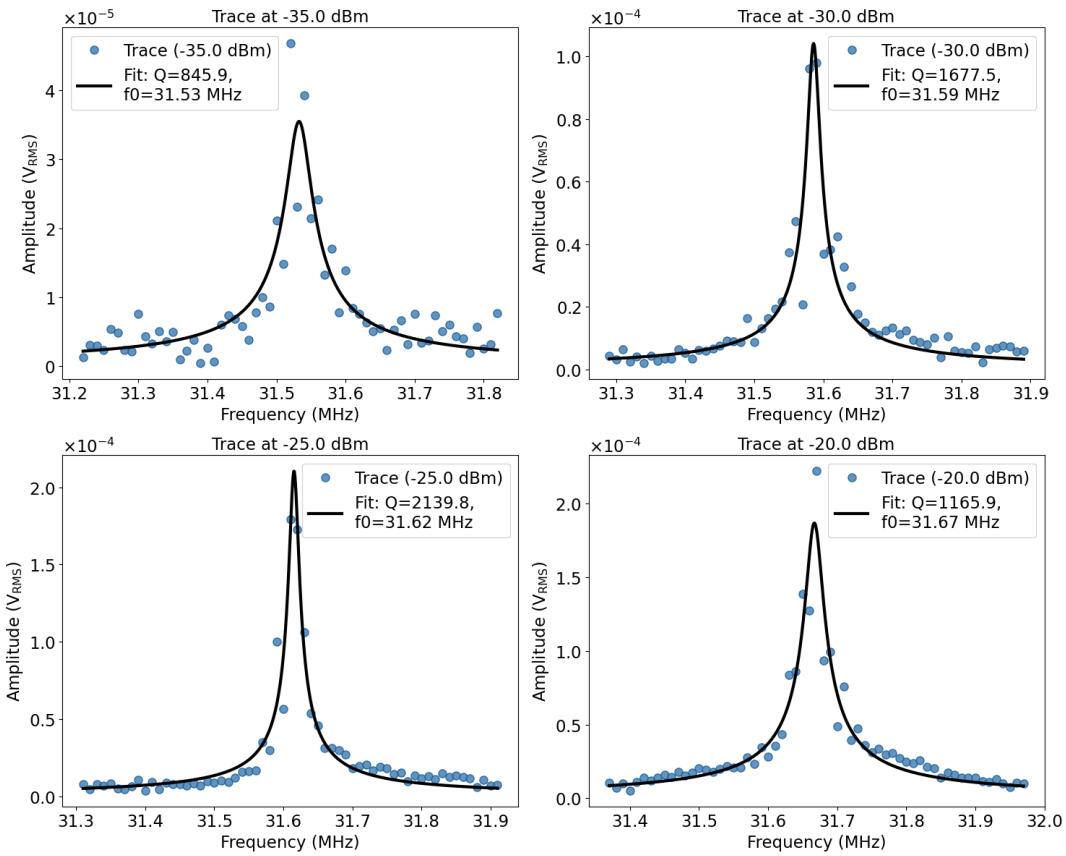

Figure A.1: Experimental data and corresponding linear harmonic oscillator fits of Drum 5 at different driving powers. At these low powers, the membrane is assumed to behave linearly, allowing the linear fits. The Q-factors and resonance frequencies are stated for each power. The amplitude is given in V_{RMS}.

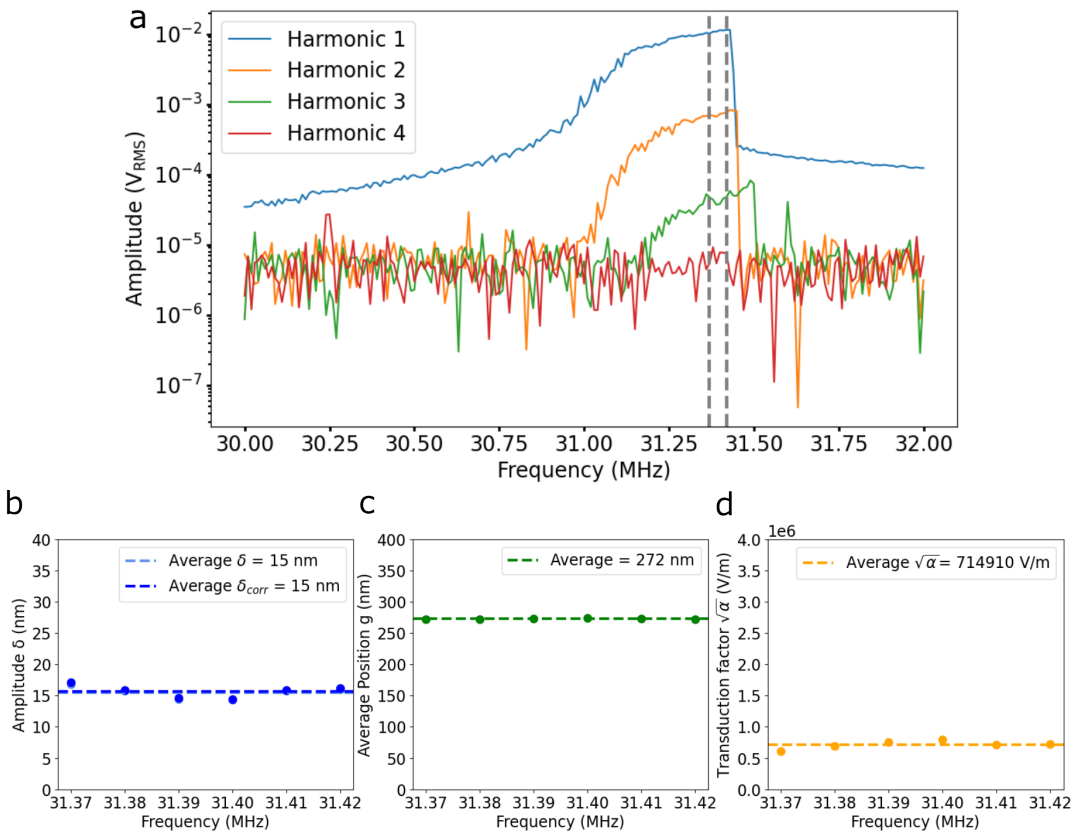

Figure A.2: Amplitude calibration of Drum 5 using harmonics of the fundamental mode. The harmonics were measured at 10 dBm. The vertical dashed lines indicate the frequency window where the amplitude, average position and transduction factor of the resonator were computed. (b) Vibrational amplitude of the resonator with and without correction for nonlinear optical transduction. Due to the low amplitude, nonlinear optical transduction effects can be neglected. (c) Average position and (d) transduction factor of the membrane resonator.

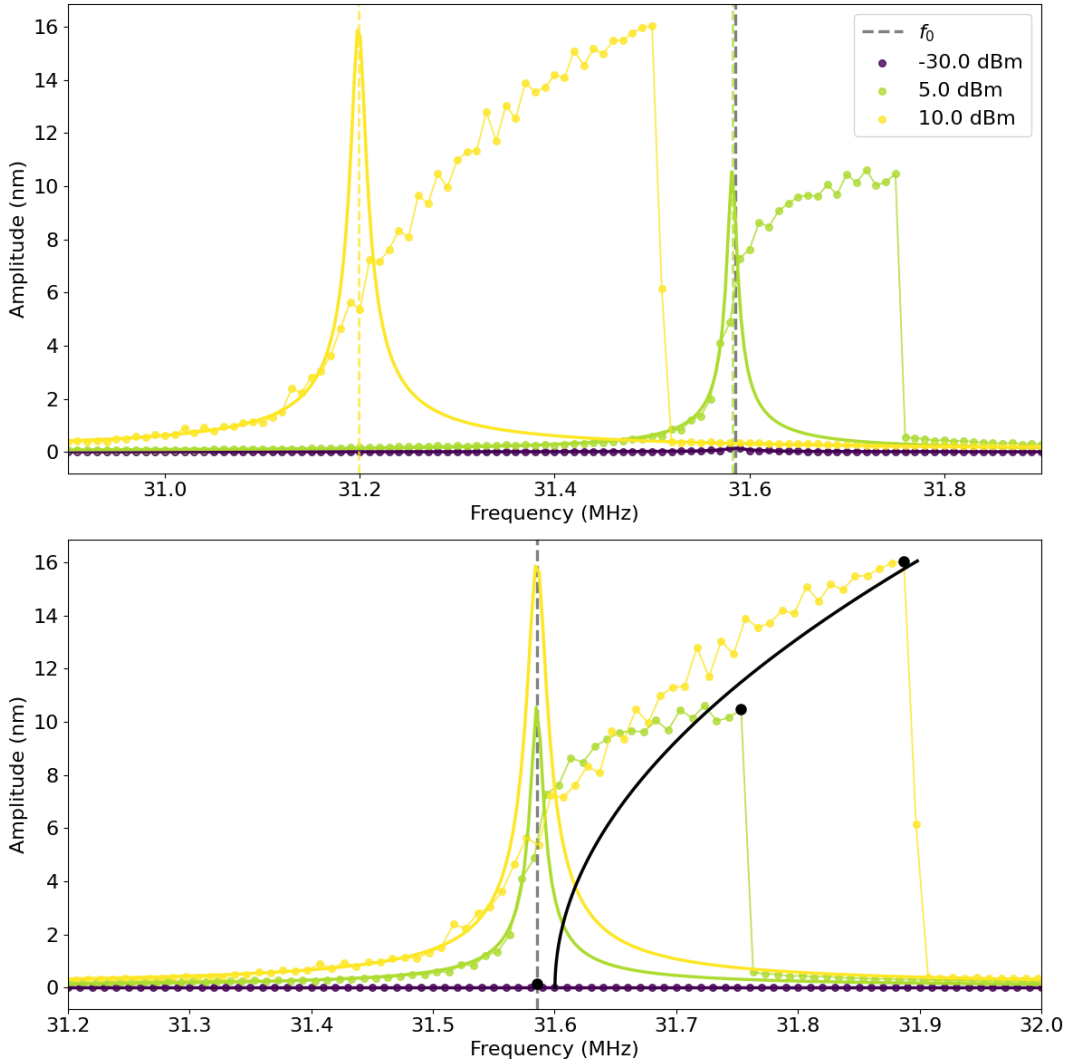

Figure A.3: Power-dependence measurement of Drum 5 at driving powers from -30 dBm to 10 dBm. To correct for the temperature-induced frequency shift, a LHO model is fitted to data far above and below the nonlinear response (see inset). The frequency shift Δf is the difference in frequency from the fitted resonance frequencies to the resonance frequency in the linear regime f_0, which are indicated by dashed vertical lines. Fitting of the backbone curve (Equation 3.9) to the maximum amplitudes of each driving power after correction for temperature fluctuations. The extracted value for the Duffing coefficient from the fit is β = 3.94$\pm$0.3×10^{30} Nm^{-3}kg^{-1}.

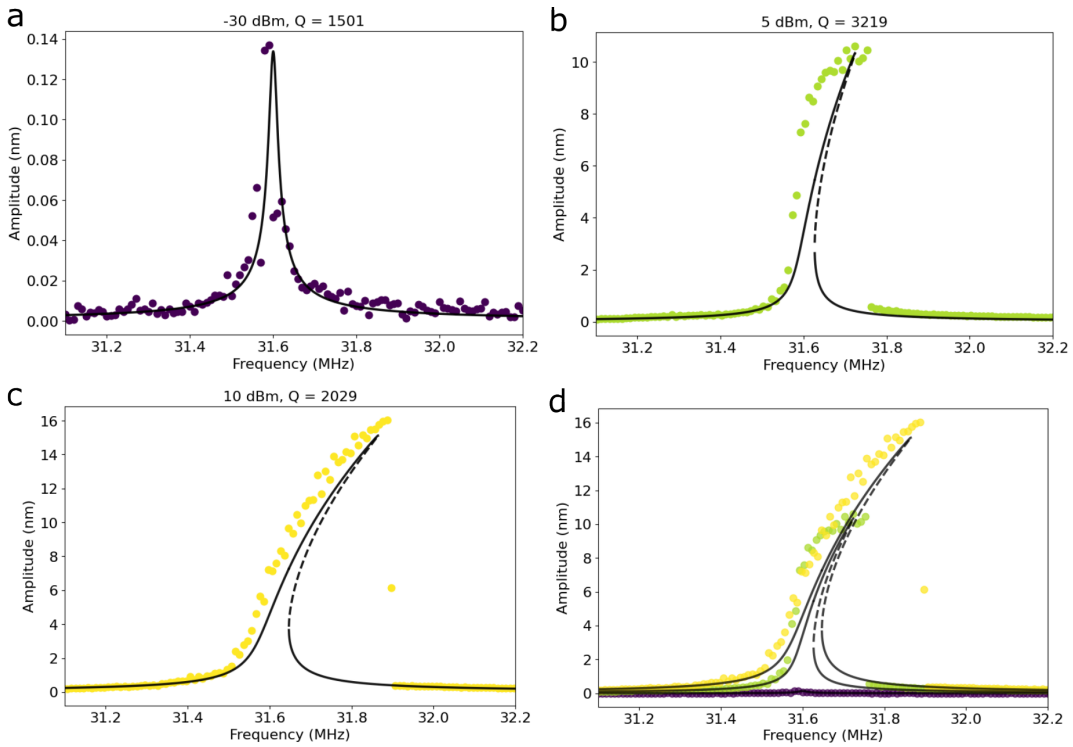

Figure A.4: (a-c) Overlay of the measured and calculated steady state response of the oscillating membrane for increasing driving powers from -30 to 10 dBm of Drum 5. The colored data points correspond to the experimental data, and the black line indicates the steady-state solutions obtained from Equation 2.18. The stable solutions are represented by solid lines, while dashed lines represent the unstable solution. (d) Combined plot showing the experimental data and steady-state solutions for the driving powers of (a-c).

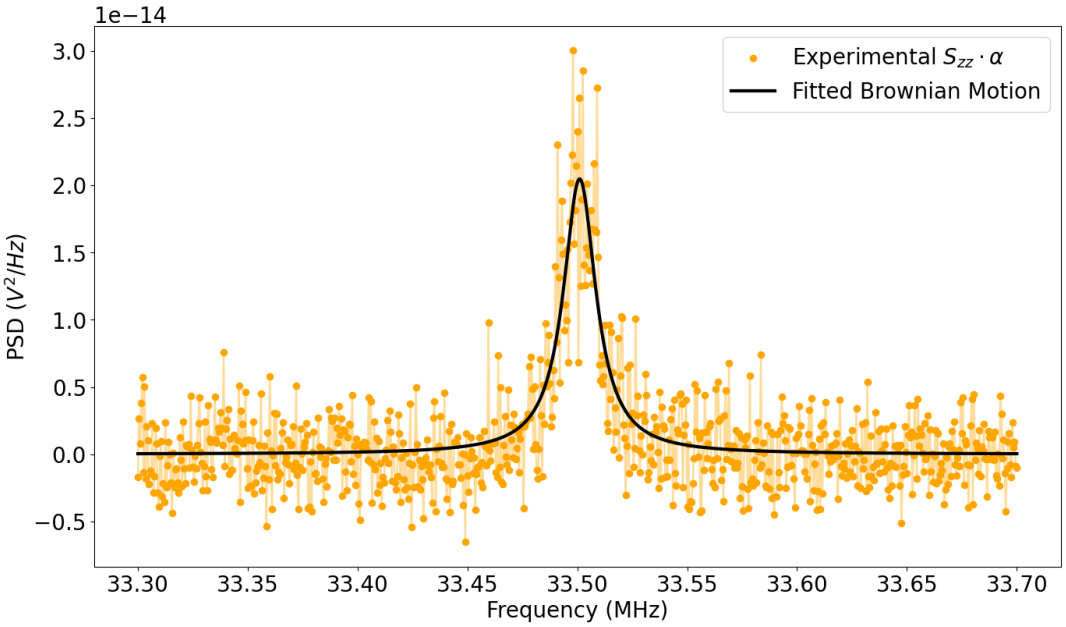

Figure A.5: Measured power spectral density of Drum 5 after subtraction of noise sources together with the corresponding fit to determine the effective mass of the membrane. The value obtained for the effective mass is m_{eff} = 8.51±0.3×10^{-17} kg.

Drum 12

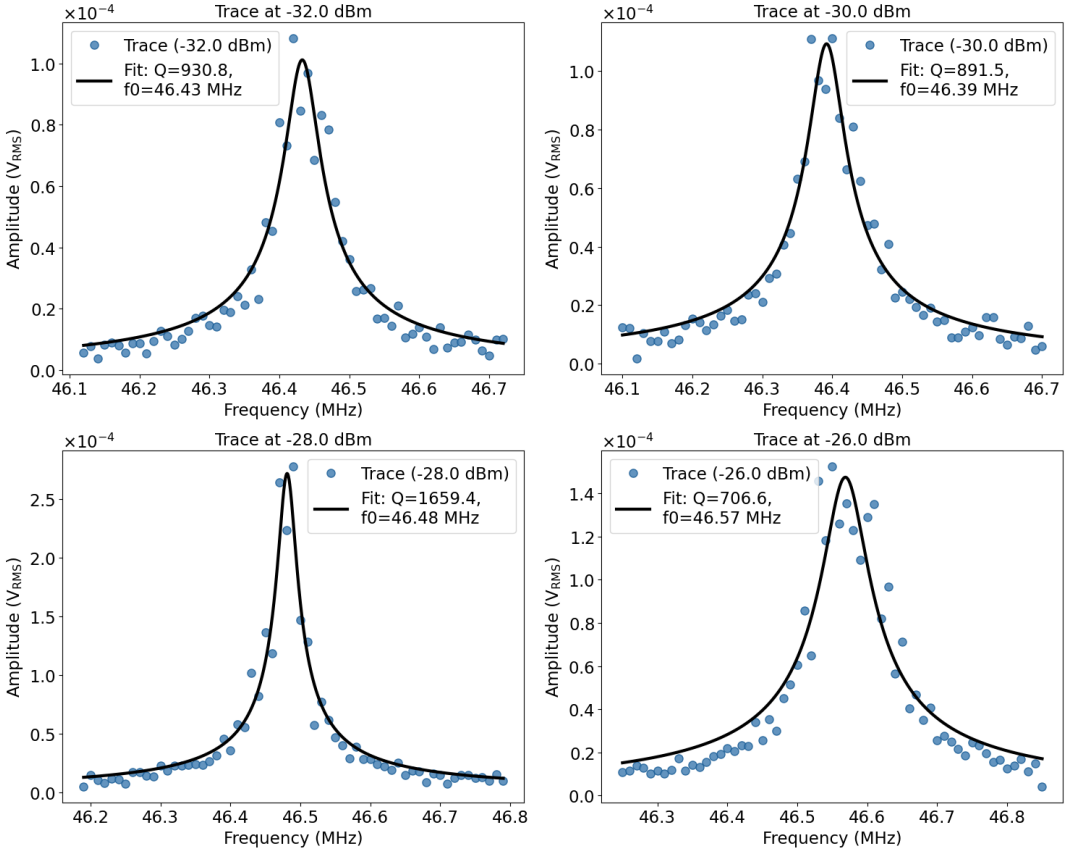

Figure A.6: Experimental data and corresponding linear harmonic oscillator fits of Drum 12 at different driving powers. At these low powers, the membrane is assumed to behave linearly, allowing the linear fits. The Q-factors and resonance frequencies are stated for each power. The amplitude is given in V_{RMS}.

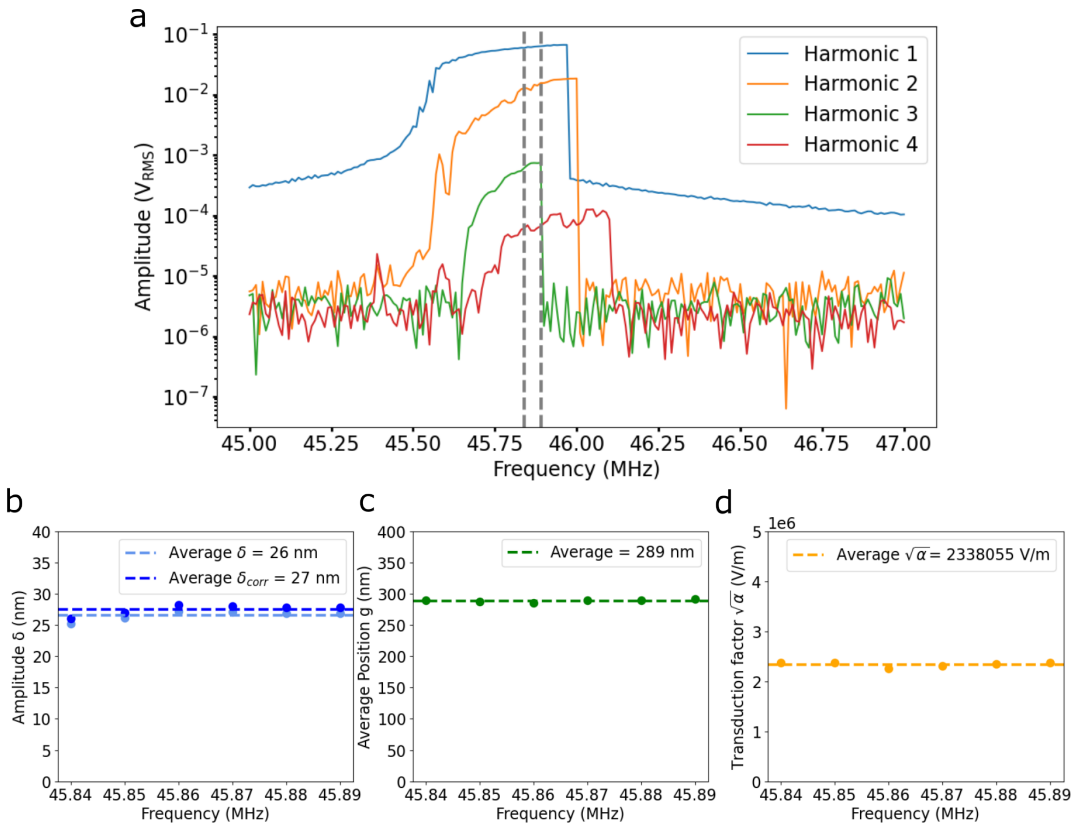

Figure A.7: Amplitude calibration of Drum 12 using harmonics of the fundamental mode. The harmonics were measured at 10 dBm. The vertical dashed lines indicate the frequency window where the amplitude, average position and transduction factor of the resonator were computed. (b) Vibrational amplitude of the resonator with and without correction for nonlinear optical transduction. Due to the low amplitude, nonlinear optical transduction effects can be neglected. (c) Average position and (d) transduction factor of the membrane resonator.

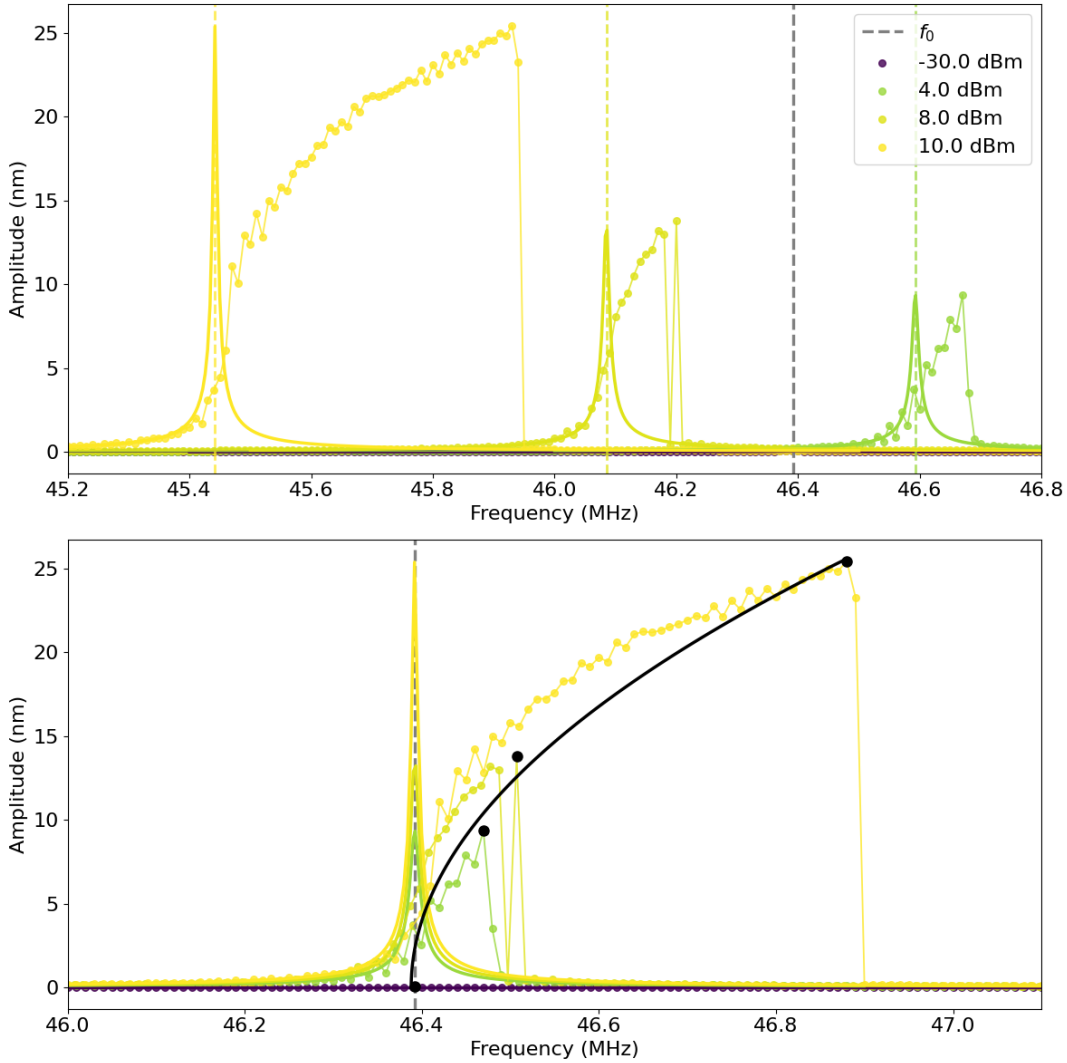

Figure A.8: Power-dependence measurement of Drum 12 at driving powers from -30 dBm to 10 dBm. To correct for the temperature-induced frequency shift, a LHO model is fitted to data far above and below the nonlinear response (see inset). The frequency shift Δf is the difference in frequency from the fitted resonance frequencies to the resonance frequency in the linear regime f_0, which are indicated by dashed vertical lines. Fitting of the backbone curve (Equation 3.9) to the maximum amplitudes of each driving power after correction for temperature fluctuations. The extracted value for the Duffing coefficient from the fit is β = 3.69$\pm$0.2×10^{30} Nm^{-3}kg^{-1}.

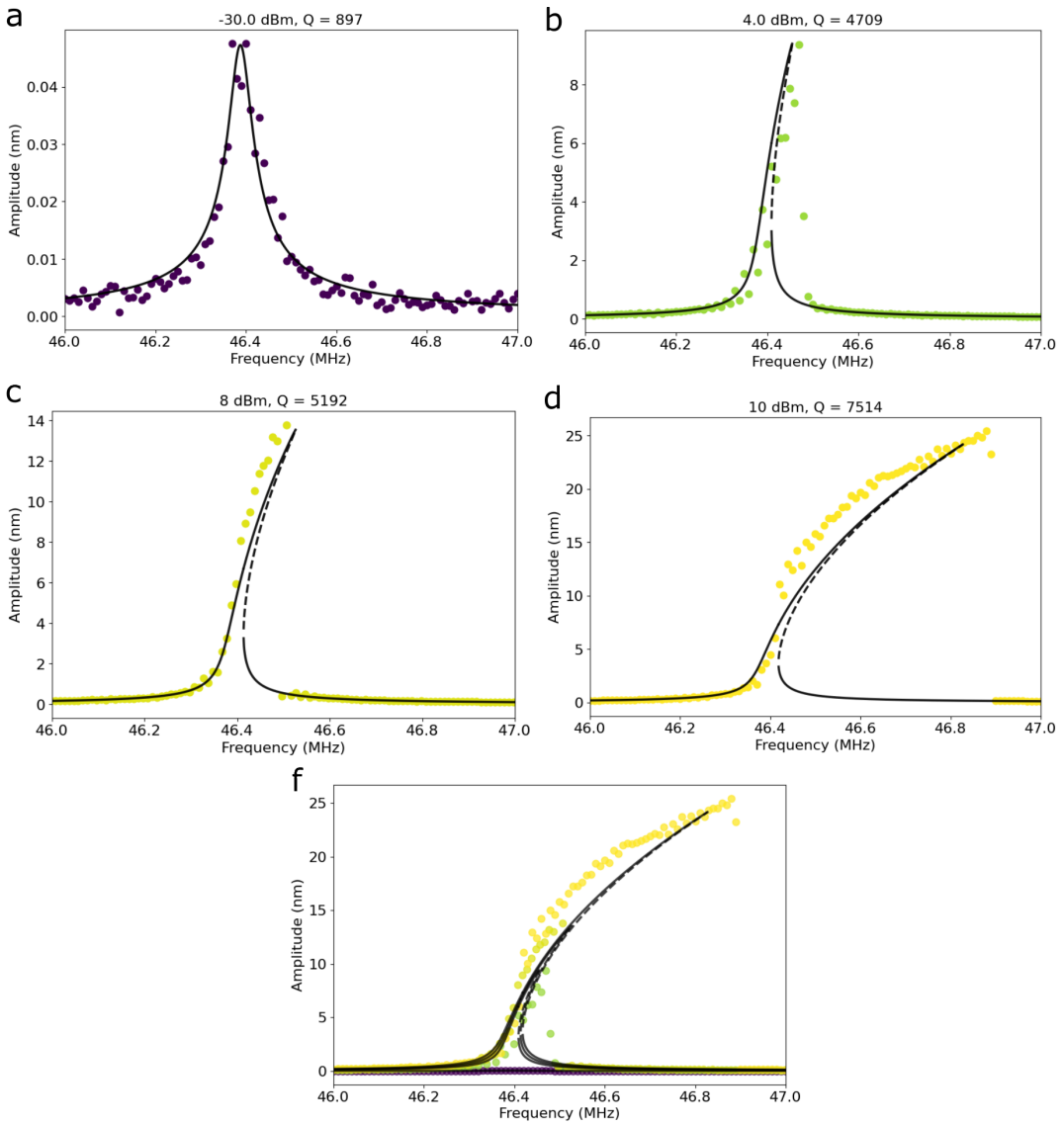

Figure A.9: (a-d) Overlay of the measured and calculated steady state response of the oscillating membrane for increasing driving powers from -30 to 10 dBm of Drum 12. The colored data points correspond to the experimental data, and the black line indicates the steady-state solutions obtained from Equation 2.18. The stable solutions are represented by solid lines, while dashed lines represent the unstable solution. (e) Combined plot showing the experimental data and steady-state solutions for the driving powers of (a-d).

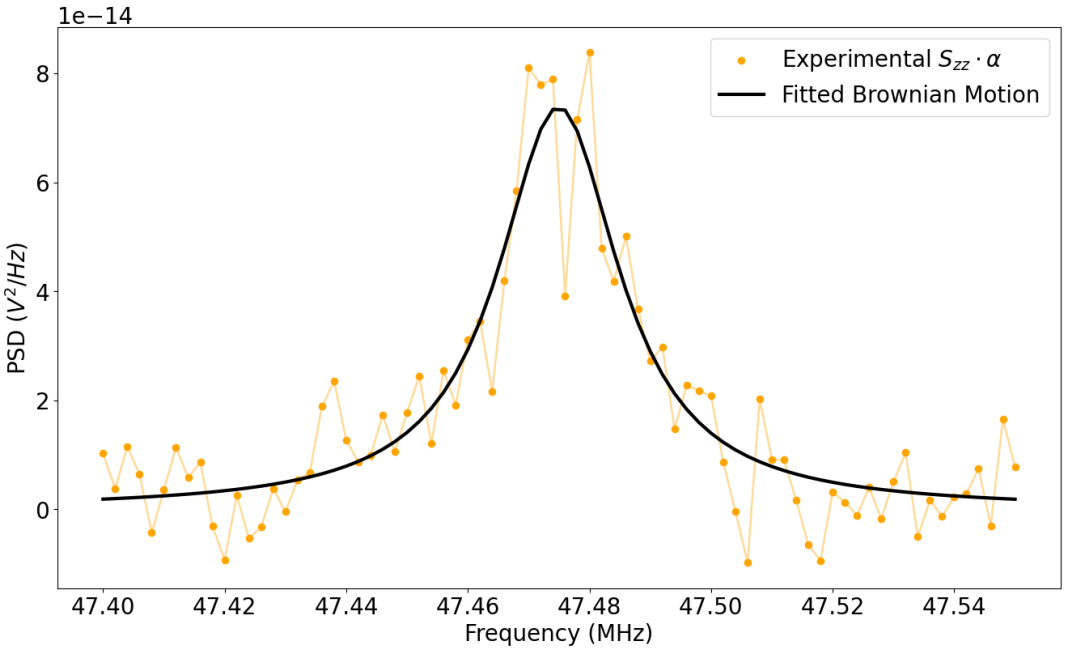

Figure A.10: Measured power spectral density of Drum 12 after subtraction of noise sources together with the corresponding fit to determine the effective mass of the membrane. The value obtained for the effective mass is m_{eff} = 9.35±0.5×10^{-17} kg.

Drum 15

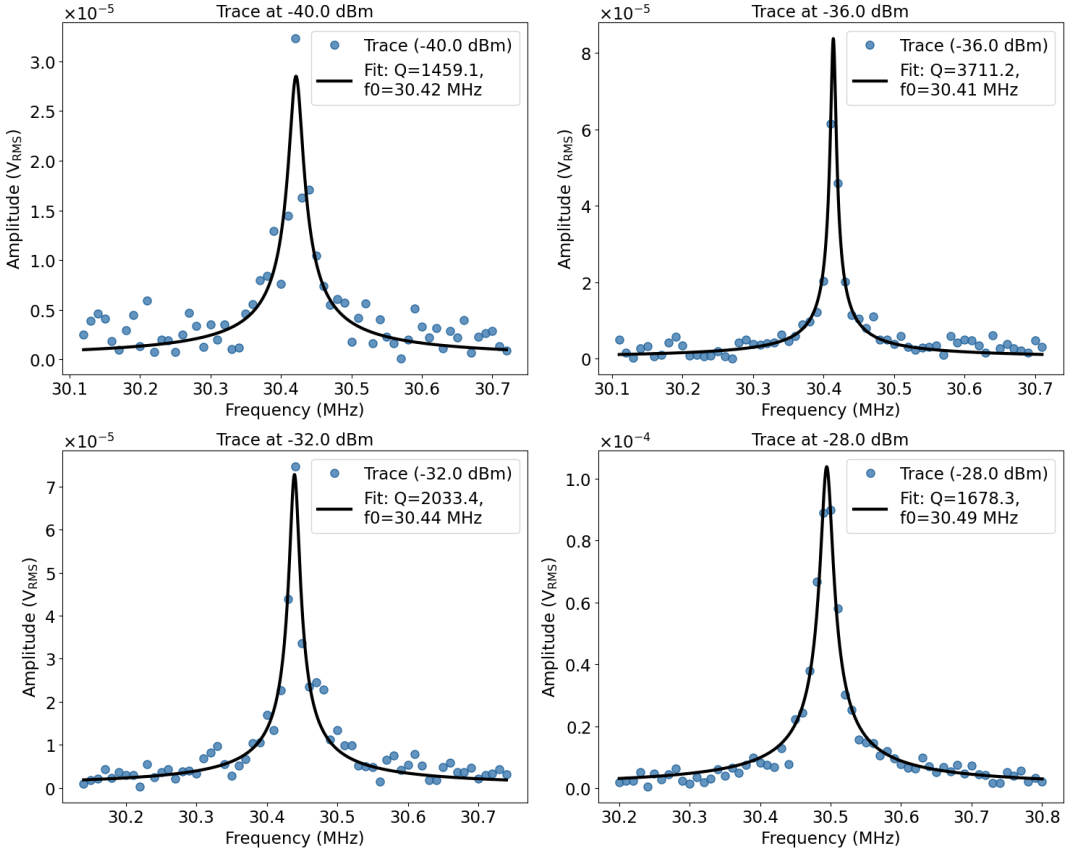

Figure A.11: Experimental data and corresponding linear harmonic oscillator fits of Drum 15 at different driving powers. At these low powers, the membrane is assumed to behave linearly, allowing the linear fits. The Q-factors and resonance frequencies are stated for each power. The amplitude is given in V_{RMS}.

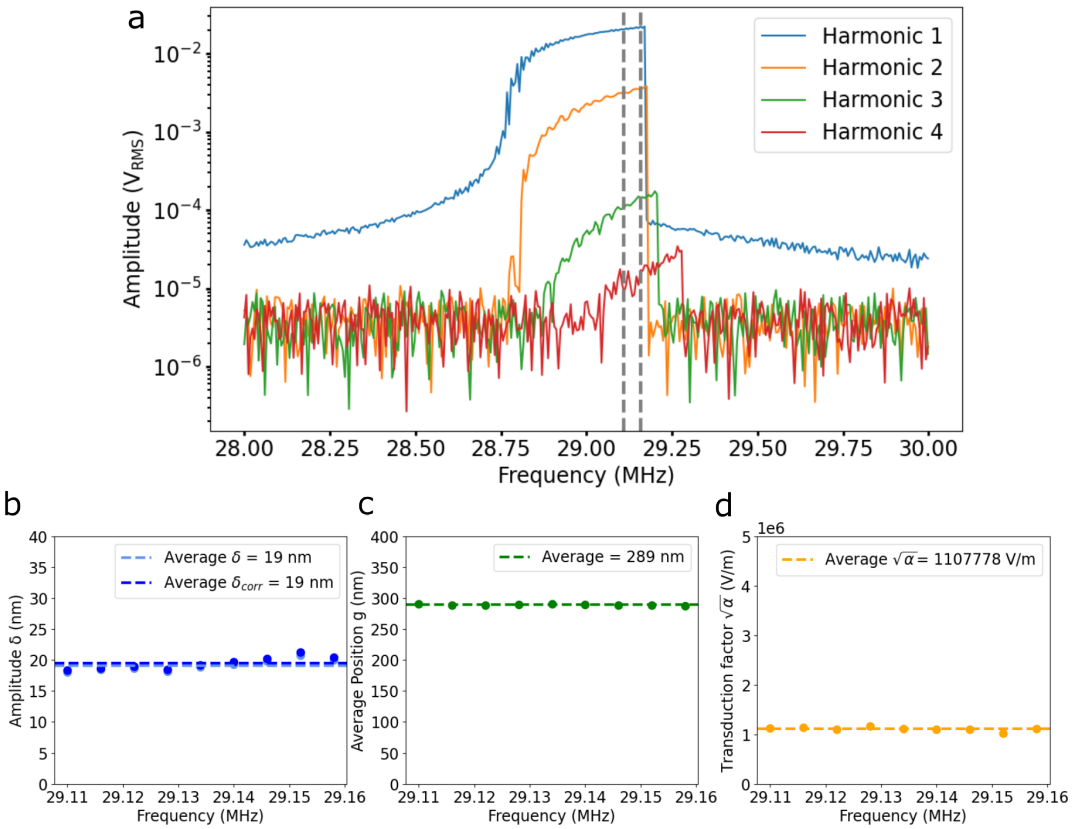

Figure A.12: Amplitude calibration of Drum 15 using harmonics of the fundamental mode. The harmonics were measured at 8 dBm. The vertical dashed lines indicate the frequency window where the amplitude, average position and transduction factor of the resonator were computed. (b) Vibrational amplitude of the resonator with and without correction for nonlinear optical transduction. Due to the low amplitude, nonlinear optical transduction effects can be neglected. (c) Average position and (d) transduction factor of the membrane resonator.

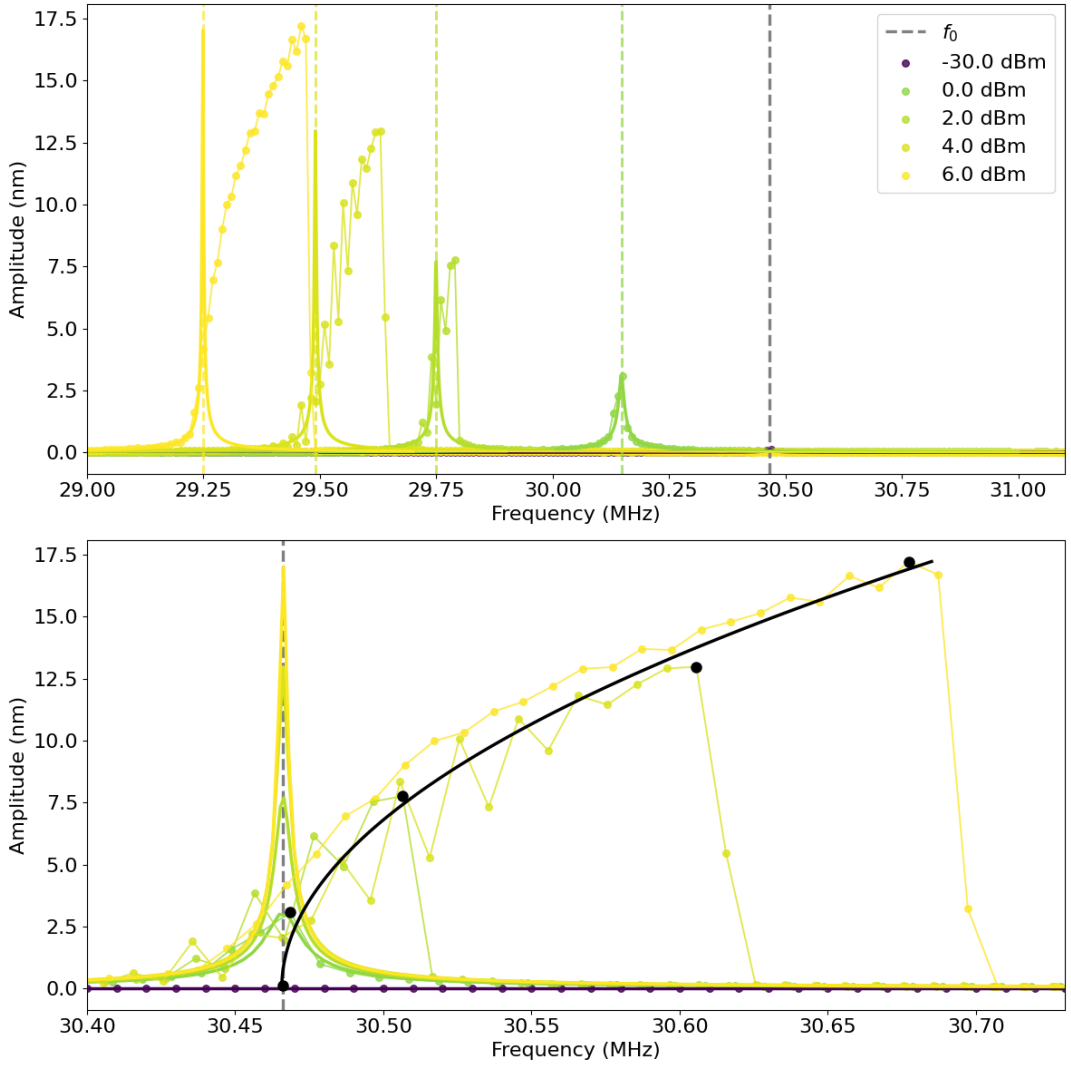

Figure A.13: Power-dependence measurement of Drum 15 at driving powers from -30 dBm to 10 dBm. To correct for the temperature-induced frequency shift, a LHO model is fitted to data far above and below the nonlinear response (see inset). The frequency shift Δf is the difference in frequency from the fitted resonance frequencies to the resonance frequency in the linear regime f_0, which are indicated by dashed vertical lines. Fitting of the backbone curve (Equation 3.9) to the maximum amplitudes of each driving power after correction for temperature fluctuations. The extracted value for the Duffing coefficient from the fit is β = 2.38$\pm$0.1×10^{30} $Nm^{-3}kg^{-1}$.

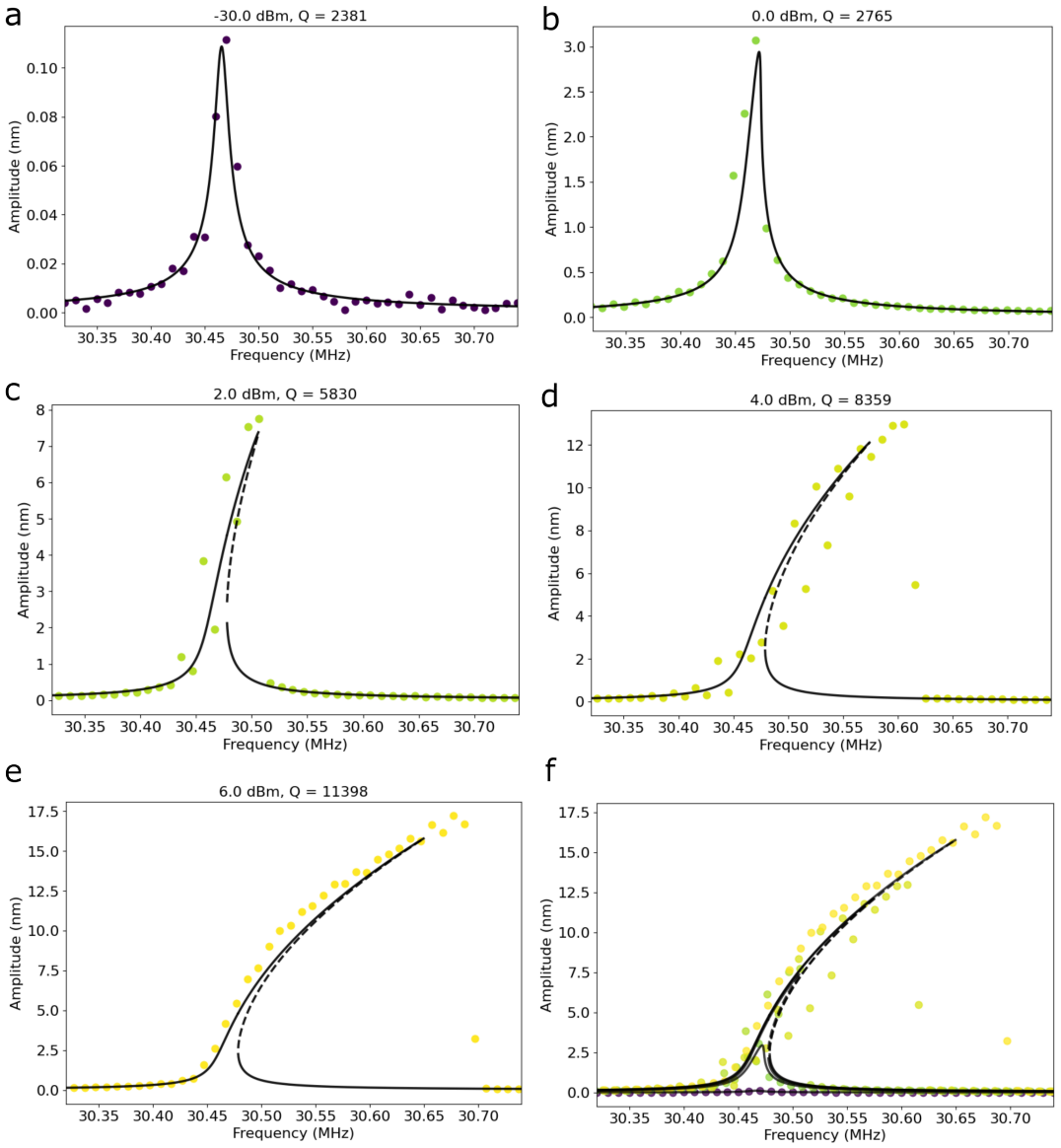

Figure A.14: (a-e) Overlay of the measured and calculated steady state response of the oscillating membrane for increasing driving powers from -30 to 10 dBm of Drum 15. The colored data points correspond to the experimental data, and the black line indicates the steady-state solutions obtained from Equation 2.18. The stable solutions are represented by solid lines, while dashed lines represent the unstable solution. (f) Combined plot showing the experimental data and steady-state solutions for the driving powers of (a-e).

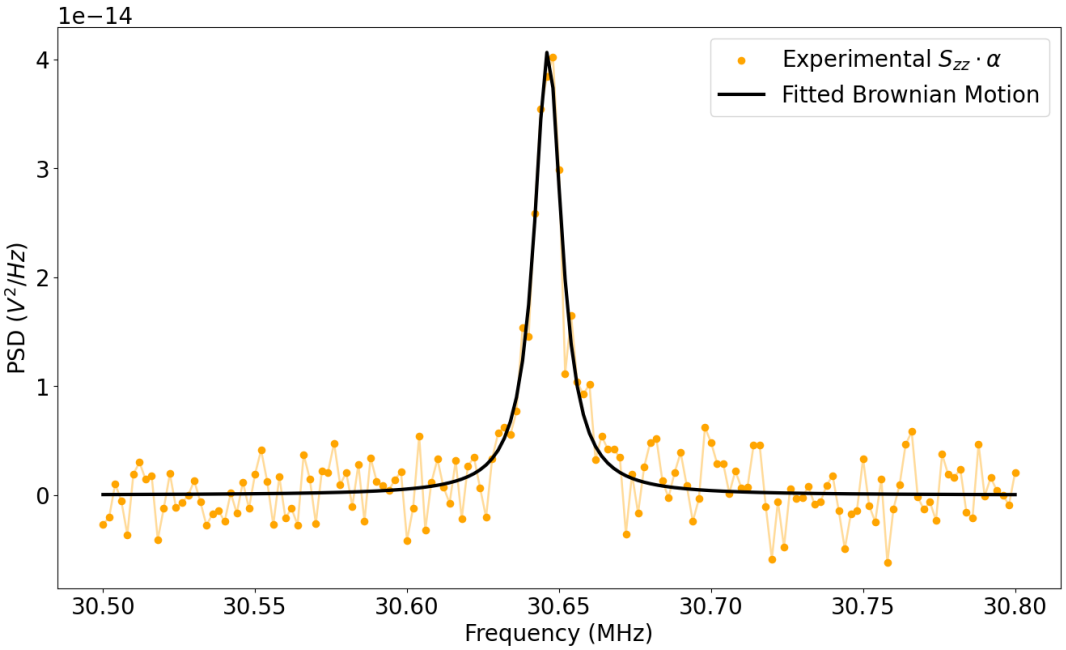

Figure A.15: Measured power spectral density of Drum 15 after subtraction of noise sources together with the corresponding fit to determine the effective mass of the membrane. The value obtained for the effective mass is m_{eff} = 20.1±0.9×10^{-17} kg.

B

Performance Assessment Blue Diode Laser

To avoid the contribution of optical nonlinearities to the measured response of the resonator, the power output of the blue actuation laser is examined. When modulating the intensity of the blue laser, the power output should change linearly with the voltage. For the measurements presented in this thesis, the laser diode controller was set to 45 mA. The maximum modulation power that was set at the VNA was 10 dBm. The voltage change at 10 dBm (0.71 V) can be calculated using Ohm's law and an impedance of the VNA of 50 Ω as:

$$I = U/R = 0.71V/50\Omega = 14.2mA \tag{B.1}$$

Because of the periodic nature of the modulation, the laser current of 45 mA is modulated by $\pm$ 7.1 mA. To control if this is within the linear range of the blue laser, the optical output power of the blue laser is measured as a function of laser current using a power sensor (ThorLabs S120C), which is positioned right in front of the free-space coupler. As apparent from Figure B.1, the laser performs in the linear regime at a modulation of the laser current by 7.1 mA.

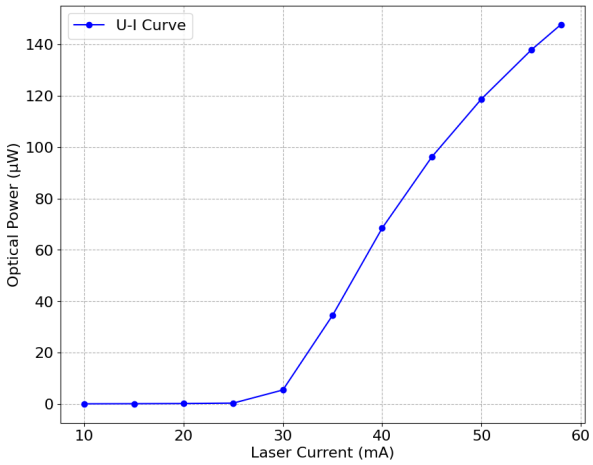

Figure B.1: Optical power output of the blue laser as a function of laser current.

C

Literature Review

The literature review preceding this thesis is presented on the following pages. It discusses the type of defects in graphene and MoS_2 in detail and summarizes theoretical and experimental studies on the relation between Young's modulus and defect concentration.

Effect of Lattice Imperfections on the Mechanical Properties of 2D Material Membranes

MS53010-20 MSE — Literature Research
Master Materials Science and Engineering

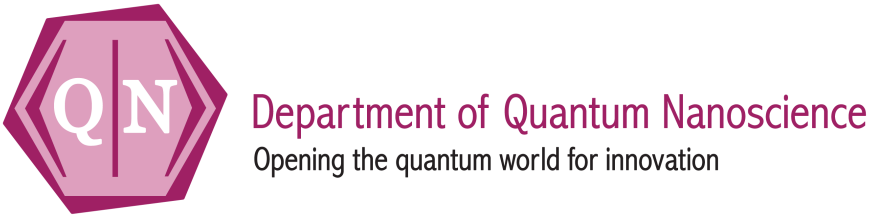

Author: Lukas Pott (5849470)
Supervisor: M.Sc. Álvaro Bermejillo Seco
Examiner: Prof. Dr. Peter Steeneken

Department of Materials Science and Engineering
Faculty of Mechanical Engineering
Delft University of Technology

September 18, 2024

Abstract

This literature review investigates the impact of lattice imperfections on the mechanical properties of two-dimensional (2D) material membranes, focusing specifically on graphene and molybdenum disulfide (MoS_2). The review highlights the significant role of defect engineering in tuning the mechanical properties of these materials, which are crucial for various applications in electronics, sensors, composite reinforcement and nanomechanics. It discusses controversial findings in the field, particularly the study by López-Polín et al., which reported a strong increase in the Young's modulus of suspended graphene by almost the factor of two due to the inclusion of point defects. This contrasts with the majority of studies that observed a monotonous decrease in Young's modulus with increasing defect density. By summarizing experimental and theoretical research, the review identifies critical knowledge gaps in the current understanding and sets the stage for further experimental verification using non-linear dynamic characterization methods in the subsequent master thesis. The goal is to clarify the influence of specific defects on the mechanical properties of graphene and MoS2, and to establish a more comprehensive understanding of how these defects can be engineered for improved material performance.

Contents

List of Figures

Abbreviations

AC	Armchair
AFM	Atomic Force Microscopy
CVD	Chemical Vapor Deposition
DFT	Density Functional Theory
DV defect	Double Vacancy Defect
E_{2D}	In-plane Young's Modulus
FEM	Finite Element Method
FET	Field Effect Transistor
HSLA	High-Strength-Low-Alloy
ME	Mechanical Exfoliation
NEMS	Nanoelectromechanical Systems
PVD	Physical Vapor Deposition
SV defect	Single Vacancy Defect
SW defect	Stone-Wales Defect
TMDC	Transition Metal Dichalcogenides
ZZ	Zigzag

Introduction

1.1 Two-Dimensional Materials

With the scientific study and fabrication of two-dimensional (2D) materials, researchers address current challenges in areas like the semiconductor [1] and medical industry [2], as well as sensor technology [3] and the renewable energy sector [4]. The study of materials that extend only in two dimensions while retaining atomic thickness is crucial, as it allows for significant improvements in chemical, optical, electronic, and mechanical properties. In comparison to their bulk counterparts that are typically held together by van der Waals bonds, atomically thin monolayers from the same element or compound were proven to show tremendously enhanced properties. For example, 2D materials offer improved carrier mobility and thermal conductivity, as well as a tunable band gap and the possibility for chemical functionalization [3, 5].

Concretely, the superior mechanical properties of some 2D materials have aroused great interest, and makes them suitable for applications ranging from sensors [3] to flexible and wearable electronics [6, 7] to reinforcement agents in composites [8, 9]. Due to their atomic thickness and high aspect ratio, monolayers of van der Waals materials typically show very low bending stiffness while maintaining extremely high in-plane strength and stiffness [10]. Within the more than a thousand known and predicted 2D materials [11], typical materials with promising mechanical properties include hexagonal boron nitride (hBN) [12], Xenes [13], molybdenum disulfide (MoS_2) [9] and graphene [14]. Particularly, the two latter are among the most applied and highly studied materials and will thus be in the focus of this report.

The outstanding material properties are not only intrinsically present, but can be tailored specifically to a desired application. The modification of the properties can for example happen via stress [15], strain [15], functionalization [7, 16], or the inclusion of lattice defects [17], with the latter being known as the field of defect engineering.

Besides the relevance of lattice defects for the tunability of mechanical properties of monolayers, defects play a crucial role for applications of 2D materials in photovoltaics, integrated circuits, mechanical and chemical sensors as well as in composite reinforcement [18, 19]. Defects are not only introduced into a material for the improvement of properties, but arise during production and the exposure to ambient conditions and elevated temperatures during the device lifetime. This can have tremendous impact on the device performance, which further demonstrates the need to thoroughly understand the interdependence between mechanical properties and defect kind and concentration.

1.2 State of the Art

Despite the high relevance of defect engineering in 2D materials to tune mechanical properties, the literature has not yet yielded scientific consensus amongst researchers on the influence of defects on these properties. Contradicting results in experimental as well as theoretical studies were reported, and a study of López-Polín *et al.* [20] has further sparked this debate. In 2014, López-Polín and co-workers reported a method to drastically increase the in-plane Young's modulus (E_{2D}) of suspended graphene monolayers via the inclusion of lattice point defects. The remarkable increase of E_{2D} was achieved by introducing low densities of single and di-vacancies of carbon atoms into the material by irradiation with helium ions. At a defect concentration of ~ 0.2 %, the greatest increase in modulus by almost a factor of two from 859 to 1618 GPa was found. The principle of the modulus increase was reasoned to lie in the suppression of thermal out-of-plane membrane fluctuations, which typically occur at room temperature. The suppression of these extended fluctuations is hypothesized to keep the membrane predominantly in the 2D plane, thus increasing the stiffness of suspended graphene monolayers. After an initial increase of E_{2D}, a further increase of the defect density resulted in softening of the graphene membranes. On the contrary, the fracture strength showed a continuous decrease with increasing defect density, which is in line with standard continuum theory.
The remarkable finding of López-Polín *et al.* contrasts with most experimental studies, which report a monotonous decrease of the modulus with increasing defect density, also at low concentrations. However, the majority of the studies on this topic are simulations, and experimental work is lacking and highly challenging. Additionally, López-Polín *et al.* used atomic force microscopy (AFM) nanoindentation to characterize defective samples, which can have certain drawbacks and lead to erroneous results due to high stress concentration, tip morphology variations and material anisotropy [21]. Further, it was shown that freestanding graphene is subject to pronounced thermal fluctuations at room temperature due to the low bending stiffness, essentially reducing the Young's modulus [22, 23]. As a consequence, the commonly applied formulas to derive the Young's modulus from indentation experiments are not directly applicable for crystalline membranes and require modification [22]. These difficulties with nanoindentation measurements have sparked research on alternative, non-contact methods to characterize the mechanical properties of 2D membranes. An established method to achieve this is by exploiting the non-linear duffing response of suspended 2D membranes with interferometry [24]. By applying forced oscillations to the membranes in the GHz regime, the cubic spring constant can be fitted to interferometric measurements, ultimately leading to characterization of the membrane pre-tension and Young's modulus [24]. The analysis via non-linear dynamic characterization provides an alternative experimental to AFM-nanoindentation and has multiple benefits. Contrary to AFM-nanoindentation, it is a non-contact method that provides millions of averages of the measurement parameter per second. Thus, inhomogeneities of the setup and the material are drastically reduced.

In the scope of this literature review, the highly debated study of López-Polín *et al.* will be put into context with existing literature to provide a thorough theoretical fundament for the practical research that will be conducted in the master thesis following this article. The literature review aims to identify the knowledge gaps of current research on the topic of defect engineering in suspended membranes of graphene and MoS_2.

Two-Dimensional Materials

2.1 Graphene

2.1.1 Structure and Defects

Next to diamond and fullerenes, the term graphene describes one of the most commonly known allotropes of carbon. Graphene takes up a two-dimensional structure and consists of purely sp^2-bonded carbon atoms, leading to a so-called honeycomb structure. The honeycomb structure is illustrated in Figure 2.1 a), where the individual carbon atoms are sketched in grey. Along the honeycomb lattice, two directions, the armchair (AC) and zigzag (ZZ) directions, are defined. The armchair direction is along the y-axis in Figure 2.1 a), which resembles the shape of an armchair. The zigzag direction is along the x-axis in the figure. Due to the sp^2-hybridization, the carbon atoms are connected to neighboring atoms with covalent bonds at an angle of 120°. In the honeycomb structure, three of the four valence electrons of carbon form single σ-bonds to neighboring atoms. This C-C bond has a bond energy of 4.9 eV, leading to the remarkable in-plane strength of graphene that is even higher than in sp^3-hybridized diamond [25]. Additionally, the carbon atoms of graphene are contributing to a double bond (π-bond) which is formed by the non-hybridized 2p-orbitals. The 2p-orbitals are oriented orthogonally to the plane of the covalent σ-bonds and form a fully delocalized π-electron system. This delocalization is responsible for the remarkable electronic mobility and conductivity. Naturally, graphene occurs in the stacked form of graphite, where the individual graphene monolayers are connected via van der Waals forces. Due to the low strength of the interlayer forces, the individual graphene layers are easily sheared against each other. For the thickness of a graphene monolayer, no clear definition exists, but often the interlayer spacing in graphite (3.35 Å) is used [14, 26]. The thickness of graphene becomes a relevant quantity when comparing properties of 2D materials with their bulk counterparts or other 3D materials is desired.

During production, exposure to the environment or in the scope of defect engineering, structural defects can be introduced into the graphene monolayer. The introduced defects can be of either intrinsic or extrinsic nature. Intrinsic defects describe lattice faults that are purely related to the chemical nature of the host material, namely single vacancies (SV), agglomerations of vacancies like di-vacancies (DV), line defects or adatoms of the same element or compound. In graphene, a special intrinsic defect is known, which is described as the Stone-Wales (SW) defect. On the other hand, extrinsic defects include physically introduced foreign adatoms or substitutional impurities.

The previously mentioned defects have been widely explored to tailor material properties such as

magnetization, electric and thermal conductivity, surface functionalization and mechanical properties [27]. To influence the mechanical properties of graphene, specific focus lies on the point defects as Stone-Wales and single- as well as multi-vacancy defects, which results from the fact that these defects have the lowest formation energies [28, 29] Thus, they are frequently caused by production processes like CVD and PVD, during crystal growth, rapid cooling and ion bombardment [28, 30].

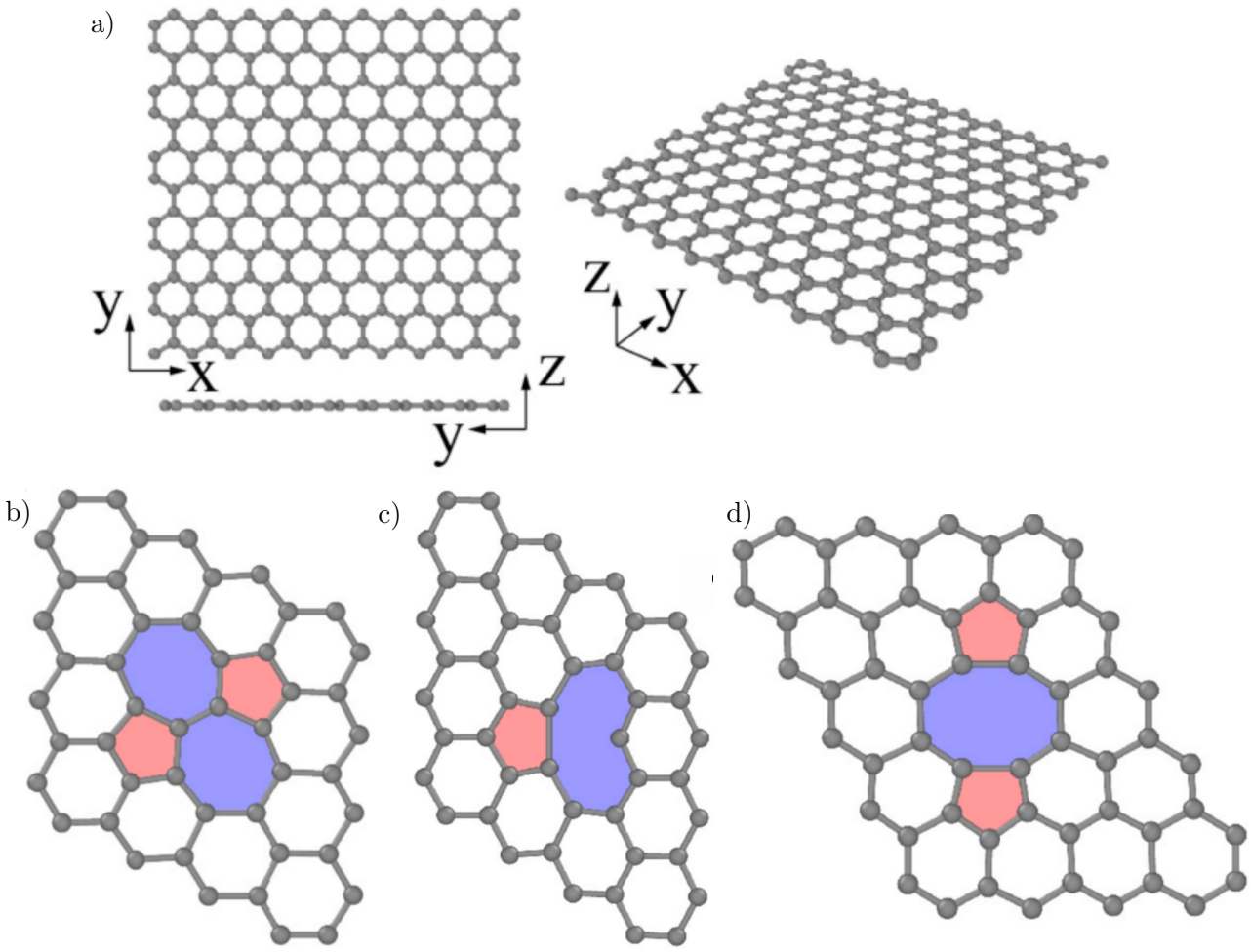

Figure 2.1: Structure of pristine and defective graphene monolayers. a) Pristine, defect-free graphene monolayer b) Stone-Wales (SW) defect caused by rotation of one bond by 90° c) single vacancy (SV) defect and d) di-vacancy (DV) defect in the V_2(5-8-5) configuration. [29]

A Stone-Wales defect is a point defect that does not involve the removal or addition of an atom, but is instead formed by a 90° rotation of one C-C bond. Thus, two pentagons and two heptagons are formed from four initial carbon hexagons, leading to the description of this defect type as an SW(55-77) defect. This defect is highlighted in Figure 2.1 b).

Next to the SW defect, mono- and di-vacancies are relevant for the mechanical properties. The graphene mono-vacancy is depicted in Figure 2.1 c), and is also termed a V_1(5-9) defect. This description originates from the rearrangement of the bond structure due to the vacancy, as it causes the atoms to rearrange forming one pentagon and one nonagon. The introduction of a single vacancy into the graphene lattice causes the formation of one dangling bond, which is oriented towards the vacant lattice site and causes a protrusion of the monolayer [27].

The formation of di-vacancies (DV, Figure 2.1 d)) results from either coalescence of two mono-

vacancies or the removal of two adjacent carbon atoms, which does not entail a dangling bond. Such a vacancy is also called a V_2(5-8-5) defect, indicating the formation of two pentagons and one octagon. A divacancy can rearrange into other lattice configurations, namely V_2(555-777) or V_2(5555-6-7777).

2.1.2 Mechanical Properties

Because of the extraordinary bond strength of the C-C bonds, the planar honeycomb structure provides great strength to materials with this structure. In graphene, record-high values of the Young's modulus along the armchair and zigzag direction were observed, which are substantially higher than materials like the commonly used High-Strength-Low-Alloy-Steels (HSLA, ∼210 GPa [31]) or tungsten carbide (WC, ∼700 GPa [32]). For the armchair direction, experimental and theoretical studies reported Young's moduli ranging from 790 to 1050 GPa [33]. Along the zigzag direction, values of the Young's moduli range from 807 to 1050 GPa [33].
Similarly, the fracture strength of monolayer graphene also varies between the two directions. Along the armchair and zigzag direction, the fracture strength ranges from 93 to 123 GPa and 106 to 137 GPa, respectively [33].

2.2 Molybdenum-Disulfide (MoS_2)

2.2.1 Structure and Defects

After the discovery of scalable routes for the production of graphene in 2004 [34], research on this compound has been carried out extensively to study and modify the outstanding properties this compound offers. However, its zero-bandgap has been limiting the applicability of graphene in logical electronic devices or optical sensors, sparking research on other 2D materials. In this so-called post-graphene era, transition metal dichalcogenides (TMDCs) and more specifically molybdenum disulfide (MoS_2) are amongst the most studied and promising materials.
Monolayer MoS_2 is a semiconducting 2D material with a direct bandgap of 1.8 eV [35] and other promising optical and electrical properties, making it a suitable candidate for the design of nanoscale optical and electrical devices like field effect transistors (FET), photodetectors and solar cells [36].
One monolayer of MoS_2 is made up of three covalently bound hexagonal layers (trilayer structure), namely one molybdenum layer which is sandwiched between two sulfur layers. Six sulfur atoms thus coordinate each molybdenum atom, and each sulfur atom is coordinated by three molybdenum atoms. In Figure 2.2 a) and b), the pristine trilayer structure is depicted from different perspectives. The atomic structure strongly resembles the honeycomb structure of graphene, but consists of two different atoms arranged in a trilayer structure. As a result, the zigzag and armchair directions can also be defined in MoS_2 (Figure 2.2 a): zigzag along x, armchair along y).

The type of defects which are commonly found in monolayer MoS_2 depends on the preparation and growth technique, among which mechanical exfoliation (ME), chemical vapor deposition (CVD), and physical vapor deposition (PVD) are the most commonly applied [36]. Compared to PVD, ME and CVD allow monolayer production of the highest quality [36], and are therefore in the focus of this report. During production of MoS_2 monolayers via ME and CVD, predominantly single (V_S) and

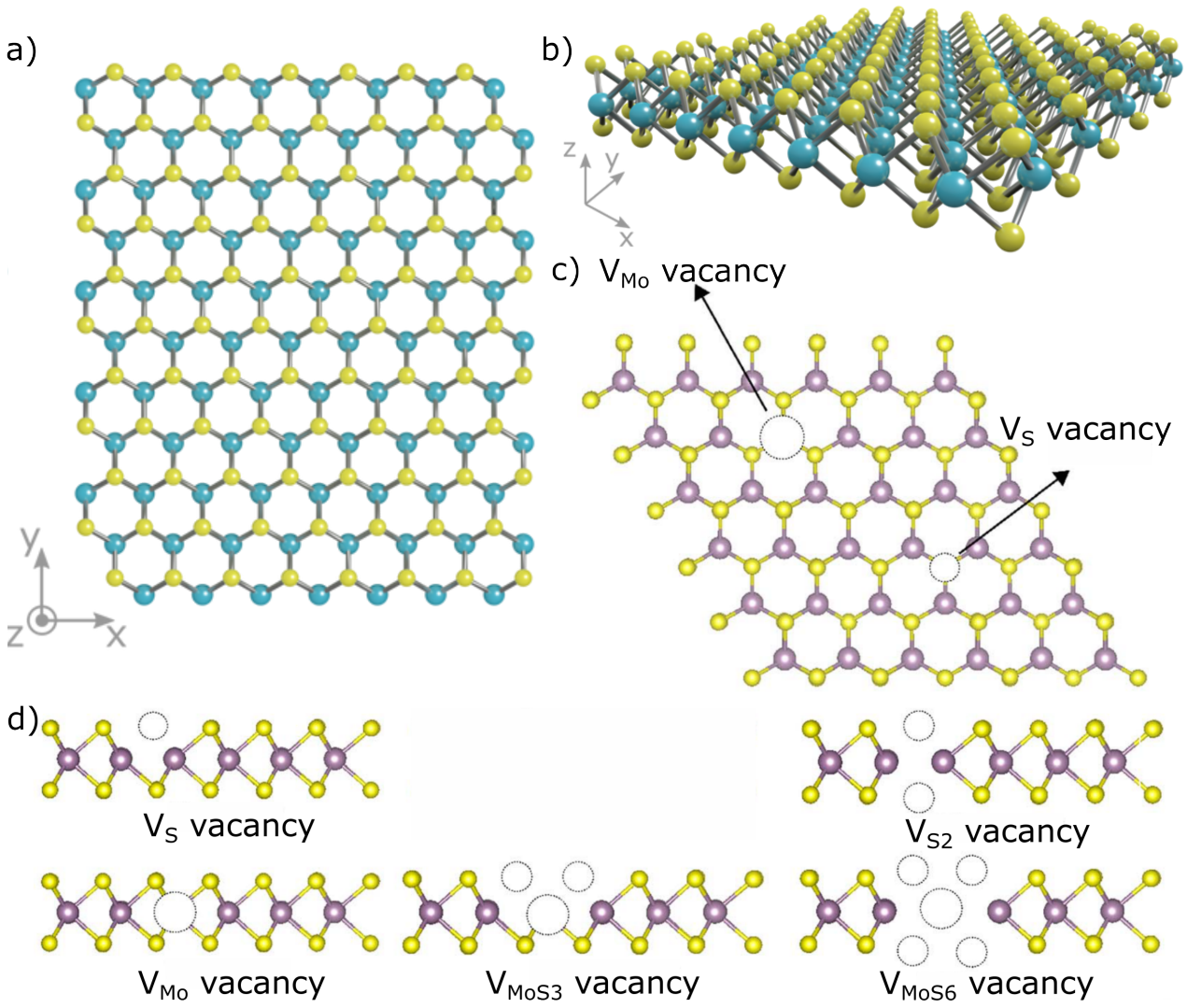

Figure 2.2: Structure of pristine and defective MoS_2 monolayers. Pristine, defect-free monolayer of MoS_2 in a) the top view and b) from the side [37]. Yellow spheres represent sulfur atoms (S), while blue represents molybdenum (Mo). c) Top view of a defective MoS_2 monolayer with Mo and S vacancies. Yellow spheres represent S atoms and purple spheres represent Mo. d) vacancies of one S atom (V_S), two adjacent S atoms (V_{S2}), one Mo atom (V_{Mo}), one Mo and three neighboring S atoms (V_{MoS3}) and one Mo and six adjacent S atoms V_{MoS6}) [38].

double (V_{S2}) sulfur and molybdenum (V_{Mo}) vacancies are created, with V_S being most easily created due to lower formation energy [36]. In the case of a single vacancy of Mo or S, one of these atoms is missing from the lattice, whereas a V_{S2} describes the absence of two adjacent S atoms. In PVD, predominantly antisite defects of Mo on S sites are present [36].
In addition to the previously mentioned defects (Figure 2.2 c)), the vacancy complexes V_{MoS3} and V_{MoS6} are depicted in Figure 2.2 d). These complexes have higher formation energies than the simpler vacancies, but are preferentially created by electron irradiation [39].

2.2.2 Mechanical Properties

As a result of the graphene-like honeycomb structure of monolayer MoS_2, this material has a high intrinsic stiffness and breaking strength. The Young's modulus and strength of MoS_2 are comparable to common steels, but values for the modulus vary significantly between experiments and simulations. Experimental examinations of the Young's modulus range from 270 ± 100 GPa [40] to 330 ± 70 GPa [41], while density functional theory (DFT) simulations report values down to 184 GPa [42]. The experimentally determined breaking strength of MoS_2 monolayers is reported to be 23 GPa [40].

Influence of Lattice Point Defects on Young's Modulus and Breaking Strength

3.1 Graphene

The research on the influence of lattice point defects on the mechanical properties of graphene has yielded highly contradicting results, both in experimental and theoretical studies (Table 3.1, Figure 3.3). To facilitate precise defect engineering and estimate degradation effects during the lifetime of devices incorporating monolayer graphene, a thorough understanding of this matter is of utmost importance.

Intuitively, the introduction of lattice point defects in a crystalline material like graphene is expected to significantly lower the Young's modulus and tensile strength. In comparison to the pristine graphene monolayer, lattice point defects like single and double vacancies reduce the number of strong in-plane σ-bonds, leading to decreased mechanical properties. Such a reduction of strength and stiffness with increasing defect density was observed by the majority of theoretical and experimental studies across all defect concentrations, as shown in Table 3.1.

To study the effect of defects, predominantly theoretical studies were conducted, applying different modelling techniques as molecular dynamics, finite element method (FEM), or parameterization methods (e.g. PM6 Method). As summarized in Table 3.1, the majority of these studies examined the influence of SV and SW defects on Young's modulus and strength, with a limited number of studies also focussing on DV defects. In the presented studies, the concentration of defects ranged from 0.1% to 5%, with a focus on SV and SW defects. These defects are subject to more intensive examination because of their structural simplicity and abundance, as confirmed by experimental and thermodynamic studies [43, 44].

3.1.1 Young's Modulus

At these defect concentrations, a linear decrease of the Young's modulus with increasing defect density is commonly observed, as presented in Figure 3.1. To investigate the influence of SV on a single layer of graphene, Tapia *et al.* [53] employed a uniaxial tensile test via atomistic finite element analysis (FEM). The resulting dependence of the modulus on the areal density of vacancies is depicted in Figure 3.1 a) and was shown to be only slightly affected in the presence of one SV (0.8 % reduction). With a total number of 1050 carbon atoms in the FEM model, a single defect translates to a number defect density of 0.1%. However, an increasing number of vacancies significantly reduced the modulus. In addition

Table 3.1: Comparison of mechanical properties of graphene and monolayer MoS_2 under the influence of defects. To convert the in-plane modulus E^{2D} (Nm^{-1}) to a bulk modulus E^{3D} (Nm^{-2}), it is divided by the thickness of one monolayer (Graphene: 3.35 Å [14], MoS_2: 6.15 Å [45]). *Initial, defect free values. [1]Values corresponding to SV defects (Graphene). AC: Armchair.

Material	Young's Modulus with SV Defects E^{3D} (GPa)[1]	Strength σ (GPa)	Analysed Defect Type	Defect Conc. (%)	Type	Ref.
Graphene	1000	130	—	pristine	AFM	[14]
Graphene	↑ E_{max} =1618 (859*)	↓	SV, DV	0-1.5 (E_{max} at 0.2)	AFM	[20]
Graphene	↑ (1100*)	↓	SV	0.24	PM6	[46]
Graphene	2570 (1350*)	↓	SV	1	Mol. Mech.	[47]
Graphene	↑ E_{max} =1500 (1130*)	↓	SV, SW	0.1-1.5 (E_{max} at 0.2)	Atom. Sim.	[48]
Graphene	↓	↓	SV	0–4	AFM, FEM	[19]
Graphene	1089-972 (1100*)	↓	SV, SW	0.2–4	Mol. Dyn.	[49]
Graphene	N.A.	↓	SV, SW	0.13	Mol. Dyn.	[50]
Graphene	↓	↓	SV	2	Mol. Dyn.	[51]
Graphene	1020-900 (1032*)	↓	SV, SW	0.1-1.4	Mol. Dyn.	[52]
Graphene	AC: 920-580 (910*)	↓	SV, DV, SW	0.4-3.13	Mol. Dyn.	[33]
Graphene	904-889 (931*)	↓	SV, (SW)	0.13–0.52	Atom. Sim.	[44]
Graphene	1034-992 (1042*)	↓	SV	0.1-0.86	FEM	[53]
MoS_2	↓ (211*)	↓	V_S,V_{S2} V_{Mo},V_{MoS3}	N.A.	DFT	[54]
MoS_2	$V_{S/S2}$: 237 V_{Mo}: 234 V_{MoS3}: 229 (237*)	↓	V_S,V_{S2} V_{Mo},V_{MoS_3}	N.A.	DFT	[45]
MoS_2	225.8-219 (226*)	↓	V_{MoS3}	0.1-1	Mol. Dyn.	[55]
MoS_2	AC: 231-219 (232*)	↓	V_{Mo}	0.1-1	Mol. Dyn.	[56]

to the effect of the vacancy density, the authors examined the influence of vacancy distribution on the Young's modulus. It was concluded that the location of vacancies in relation to the tensile direction and general position on the sheet does not result in significant influence of the modulus. This result is in agreement with the findings of Ito *et al.* [57], who reported no difference in the reduction of the modulus between uniformly and randomly distributed SVs.

Dettori *et al.* [44] also investigated the mechanical properties of graphene in the presence of SV defects, and further included SW defects into their research. SVs and SW defects were studied in a defect range of 0.13-0.52 % with a tight-binding atomistic simulation. Based on the simulation, a linear decrease of the modulus with increasing defect concentration was concluded, as apparent from Figure 3.1 d). Contrasting the effect of SVs, SW defects were shown to have a negligible impact on the modulus. In addition to the effect of defects, the authors studied defect-induced stress fields in the monolayer. It was shown that the generated elastic stress fields from point defects are short-ranged ($\sim$10 Å), such that defects in the given concentrations are not influenced by each other.

In agreement with Dettori *et al.*, multiple studies observed a similar difference in the effect of SW and SV defects on the modulus, while observing a linear decrease of E with increasing SV concentration [49, 52]. As depicted in Figure 3.1 b) and c), the effect of SW defects is significantly lower than the effect of SV defects. Hao *et al.* [49] examined the influence at defect concentrations of 0.2-4 % and reason the smoother decay of the stiffness of SW-containing graphene from a structural standpoint. SW defects preserve the sp^2-bonding character of graphene, while SVs lead to dangling bonds and structural instabilities. With an initial modulus of 1.1 TPa in the defect-free state, it drops from 1.089 TPa at 0.2 % to 0.972 TPa at 4 % vacancy concentration. Similarly, the modulus in the study of Jing *et al.* [52] reduced from a defect-free value of 1.032 TPa to 1.02 TPa and 0.890 TPa at SV concentrations of 0.1 % and 1.4 %, respectively. The effect of di-vacancies is stated to be slightly reduced compared to SV defects because of the higher number of dangling bonds created by SV defects. Moreover, the possibility of vacancy defect reconstruction was examined, and shown to stabilize and even increase the modulus compared to the initial state [52].

In the molecular dynamics study of Li *et al.* [33], the effect of defects on the modulus was compared between the zigzag and armchair directions. A significant decrease of the modulus was observed in both directions with increasing defect concentration (0.4-3.13 %), however with different dependencies on the defect type (Figure 3.1 e-f)). In agreement with Jing *et al.*, DV have a reduced impact compared to SV in both orientations. Again, this is attributed to the increased number of dangling bonds of SV compared to DV. In contrast to the previously presented data, SV have an extraordinary influence at a concentration of $\sim$ 0.4 % in the armchair direction. Only at this concentration, SV were calculated to moderately increase the modulus by $\sim$ 10 GPa. This effect is not addressed in the manuscript, thus hindering further interpretation and conclusions.

In contrast to the previously presented research, a limited number of studies report an increase of the modulus at certain defect concentrations ([20, 46–48]), which are summarized in the top section of Table 3.1. The first study on this topic was published in 2010 by Kvashnin *et al.* [47], who carried out a molecular mechanics simulation recreating an experimental AFM nanoindentation measurement. The indentation on circular graphene membranes with diameters from 38 to 140 Å was simulated. It was observed that the initial modulus of 1.35 TPa could be increased by about a factor two, to 2.57 TPa at 1 % of vacancy defects (Figure 3.2 a)). After this initial increase, a continuous reduction

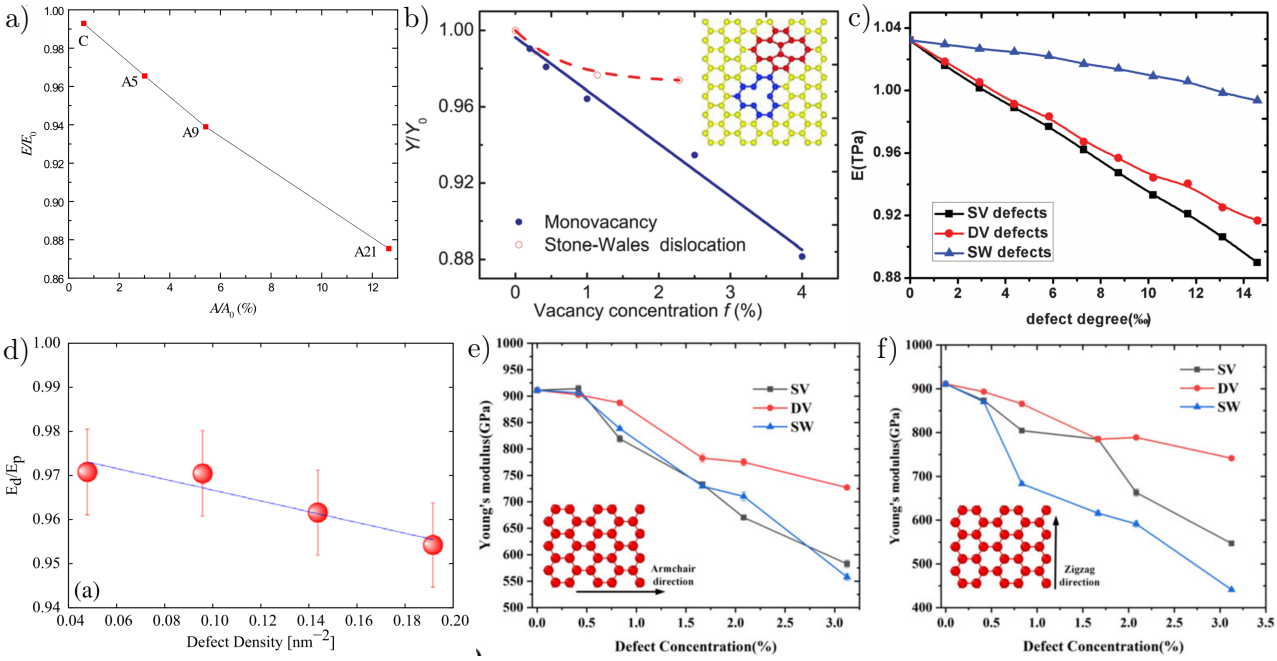

Figure 3.1: Linear decrease of the Young's modulus with increasing density of Stone-Wales defects and single and di-vacancies. Evolution of the modulus versus concentration of a) single vacancies (areal density) [53] b) SV and SW defects [49] c) SV, DV, and SW defects [52] d) single vacancies [44] and e-f) SV, DV, and SW defects [33].

of the modulus with increasing defect concentration followed. The authors propose two competing mechanisms for the initial increase and subsequent decrease in modulus. The initial hardening of graphene at lower defect concentrations is hypothesized to result from geometric rearrangement of the C-C bonds, ultimately leading to shorter and thus stronger bonds near the defects. At higher concentrations, this effect is believed to be counteracted by the decreased density of C-C bonds in the lattice.

The presented research however does not provide information about the validation of the model and the calculation of the modulus from the simulated indentation experiment. Already, the initial modulus of the pristine graphene of 1.35 TPa is significantly higher than the commonly accepted value of $\sim$ 1.0 TPa, hinting to possible inaccuracies in the simulation. Validation of this approach is further aggravated by the lack of supplementary information.

In an experimental study from 2015, López-Polín *et al.* [20] examined the influence of a controlled density of single and di-vacancies on the modulus and strength of graphene membranes via AFM nanoindentation. Similar to the earlier result of Kvashnin *et al.*, a significant increase in the Young's modulus could be observed for low defect concentrations, followed by the commonly expected linear decrease (Figure 3.2 d)). To produce controlled defect densities from 0 to 0.9 %, the samples were irradiated with Ar^+ ions at 140 eV for different time periods. At these conditions, SV and DV are randomly introduced into the graphene lattice at a ratio of 3:1 and are likely to be filled with small atmospheric atoms. In comparison to graphene membranes that were not irradiated (blue curve in Figure 3.2 c)), the in-plane Young's modulus E^{2D} could be increased by almost a factor of two for irradiated membranes (red curve in Figure 3.2 c)) at a defect density of 4×10^{12} cm^{-2} ($\sim$ 0.2 %). The defect content of 0.2 % translates to a mean distance of $\sim$ 5 nm between the defects.

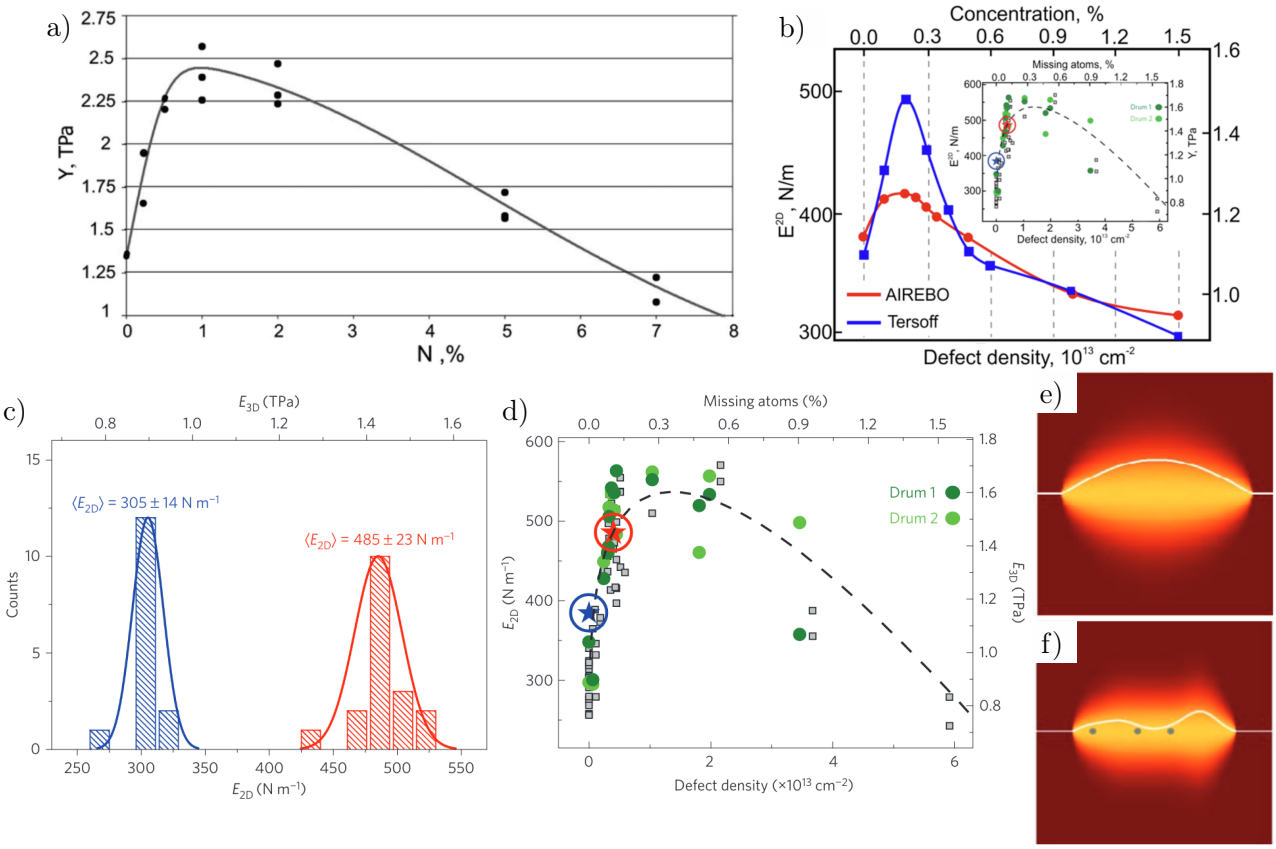

Figure 3.2: Increase of the in-plane Young's modulus of suspended graphene monolayers due to inclusion of lattice defects. Computational studies of the influence of single vacancies on the modulus with molecular dynamics representing AFM nanoindentation (a-b)) [47, 48]. Experimental AFM nanoindentation experiment showing an c) increase of the modulus of ion-irradiated graphene monolayers (red) compared to pristine monolayers (blue), a d) change of the modulus of suspended graphene with increasing density of vacancies and e-f) the hypothesized suppression of long-wavelength thermal fluctuations of the suspended graphene membranes [20].

As opposed to the previously presented results, the authors present a fundamentally different explanation for the increase of the modulus at low defect concentrations. An increase of the modulus is not reasoned with stronger in-plane bonds, but attributed to an influence of vacancy defects on out-of-plane flexural modes. Because of the low bending rigidity of graphene ($\kappa \approx 1$ eV [20]), strong thermal out-of-plane fluctuations with large wavelengths are hypothesized to occur in a suspended, defect-free 2D membrane (Figure 3.2 e)). Upon inclusion of point defects, flexural modes with long wavelengths should be suppressed and the mean free path of the corresponding phonons is reduced. This behavior is schematically depicted in Figure 3.2 f), and hypothesized to be responsible for the drastic modulus increase. At higher defect concentrations, the softening effect caused by reduction of sp^2-bonds is said to become dominating, effectively leading to the linear decrease that was observed before.

In the interpretation of López-Polín *et al.*, their results are in good agreement with an experimental study from Zandiatashbar *et al.* [19], who compared the influence of sp^3-type defects and vacancies on the modulus. The defects were introduced with an oxygen plasma treatment and clear differences in the influence on the modulus were observed. Although a continuous decrease of the modulus was reported in the vacancy defect regime, an increase in E_{2D} at minute concentrations was deemed possible despite differences in the defect nature in both studies ([20], Suppl. Inf. 16).

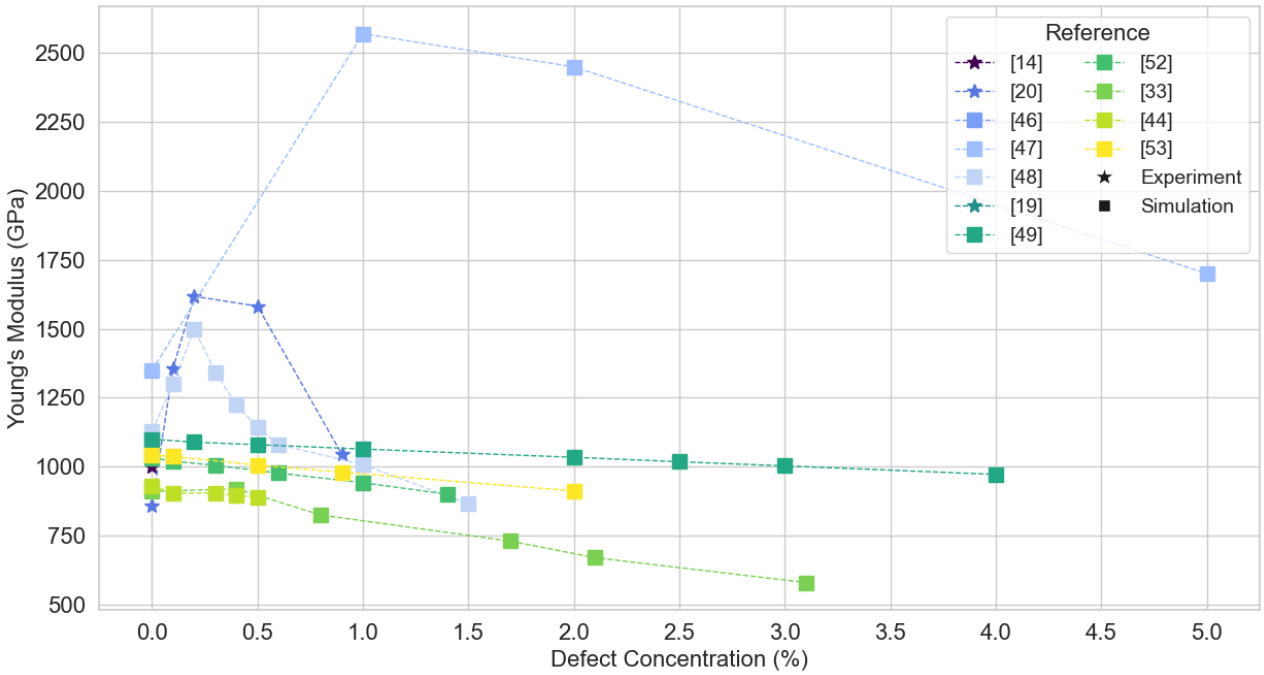

Figure 3.3: Influence of single vacancies on the Young's modulus of graphene monolayers, as published by the presented authors (see Table 3.1). References stating an increase of the Young's modulus are represented by blue shades. Partly, the data in this table was estimated from graphs of the given references, and is thus not exact.

Another study supporting the increase of E_{2D} at low concentrations of monovacancies was published by Kvashnin and Sorokin [48], who carried out atomistic simulations of AFM nanoindentation similarly to the previous study [47] from the same group. Randomly distributed single vacancies with concentrations ranging from 0 to 1.5 % resulted in a similar modulus dependence as the study of López-Polín *et al.* (Figure 3.2 b) and inset). At concentrations from 0.1 to 0.6 %, a significant

modulus increase was reported. Upon inclusion of SW and DV defects into the graphene lattice, no increase was observed, stating the relevance of SV for the modulus increase.

The presented results on SV's are summarized in Figure 3.3, where studies reporting a modulus increase at small defect concentrations (0–1%) are displayed in blue, clearly highlighting the discrepancy compared to results of monotonous modulus decrease. Further, it is differentiated between experimental and computational results.

3.1.2 Breaking Strength

Unlike with the modulus, there is scientific consensus amongst the studies focusing on the breaking strength of defective graphene membranes. All presented studies report a decrease in strength with increasing concentration of SW defects, as well as single and di-vacancies. Also, the reports observing an increase of the modulus found a decrease in strength with increasing defect density. Although López-Polín *et al.* [20] state that classical models fail to describe the influence on the modulus, they explicitly state their compatibility to describe the dependence of the fracture strength.

3.2 MoS_2

3.2.1 Young's Modulus

In comparison with graphene, the literature on the influence of defects on MoS_2 is largely consistent, and no increase in modulus and strength was observed at low or high defect concentrations. Similar to the research on graphene monolayers, experimental studies on the effect of defects are uncommon, and a strong emphasis is placed on computer simulations (see Table 3.1). The most studied defects are vacancies of one (V_S) and two (V_{S2}) sulfur atoms, since they occur most frequently due to their low formation energy compared to other defects [39]. In addition to these defects, multiple studies also examine vacancies of one Mo atom (V_{Mo}) and a group of one Mo atom and three neighboring S atoms (V_{MoS3}).
Multiple DFT studies [45, 54] investigate the influence of the four previously mentioned defects and find limited effects of sulfur vacancies (V_S, V_{S2}) on the modulus. A more pronounced decrease of the modulus was concluded for V_{Mo} and V_{MoS3} defects. In their manuscript, Lorenz *et al.* [45] apply DFT calculations to MoS_2 nanotubes in the zigzag configuration (22,0), which are deemed to be sufficiently comparable to MoS_2 regarding the mechanical properties [58]. For each type of defect, one defect was introduced per (22,0) nanotube. While the vacancies V_S, V_{S2} and V_{Mo} had a very limited effect on the modulus, V_{MoS3} vacancies resulted in the most noticeable decrease of 3.54 % compared to pristine nanotubes. Kazemi *et al.* [54] simulated multiple different TMD materials, including MoS_2, with first-principles DFT. To create the vacancy defects for the simulation, the corresponding atoms were removed from the atomic model. In accordance with Lorenz *et al.* [45], only minor influence of anionic vacancy defects were observed. A more significant reduction of the stiffness resulted from metal and metal complex vacancies, with the strongest reduction caused by molybdenum vacancies.
M. Li and co-authors researched the influence of molybdenum vacancies (V_{Mo}) [56] and molybdenum complex vacancies (V_{MoS3}) [55] with molecular dynamics simulations. V_{Mo} defects were introduced

randomly at concentrations ranging from 0.1 to 1 % and a classical tensile test experiment was simulated. Along the armchair direction, the stiffness was shown to decrease linearly from 232 GPa for the pristine material to 219 GPa for a defect concentration of 1 %. The slope of the armchair configuration compared to zigzag was almost identical with respect to an increasing defect concentration. In both directions, no sign of a stiffness increase was observed at any concentration. The influence of V_{MoS3} was studied at defect concentrations of 0.1 to 1 % and resulted in a similar dependence of the modulus with defects. The stiffness decreased linearly from 226 GPa of the defect-free material to 219 GPa at 1 % of V_{MoS3}. Again, no increase of the modulus was observed for any concentration.

3.2.2 Breaking Strength

Besides studying the influence on the modulus, the strength of the defective monolayers of MoS_2 was also examined. Similar to graphene, the strength decreased with increasing defect density in all presented studies, as apparent from Table 3.1.

Conclusion and Research Plan

4.1 Conclusion

Based on the presented literature review, clear knowledge gaps can be identified regarding the influence of lattice defects on the mechanical properties of 2D material membranes. Specifically, the influence of point defects on the Young's modulus is widely debated, and contradicting results were published.
In typically applied and highly relevant 2D materials like graphene and MoS_2, defects commonly result from exposure to environmental conditions or during production via ME, CVD or PVD. As presented, defects can severely alter the properties of graphene and MoS_2, which can be exploited to tune the material properties for specific applications or research purposes. Despite substantial research initiatives in the past decade, the procedure, also known as defect engineering, has yielded conflicting results in theoretical and experimental studies.
In graphene, the most frequently observed defects are Stone-Wales defects, along with single and double vacancies, owing to their comparatively low formation energies. In the majority of simulations and experimental studies, an inclusion of these defects at concentrations up to 4%, the in-plane Young's modulus decreased continuously with increasing defect fraction. On the contrary, a limited number of studies reported an increase in the modulus by almost a factor of 2 for 0.2 % of vacancy defects. With a mean defect spacing of $\sim$5 nm, the defects are hypothesized to suppress thermal out-of-plane fluctuations of suspended graphene membranes, which would occur in the absence of defects. Resulting from the suppressed thermal fluctuations, the membrane is predominantly kept in the 2D-plane, leading to the enhanced stiffness. However, the increase by almost a factor of two is extremely high and requires subsequent experimental analysis for verification. Small atoms from the atmosphere or the production processes potentially saturate the point defects, which was not included in any of the simulation supporting the hypothesis of modulus increase. Further, inhomogeneities in the structure, wrinkling or varying pre-tension and clamping of the membranes were not included, highlighting the general challenge of exactly reproducing experimental observations in simulations. Lastly, the chosen simulation potential has a strong impact, leading to scattered overall results.

In monolayers of MoS_2, mostly single and double vacancies of sulfur are created, followed by single molybdenum vacancies. Despite the structural similarity to graphene, no increase in modulus was observed in any study on MoS_2 with increasing defect density, although no experimental study on this topic was conducted to date. Thus, it remains unclear whether this is connected to the trilayer structure with two different atoms or has other, currently not identified reasons.

4.2 Research Questions

Because of these highly contradicting results and the great relevance to exhaustively understand defects in 2D materials, further research is required to clarify the effect of single point defects on the Young's modulus at low concentrations between 0.1 and 0.6 %.
In the thesis, the mechanical properties of defective graphene and MoS_2 will be characterized experimentally via non-linear dynamics as an alternative, non-contact method to conventional AFM nanoindentation and theoretical simulations [24]. MoS_2 is chosen as a reference material for graphene due to the strong similarities in their atomic structures, which could lead to similar effects of defects on their elastic modulus. The defect concentrations of the membranes to be studied will be of the same magnitude as in the reference studies presented in this review to ensure comparability.

In the experimental part of the master thesis, the following primary research question will be addressed.

Primary Question:

1. How do atomic-scale defects influence the Young's modulus of graphene, as measured through non-linear dynamic characterization?

To help answer the primary question and put the results in the larger scientific context, the following sub-questions will be examined.

Subquestions:

1. Can trends in the mechanical influence of defects observed in graphene also be found in structurally similar 2D materials like MoS_2?
2. What are the benefits and disadvantages of non-linear dynamic characterization compared to the commonly applied AFM nanoindentation?
3. How do precision and accuracy of non-linear dynamic characterization and AFM nanoindentation compare in mechanical characterization?
4. What challenges arise in the calibration process and error estimation during the nonlinear dynamic characterization of suspended membranes?

4.3 Research Plan

As presented, experimental studies on the influence of point defects on the modulus are clearly underrepresented, for graphene as well as MoS_2. Also, the mechanism of modulus enhancement is still highly debated, and requires further proof. To shed light on this controversial matter, the following experimental research will be conducted during the master thesis.

With the utilization of non-linear dynamics, the Young's modulus of MoS_2 and graphene will be studied at varying concentrations of point defects. To ensure comparability with the experimental study

of López-Polín *et al.*, the defect type and concentration will be similar. Point defects at 10 different concentrations ranging from $1.00 * 10^{12}$ to $1.00 * 10^{15}$ will be introduced into suspended monolayers of MoS_2 and graphene via irradiation with helium ions. For the non-linear characterization, the monolayers will be suspended over circular cavities on a silicon chip with 4 µm diameter. The project will be executed in collaboration with the group of Otakar Frank, Department of Electrochemical Materials at the Czech Academy of Sciences. The team of Otakar Frank will prepare the samples, introduce the defects by irradiation and characterize the defects.
A detailed research plan for characterization of the Young's modulus of defective graphene and MoS_2 membranes is listed on the following page.

Action plan	2024									
	Mar	Apr	May	Jun	Jul	Aug	Sep	Oct	Nov	Dec
1. Study the theoretical background and write Literature Review										
2. Get acquainted with measurement setup and hands-on practice										
3. Fixing the experimental setup, installing new PC and explore resonance of 2 µm Drums										
4. Obtaining first data of non-linear membrane dynamics and establish proper fitting procedure										
5. Measuring and fitting drums with varying defect concentrations to extract Young's modulus										
6. Analysis of experimental results, writing of master thesis and preparation of presentation										

References

1. Iannaccone, G., Bonaccorso, F., Colombo, L. & Fiori, G. Quantum engineering of transistors based on 2D materials heterostructures. en. *Nature Nanotechnology* **13,** 183–191. ISSN: 1748-3395. https://www.nature.com/articles/s41565-018-0082-6 (2024) (Mar. 2018).
2. Tatullo, M. *et al.* Phosphorene Is the New Graphene in Biomedical Applications. *Materials* **12.** ISSN: 1996-1944. https://www.mdpi.com/1996-1944/12/14/2301 (2019).
3. Lemme, M. C. *et al.* Nanoelectromechanical Sensors Based on Suspended 2D Materials. en. *Research* **2020,** 2020/8748602. ISSN: 2639-5274. https://spj.science.org/doi/10.34133/2020/8748602 (2024) (Jan. 2020).
4. Khan, K. *et al.* Going green with batteries and supercapacitor: Two dimensional materials and their nanocomposites based energy storage applications. *Progress in Solid State Chemistry* **58,** 100254. ISSN: 0079-6786. https://www.sciencedirect.com/science/article/pii/S0079678619300238 (2020).
5. Glavin, N. R. *et al.* Emerging Applications of Elemental 2D Materials. en. *Advanced Materials* **32,** 1904302. ISSN: 1521-4095. https://onlinelibrary.wiley.com/doi/abs/10.1002/adma.201904302 (2024) (2020).
6. Zhang, Z. *et al.* Rosin-enabled ultraclean and damage-free transfer of graphene for large-area flexible organic light-emitting diodes. en. *Nature Communications* **8,** 14560. ISSN: 2041-1723. https://www.nature.com/articles/ncomms14560 (2024) (Feb. 2017).
7. Lee, Y. H. *et al.* Flexible high-performance graphene hybrid photodetectors functionalized with gold nanostars and perovskites. en. *NPG Asia Materials* **12,** 1–12. ISSN: 1884-4057. https://www.nature.com/articles/s41427-020-00260-1 (2024) (Dec. 2020).
8. Qadir, A. *et al.* Representative 2D-material-based nanocomposites and their emerging applications: a review. en. *RSC Advances* **11,** 23860–23880. ISSN: 2046-2069. http://xlink.rsc.org/?DOI=D1RA03425A (2024) (2021).
9. Dong, M. *et al.* Multifunctional epoxy nanocomposites reinforced by two-dimensional materials: A review. en. *Carbon* **185,** 57–81. ISSN: 00086223. https://linkinghub.elsevier.com/retrieve/pii/S0008622321009003 (2024) (Nov. 2021).
10. Hou, Y. *et al.* Tuning instability in suspended monolayer 2D materials. en. *Nature Communications* **15,** 4033. ISSN: 2041-1723. https://www.nature.com/articles/s41467-024-48345-7 (May 2024).

11. Mounet, N. *et al.* Two-dimensional materials from high-throughput computational exfoliation of experimentally known compounds. en. *Nature Nanotechnology* **13,** 246–252. ISSN: 1748-3387, 1748-3395. https://www.nature.com/articles/s41565-017-0035-5 (2024) (Mar. 2018).

12. Falin, A. *et al.* Mechanical properties of atomically thin boron nitride and the role of interlayer interactions. en. *Nature Communications* **8,** 15815. ISSN: 2041-1723. https://www.nature.com/articles/ncomms15815 (2024) (June 2017).

13. Wang, T. *et al.* Xenes as an Emerging 2D Monoelemental Family: Fundamental Electrochemistry and Energy Applications. en. *Advanced Functional Materials* **30,** 2002885. ISSN: 1616-3028. https://onlinelibrary.wiley.com/doi/abs/10.1002/adfm.202002885 (2024) (2020).

14. Lee, C., Wei, X., Kysar, J. W. & Hone, J. Measurement of the Elastic Properties and Intrinsic Strength of Monolayer Graphene. en. *Science* **321,** 385–388. ISSN: 0036-8075, 1095-9203. https://www.science.org/doi/10.1126/science.1157996 (2024) (July 2008).

15. Peng, Z., Chen, X., Fan, Y., Srolovitz, D. J. & Lei, D. Strain engineering of 2D semiconductors and graphene: from strain fields to band-structure tuning and photonic applications. en. *Light: Science & Applications* **9,** 190. ISSN: 2047-7538. https://www.nature.com/articles/s41377-020-00421-5 (2024) (Nov. 2020).

16. Georgakilas, V. *et al.* Functionalization of Graphene: Covalent and Non-Covalent Approaches, Derivatives and Applications. *Chemical Reviews* **112.** Publisher: American Chemical Society, 6156–6214. ISSN: 0009-2665. https://doi.org/10.1021/cr3000412 (2024) (Nov. 2012).

17. Cao, Q. *et al.* A Review of Current Development of Graphene Mechanics. en. *Crystals* **8,** 357. ISSN: 2073-4352. http://www.mdpi.com/2073-4352/8/9/357 (2024) (Sept. 2018).

18. Komsa, H.-P. & Krasheninnikov, A. V. in *Defects in Two-Dimensional Materials* (eds Addou, R. & Colombo, L.) 7–41 (Elsevier, Jan. 2022). ISBN: 978-0-12-820292-0. https://www.sciencedirect.com/science/article/pii/B9780128202920000082 (2024).

19. Zandiatashbar, A. *et al.* Effect of defects on the intrinsic strength and stiffness of graphene. en. *Nature Communications* **5.** Publisher: Nature Publishing Group, 3186. ISSN: 2041-1723. https://www.nature.com/articles/ncomms4186 (2024) (Jan. 2014).

20. López-Polín, G. *et al.* Increasing the elastic modulus of graphene by controlled defect creation. en. *Nature Physics* **11,** 26–31. ISSN: 1745-2473, 1745-2481. https://www.nature.com/articles/nphys3183 (2024) (Jan. 2015).

21. Rosenhek-Goldian, I. & Cohen, S. R. Some considerations in nanoindentation measurement and analysis by atomic force microscopy. en. *Journal of Vacuum Science & Technology A* **41,** 062801. ISSN: 0734-2101, 1520-8559. https://pubs.aip.org/jva/article/41/6/062801/2922084/Some-considerations-in-nanoindentation-measurement (2024) (Dec. 2023).

22. Los, J. H., Fasolino, A. & Katsnelson, M. I. Mechanics of thermally fluctuating membranes. en. *npj 2D Materials and Applications* **1,** 9. ISSN: 2397-7132. https://www.nature.com/articles/s41699-017-0009-3 (2024) (May 2017).

23. Lopez-Polin, G., Gomez-Navarro, C. & Gomez-Herrero, J. The effect of rippling on the mechanical properties of graphene. en. *Nano Materials Science* **4,** 18–26. ISSN: 25899651. https://linkinghub.elsevier.com/retrieve/pii/S2589965121000234 (Mar. 2022).

24. Davidovikj, D. *et al.* Nonlinear dynamic characterization of two-dimensional materials. en. *Nature Communications* **8,** 1253. ISSN: 2041-1723. https://www.nature.com/articles/s41467-017-01351-4 (2024) (Nov. 2017).

25. Berry, V. Impermeability of graphene and its applications. *Carbon* **62,** 1–10. ISSN: 0008-6223. https://www.sciencedirect.com/science/article/pii/S0008622313004880 (2013).

26. Huang, Y., Wu, J. & Hwang, K. C. Thickness of graphene and single-wall carbon nanotubes. en. *Physical Review B* **74,** 245413. ISSN: 1098-0121, 1550-235X. https://link.aps.org/doi/10.1103/PhysRevB.74.245413 (2024) (Dec. 2006).

27. Ugeda, M. M., Brihuega, I., Guinea, F. & Gómez-Rodríguez, J. M. Missing Atom as a Source of Carbon Magnetism. en. *Physical Review Letters* **104,** 096804. ISSN: 0031-9007, 1079-7114. https://link.aps.org/doi/10.1103/PhysRevLett.104.096804 (2024) (Mar. 2010).

28. Banhart, F., Kotakoski, J. & Krasheninnikov, A. V. Structural Defects in Graphene. *ACS Nano* **5.** Publisher: American Chemical Society, 26–41. ISSN: 1936-0851. https://doi.org/10.1021/nn102598m (2024) (Jan. 2011).

29. Xiong, Z., Zhong, L., Wang, H. & Li, X. Structural Defects, Mechanical Behaviors, and Properties of Two-Dimensional Materials. en. *Materials* **14,** 1192. ISSN: 1996-1944. https://www.mdpi.com/1996-1944/14/5/1192 (2024) (Mar. 2021).

30. Bhatt, M. D., Kim, H. & Kim, G. Various defects in graphene: a review. en. *RSC Advances* **12,** 21520–21547. ISSN: 2046-2069. http://xlink.rsc.org/?DOI=D2RA01436J (2024) (2022).

31. Chen, Z., Gandhi, U., Lee, J. & Wagoner, R. Variation and consistency of Young's modulus in steel. en. *Journal of Materials Processing Technology* **227,** 227–243. ISSN: 09240136. https://linkinghub.elsevier.com/retrieve/pii/S0924013615301011 (2024) (Jan. 2016).

32. Kurlov, A. S. & Gusev, A. I. en. in *Tungsten Carbides: Structure, Properties and Application in Hardmetals* (eds Kurlov, A. S. & Gusev, A. I.) 1–3 (Springer International Publishing, Cham, 2013). ISBN: 978-3-319-00524-9. https://doi.org/10.1007/978-3-319-00524-9_1 (2024).

33. Li, M. *et al.* Effect of Defects on the Mechanical and Thermal Properties of Graphene. en. *Nanomaterials* **9,** 347. ISSN: 2079-4991. https://www.mdpi.com/2079-4991/9/3/347 (2024) (Mar. 2019).

34. Novoselov, K. S. *et al.* Electric Field Effect in Atomically Thin Carbon Films. en. *Science* **306,** 666–669. ISSN: 0036-8075, 1095-9203. https://www.science.org/doi/10.1126/science.1102896 (2024) (Oct. 2004).

35. Mak, K. F., Lee, C., Hone, J., Shan, J. & Heinz, T. F. Atomically Thin MoS2: A New Direct-Gap Semiconductor. *Physical Review Letters* **105.** Publisher: American Physical Society, 136805. https://link.aps.org/doi/10.1103/PhysRevLett.105.136805 (2024) (Sept. 2010).

36. Hong, J. *et al.* Exploring atomic defects in molybdenum disulphide monolayers. en. *Nature Communications* **6.** Publisher: Nature Publishing Group, 1–8. ISSN: 2041-1723. https://www.nature.com/articles/ncomms7293 (2024) (Feb. 2015).

37. Ossila B.V. *Molybdenum Disulfide, MoS2: Theory, Structure & Applications* https://www.ossila.com/pages/molybdenum-disulfide-mos2#ref1 (2024).

38. Komsa, H.-P. & Krasheninnikov, A. V. Native defects in bulk and monolayer MoS 2 from first principles. en. *Physical Review B* **91,** 125304. ISSN: 1098-0121, 1550-235X. https://link.aps.org/doi/10.1103/PhysRevB.91.125304 (2024) (Mar. 2015).

39. Zhou, W. *et al.* Intrinsic Structural Defects in Monolayer Molybdenum Disulfide. *Nano Letters* **13.** Publisher: American Chemical Society, 2615–2622. ISSN: 1530-6984. https://doi.org/10.1021/nl4007479 (2024) (June 2013).

40. Bertolazzi, S., Brivio, J. & Kis, A. Stretching and breaking of ultrathin MoS2. eng. *ACS nano* **5,** 9703–9709. ISSN: 1936-086X (Dec. 2011).

41. Castellanos-Gomez, A. *et al.* Elastic Properties of Freely Suspended MoS2 Nanosheets. *Advanced Materials* **24,** 772–775. ISSN: 1521-4095. https://onlinelibrary.wiley.com/doi/abs/10.1002/adma.201103965 (2024) (2012).

42. Peng, Q. & De, S. Outstanding mechanical properties of monolayer MoS2 and its application in elastic energy storage. en. *Physical Chemistry Chemical Physics* **15.** Publisher: The Royal Society of Chemistry, 19427–19437. ISSN: 1463-9084. https://pubs.rsc.org/en/content/articlelanding/2013/cp/c3cp52879k (2024) (Oct. 2013).

43. Hashimoto, A., Suenaga, K., Gloter, A., Urita, K. & Iijima, S. Direct evidence for atomic defects in graphene layers. en. *Nature* **430,** 870–873. ISSN: 1476-4687. https://www.nature.com/articles/nature02817 (2024) (Aug. 2004).

44. Dettori, R., Cadelano, E. & Colombo, L. Elastic fields and moduli in defected graphene. en. *Journal of Physics: Condensed Matter* **24,** 104020. ISSN: 0953-8984, 1361-648X. https://iopscience.iop.org/article/10.1088/0953-8984/24/10/104020 (2024) (Mar. 2012).

45. Lorenz, T., Teich, D., Joswig, J.-O. & Seifert, G. Theoretical Study of the Mechanical Behavior of Individual TiS2 and MoS2 Nanotubes. *The Journal of Physical Chemistry C* **116.** Publisher: American Chemical Society, 11714–11721. ISSN: 1932-7447. https://doi.org/10.1021/jp300709w (2024) (May 2012).

46. Güryel, S. *et al.* Effect of structural defects and chemical functionalisation on the intrinsic mechanical properties of graphene. en. *Physical Chemistry Chemical Physics* **15.** Publisher: The Royal Society of Chemistry, 659–665. ISSN: 1463-9084. https://pubs.rsc.org/en/content/articlelanding/2013/cp/c2cp43033a (2024) (Dec. 2012).

47. Kvashnin, A. G., Sorokin, P. B. & Kvashnin, D. G. The Theoretical Study of Mechanical Properties of Graphene Membranes. en. *Fullerenes, Nanotubes and Carbon Nanostructures* **18,** 497–500. ISSN: 1536-383X, 1536-4046. http://www.tandfonline.com/doi/abs/10.1080/1536383X.2010.488160 (2024) (Oct. 2010).

48. Kvashnin, D. & Sorokin, P. Effect of Ultrahigh Stiffness of Defective Graphene from Atomistic Point of View. *The Journal of Physical Chemistry Letters* **6.** Publisher: American Chemical Society, 2384–2387. https://doi.org/10.1021/acs.jpclett.5b00740 (2024) (June 2015).

49. Hao, F., Fang, D. & Xu, Z. Mechanical and thermal transport properties of graphene with defects. *Applied Physics Letters* **99,** 041901. ISSN: 0003-6951. https://doi.org/10.1063/1.3615290 (2024) (July 2011).

50. Wang, M. C., Yan, C., Ma, L., Hu, N. & Chen, M. W. Effect of defects on fracture strength of graphene sheets. *Computational Materials Science* **54,** 236–239. ISSN: 0927-0256. https://www.sciencedirect.com/science/article/pii/S0927025611006033 (2024) (Mar. 2012).

51. Dewapriya, M. A. N. & Rajapakse, R. K. N. D. Molecular Dynamics Simulations and Continuum Modeling of Temperature and Strain Rate Dependent Fracture Strength of Graphene With Vacancy Defects. *Journal of Applied Mechanics* **81.** ISSN: 0021-8936. https://doi.org/10.1115/1.4027681 (2024) (June 2014).

52. Jing, N. *et al.* Effect of defects on Young's modulus of graphene sheets: a molecular dynamics simulation. en. *RSC Advances* **2.** Publisher: Royal Society of Chemistry, 9124–9129. https://pubs.rsc.org/en/content/articlelanding/2012/ra/c2ra21228e (2024) (2012).

53. Tapia, A., Peón-Escalante, R., Villanueva, C. & Avilés, F. Influence of vacancies on the elastic properties of a graphene sheet. *Computational Materials Science* **55,** 255–262. ISSN: 0927-0256. https://www.sciencedirect.com/science/article/pii/S0927025611006744 (2024) (Apr. 2012).

54. Kazemi, S. A. *et al.* Vacancy impacts on electronic and mechanical properties of MX2 (M = Mo, W and X = S, Se) monolayers. en. *RSC Advances* **13.** Publisher: The Royal Society of Chemistry, 6498–6506. ISSN: 2046-2069. https://pubs.rsc.org/en/content/articlelanding/2023/ra/d3ra00205e (2024) (Feb. 2023).

55. Li, M., Wan, Y., Tu, L., Yang, Y. & Lou, J. The Effect of VMoS3 Point Defect on the Elastic Properties of Monolayer MoS2 with REBO Potentials. en. *Nanoscale Research Letters* **11,** 155. ISSN: 1931-7573, 1556-276X. https://link.springer.com/10.1186/s11671-016-1377-x (2024) (Dec. 2016).

56. Li, M., Wan, Y. & Wang, W. *Prediction of mechanical properties for defective monolayer MoS2 with single molybdenum vacancy defects using molecular dynamics simulations* en. in *2017 IEEE 17th International Conference on Nanotechnology (IEEE-NANO)* (IEEE, Pittsburgh, PA, USA, July 2017), 9–12. ISBN: 978-1-5090-3028-6. http://ieeexplore.ieee.org/document/8117324/ (2024).

57. Ito, A. & Okamoto, S. Molecular Dynamics Analysis on Effects of Vacancies upon Mechanical Properties of Graphene and Graphite. *Engineering Letters* **20** (Aug. 2012).

58. Joswig, J.-O., Lorenz, T., Wendumu, T. B., Gemming, S. & Seifert, G. Optics, Mechanics, and Energetics of Two-Dimensional MoS2 Nanostructures from a Theoretical Perspective. *Accounts of Chemical Research* **48.** Publisher: American Chemical Society, 48–55. ISSN: 0001-4842. https://doi.org/10.1021/ar500318p (2024) (Jan. 2015).

D

Source Code Parameter Extraction

The python scripts used to analyze and plot the data presented in this thesis can be found in the following GitHub repository:

`https://github.com/LukasPott/AllOpticalModulusCalculation.git`